








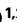


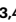



# Hypothalamic deep brain stimulation augments walking after spinal cord injury

Received: 17 May 2024

Accepted: 13 September 2024

Published online: 02 December 2024

 Check for updates

Newton Cho <sup>1,2,9</sup>, Jordan W. Squair <sup>1,2,3,4,9</sup>, Viviana Aureli <sup>1,2,3,4</sup>, Nicholas D. James <sup>1,2</sup>, Léa Bole-Feysot<sup>1,2</sup>, Inssia Dewany <sup>1,2</sup>, Nicolas Hankov<sup>1,2</sup>, Laetitia Baud <sup>1,2</sup>, Anna Leonhartsberger<sup>1,2</sup>, Kristina Sveistyte<sup>1,2</sup>, Michael A. Skinnider <sup>5</sup>, Matthieu Gautier <sup>1,2</sup>, Achilles Laskaratos <sup>1,2</sup>, Katia Galan<sup>1,2</sup>, Maged Goubran <sup>6</sup>, Jimmy Ravier<sup>1,2</sup>, Frederic Merlos<sup>1,2</sup>, Laura Batti<sup>7</sup>, Stéphane Pages<sup>7</sup>, Nadia Berard <sup>1,4</sup>, Nadine Interling <sup>1,4</sup>, Camille Varescon<sup>1,4</sup>, Anne Watrin<sup>8</sup>, Léa Duguet<sup>8</sup>, Stefano Carda<sup>4</sup>, Kay A. Bartholdi<sup>1,2</sup>, Thomas H. Hutson <sup>1,2,7</sup>, Claudia Kathe <sup>1,2</sup>, Michael Hodara<sup>1,2</sup>, Mark A. Anderson <sup>1,2,7</sup>, Bogdan Draganski <sup>4</sup>, Robin Demesmaeker <sup>1,2</sup>, Leonie Asboth<sup>1,2</sup>, Quentin Barraud <sup>1,2</sup>, Jocelyne Bloch <sup>1,2,3,4,10</sup> ✉ & Grégoire Courtine <sup>1,2,3,4,10</sup> ✉

A spinal cord injury (SCI) disrupts the neuronal projections from the brain to the region of the spinal cord that produces walking, leading to various degrees of paralysis. Here, we aimed to identify brain regions that steer the recovery of walking after incomplete SCI and that could be targeted to augment this recovery. To uncover these regions, we constructed a space–time brain-wide atlas of transcriptionally active and spinal cord-projecting neurons underlying the recovery of walking after incomplete SCI. Unexpectedly, interrogation of this atlas nominated the lateral hypothalamus (LH). We demonstrate that glutamatergic neurons located in the LH (LH<sup>Vglut2</sup>) contribute to the recovery of walking after incomplete SCI and that augmenting their activity improves walking. We translated this discovery into a deep brain stimulation therapy of the LH (DBS<sup>LH</sup>) that immediately augmented walking in mice and rats with SCI and durably increased recovery through the reorganization of residual lumbar-terminating projections from brainstem neurons. A pilot clinical study showed that DBS<sup>LH</sup> immediately improved walking in two participants with incomplete SCI and, in conjunction with rehabilitation, mediated functional recovery that persisted when DBS<sup>LH</sup> was turned off. There were no serious adverse events related to DBS<sup>LH</sup>. These results highlight the potential of targeting specific brain regions to maximize the engagement of spinal cord-projecting neurons in the recovery of neurological functions after SCI. Further trials must establish the safety and efficacy profile of DBS<sup>LH</sup>, including potential changes in body weight, psychological status, hormonal profiles and autonomic functions.

Spinal cord injury (SCI) scatters the communication between the brain and the neurons in the lumbar spinal cord that must be activated to produce walking<sup>1–3</sup>. When the SCI is incomplete, the reorganization of residual projections from spinal cord-projecting neuronal populations located in the brain restores a sufficient degree of communication to mediate spontaneous yet partial recovery of walking<sup>4–8</sup>. Although many regions of the brain have been implicated in the orchestration of walking in the absence of injury<sup>3</sup>, the relative implication of these regions after SCI and the potential of additional recovery-organizing regions to contribute to the recovery of walking remain unknown.

Prioritizing regions and neurons across the entire brain that are responsive to biological perturbations remains a fundamental challenge in neuroscience<sup>9</sup>. Central to the resolution of this challenge is the deployment of technologies that permit concomitant anatomical and functional brain-wide cellular-resolution mapping in large organisms<sup>10–15</sup>.

Here, we leveraged these technologies to harmonize whole-brain quantifications of transcriptionally active and spinal cord-projecting neurons during the spontaneous recovery of walking after incomplete SCI. We hypothesized that the interrogation of this combined anatomical and functional atlas would uncover the key regions and neurons of the brain that contribute to the spontaneous recovery of walking after partial SCI and that tapping into these regions and neurons could augment this recovery.

## Results

### Space–time brain-wide atlas

When an SCI spares abundant projections from spinal cord-projecting neurons located in the brain, the initial paralysis is followed by the spontaneous recovery of walking<sup>4–8</sup>. We reasoned that this natural repair would provide the opportunity to expose the key regions and neurons of the brain involved in the spontaneous recovery of walking after incomplete SCI.

Therefore, we selected a model of lateral hemisection SCI, as we and others previously demonstrated that both mice and humans spontaneously regain walking ability after this type of injury<sup>4,5,16,17</sup>. Indeed, we found that mice with a low-thoracic lateral hemisection SCI displayed immediate paralysis but partially recovered walking function over 8 weeks (Fig. 1a–c, Extended Data Fig. 1a–c and Supplementary Video 1).

To identify the key regions of the brain involved in the production of walking during this spontaneous recovery, we optimized immunolabeling-enabled three-dimensional (3D) imaging of solvent-cleared organs (iDISCO+) to achieve whole-brain labeling of cFos—a marker of neuronal activity-induced transcription<sup>18</sup> (Extended Data Fig. 1d). The use of a high-resolution CLARITY-optimized light-sheet microscope (COLM)<sup>10</sup> allowed automated 3D nuclear spot detection of the cFos signal (Extended Data Fig. 1d,e). We surveyed the brains of 12 uninjured and injured mice at time intervals that captured the process of spontaneous recovery from SCI, including at 1 week (acute) and 8 weeks (chronic) after SCI (Fig. 1d and Extended Data Fig. 1e). We registered all 12 brains into the mouse Allen Brain Atlas<sup>19,20</sup> to quantify the number of active cells during walking in each of the 1,111 regions from each brain within a common coordinate space (Fig. 1d and Extended Data Fig. 1d). We validated this space–time brain-wide atlas in uninjured mice, showing that cFos<sup>ON</sup> cells were primarily detected in regions of the brain that are known to contribute to the production of walking, including the cuneiform nucleus, pedunculopontine nucleus, primary motor cortex and medullary reticular formation (Extended Data Fig. 1d)<sup>3</sup>.

Residual projections from spinal cord-projecting neurons located in the brain are well known to contribute to the recovery of walking after incomplete SCI<sup>4–8</sup>. Consequently, we reasoned that prioritizing transcriptionally active regions of the brain containing neurons with residual projections to the lumbar spinal cord would expose the recovery-organizing regions of the brain after incomplete SCI. To map these neuronal projections, we infused a G protein-deficient rabies

virus encoding fluorescent protein markers<sup>21</sup> into the lumbar region of the ipsilesional spinal cord below the injury (Extended Data Fig. 2a). We optimized CLARITY<sup>11</sup> to achieve brain-wide visualization of spinal cord-projecting neurons (Fig. 1d,e and Extended Data Fig. 2a), which we imaged using a mesoscale selective plane-illumination microscope<sup>22</sup> (mesoSPIM; Extended Data Fig. 2a–c).

We next interrogated this space–time brain-wide atlas of recovery from SCI to identify the regions of the brain that contribute to this recovery. We hypothesized that recovery-organizing regions must fulfill four functional and anatomical criteria. First, we reasoned that these regions must demonstrate a decrease in transcriptional activity in the early phase after SCI, coinciding with the loss of walking. Second, the transcriptional activity of these regions must increase during the spontaneous recovery of walking. Third, the density of neuronal projections from these regions to the lumbar spinal cord must decline after injury. Fourth, the spontaneous recovery of walking must coincide with an increase in the density of neuronal projections from these regions to the lumbar spinal cord, which would reflect the sprouting of intact axons from the contralateral side that reintegrate with the neurons in the lumbar spinal cord responsible for the production of walking.

To expose regions exhibiting this archetypal pattern, we conducted normal-based empirical Bayes differential analyses<sup>23</sup> of transcriptional activity and anatomical connectivity following stringent quality control (Extended Data Fig. 3). While many regions fulfilled individual criteria (Fig. 1g and Extended Data Fig. 3l), only a single region emerged that met all the four criteria attributed to recovery-organizing regions: the lateral hypothalamus (LH) (Fig. 1f–h and Extended Data Fig. 2c).

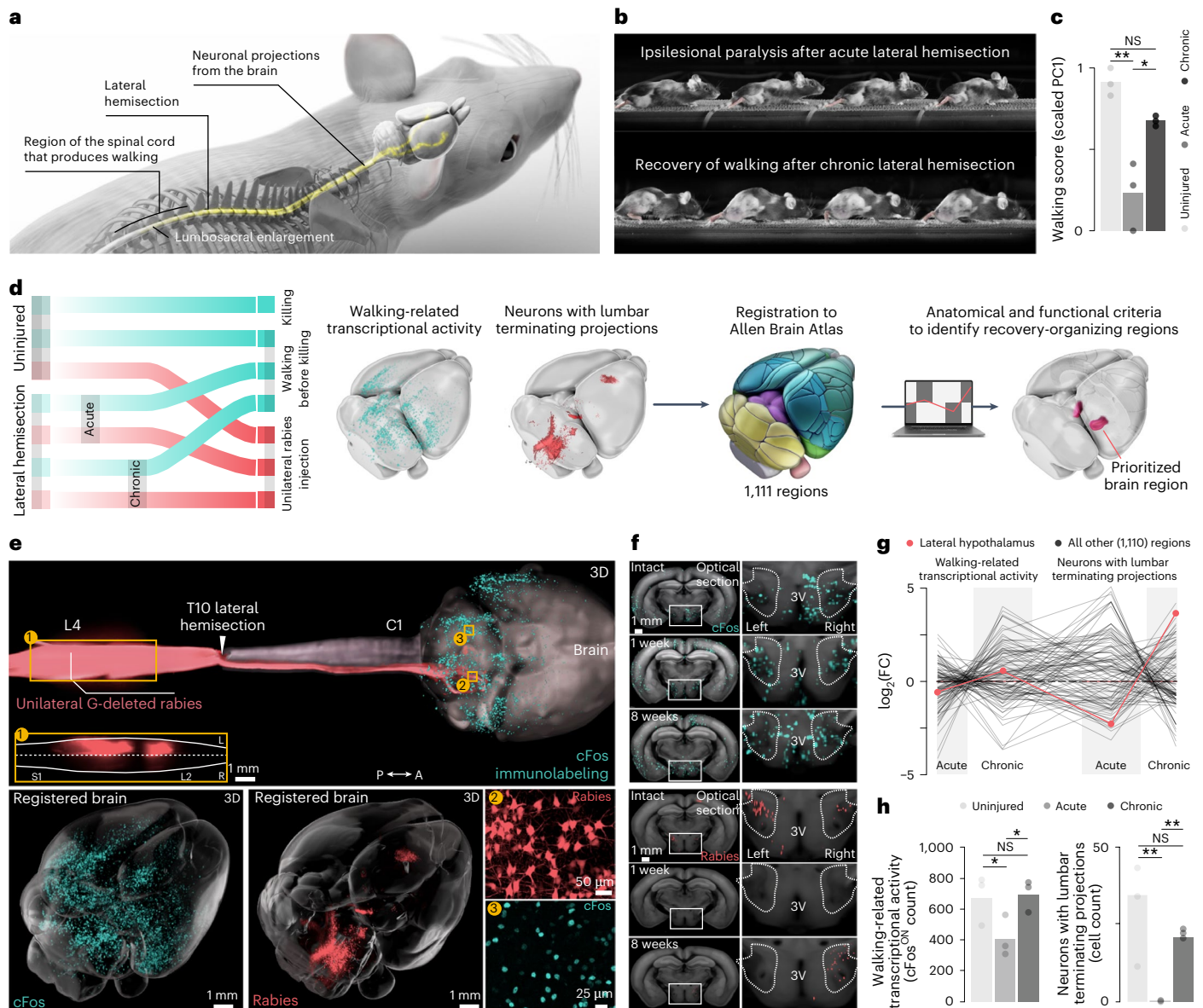
The analysis of our space–time brain-wide atlas suggested that key neurons responsible for the spontaneous recovery of walking after incomplete SCI are unexpectedly located in the LH, a highly specialized region of the brain that is primarily known to regulate arousal, feeding and motivated behavior<sup>24–28</sup>. However, historical work also documented the involvement of the LH in the production of movement<sup>29–31</sup>, which motivated us to test the potential role of the LH in the recovery of walking after incomplete SCI.

### LH<sup>Vglut2</sup> neurons augment walking after SCI

We speculated that neurons located in the LH may be essential to mediate spontaneous recovery of walking after SCI. While neuronal populations located in the LH have been classified with different granularities, all neurons of the LH express either the excitatory neurotransmitter Slc17a6 (also known as Vglut2) or the inhibitory neurotransmitter Slc32a1 (also known as Vgat)<sup>24</sup>. Therefore, we asked whether LH<sup>Vglut2</sup> or LH<sup>Vgat</sup> neurons contribute to the spontaneous recovery of walking in mice after a lateral hemisection SCI.

To test this hypothesis, we selectively activated these two neuronal subpopulations in the LH with optogenetics<sup>32,33</sup>. We injected adeno-associated viruses (AAVs) expressing channelrhodopsin in a Cre-dependent manner<sup>34</sup> into the LH of Vglut2<sup>Cre</sup> and Vgat<sup>Cre</sup> mice with chronic lateral hemisection SCI. Photostimulation of the LH with blue light robustly activated LH<sup>Vglut2</sup> neurons (Extended Data Fig. 4a). This optogenetic activation of LH<sup>Vglut2</sup> neurons immediately alleviated residual gait deficits that persisted despite the spontaneous recovery of walking (Fig. 2a–c, Extended Data Fig. 4b and Supplementary Video 2). Augmenting the activation of LH<sup>Vglut2</sup> neurons with increasing photostimulation frequencies induced a proportional increase in the relative facilitation of walking, even eliciting powerful jumps in the injured mice with high frequencies of photostimulation (Extended Data Fig. 4c). Photostimulation of the LH after injections of AAVs expressing only the reporter protein green fluorescent protein (GFP) or of LH<sup>Vgat</sup> neurons failed to influence walking (Extended Data Figs. 4d and 5a,b).

The immediate facilitation of walking in response to the activation of LH<sup>Vglut2</sup> neurons led us to hypothesize that the inactivation of LH<sup>Vglut2</sup> neurons would conversely impair walking. Indeed, optogenetic inactivation of LH<sup>Vglut2</sup> neurons disrupted the production of



**Fig. 1 | Space-time brain-wide atlas of recovery from SCI nominates the LH.** **a**, Overview of the experimental approach for lateral hemisection SCI in mice. **b**, Chronophotography of walking captured at 1 week (acute) and 8 weeks (chronic) after a lateral hemisection SCI. **c**, Walking was quantified using principal component analysis applied to gait parameters calculated from kinematic recordings. The first principal component (PC1) distinguished gaits between mice without and with SCI. Walking scores were thus quantified as the scores on PC1 ( $n \geq 10$  gait cycles per mouse,  $n = 3$  mice per group). Statistics are provided in Supplementary Data 1. **d**, Overview of the experimental approach to elaborate a space-time brain-wide atlas of recovery after SCI. **e**, 3D visualization of cFos immunolabeling and G-deleted rabies-mediated labeling of lumbar spinal

cord-projecting neurons throughout the CNS in overlaid brains. **f**, Representative optical sections (50- $\mu$ m projection) demonstrating cFos activity and retrogradely labeled neurons in the LH of uninjured mice and mice after acute and chronic injury. 3V, third ventricle. **g**, Log fold changes (FC) of transcriptional activity (cFos) and spinal cord-projecting neurons (rabies) in 1,111 brain regions. Individual lines represent individual regions. This analysis nominated the LH (shown in red) as the sole region exhibiting the expected statistical changes (Extended Data Fig. 3k,l). **h**, Quantification of transcriptional activity (cFos) and spinal cord-projecting neurons (rabies) from the contralesional (right) LH ( $n = 3$  per group). Statistics are provided in Supplementary Data 2. NS, no significance.

walking (Fig. 2d-f, Extended Data Fig. 5c,d and Supplementary Video 2), whereas the same photostimulation of the LH after injections of AAVs expressing only reporter proteins had no effect (Extended Data Fig. 5e).

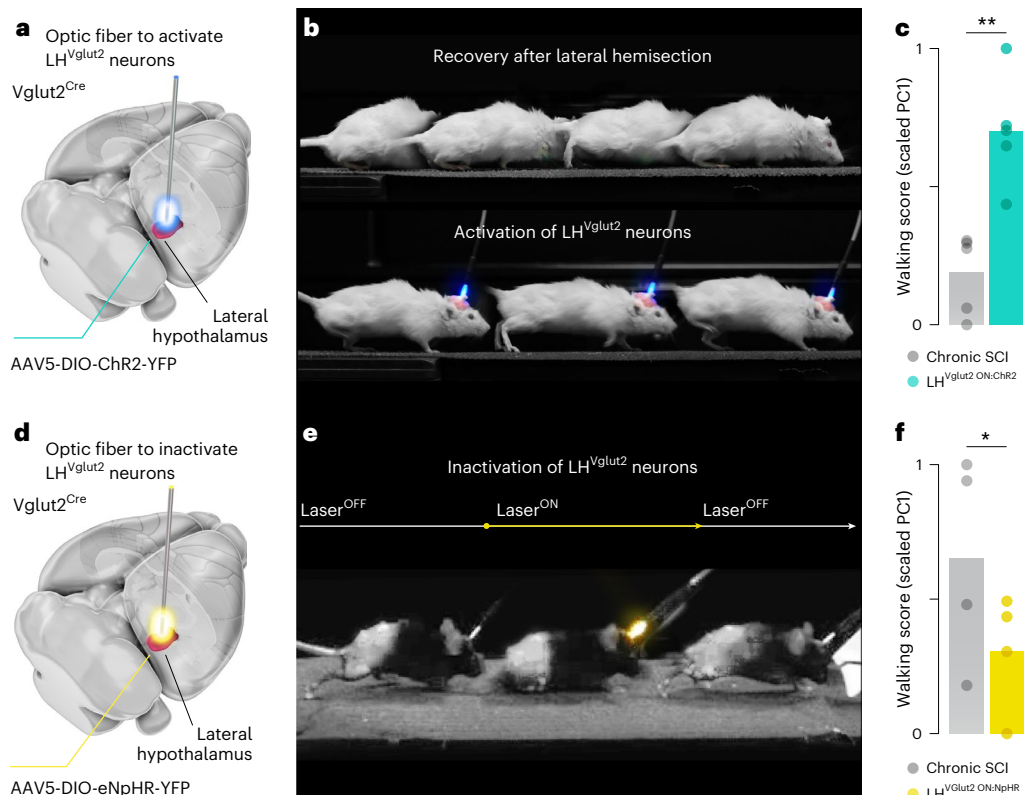
These results demonstrate that LH<sup>Vglut2</sup> neurons not only contribute to the recovery of walking after SCI but are also sufficient to augment the quality and vigor of walking after incomplete SCI.

### LH augments walking through relays

Our results thus far demonstrate the necessity and sufficiency of LH<sup>Vglut2</sup> neurons for regaining and augmenting walking after lateral hemisection SCI. We next sought to determine whether activation of LH<sup>Vglut2</sup>

neurons also improves walking in a more clinically relevant model of SCI, as lateral spinal cord hemisections rarely occur in humans<sup>16</sup>. Indeed, spinal cord damage observed in humans leads to pathophysiology that has been proposed to be reliably modeled with contusion SCI<sup>35,36</sup>. Consequently, we tested whether the activation of LH<sup>Vglut2</sup> neurons improves walking after contusion SCI.

To model an incomplete contusion SCI, we delivered a robotically controlled impact onto the midthoracic spinal cord (Extended Data Fig. 6a). This contusion led to severe bilateral impairments of the lower limbs (Extended Data Fig. 6b). We reasoned that direct projections from LH neurons to the lumbar spinal cord must exist to mediate



**Fig. 2 | LH<sup>Vglut2</sup> neurons contribute to the recovery of walking after SCI.**

**a**, Overview of experiments for optogenetic activation of LH<sup>Vglut2</sup> neurons. **b**, Chronophotography of mice with and without photostimulation. **c**, Walking was quantified using principal component analysis as described in Fig. 1c ( $n \geq 10$  gait cycles per mouse,  $n = 5$  mice per group). Statistics are provided in

Supplementary Data 1. **d**, Overview of experiments for optogenetic inhibition of LH<sup>Vglut2</sup> neurons. **e**, As in **b**, for optogenetic inhibition. **f**, As in **c**, for optogenetic inhibition ( $n \geq 10$  gait cycles per mouse,  $n = 4$  mice per group). Statistics are provided in Supplementary Data 1.

improvements in walking after contusion SCI. Thus, we aimed to confirm the survival of LH-derived neuronal projections below the injury. For this purpose, we injected G protein-deficient rabies virus encoding a fluorescent protein in the lumbar spinal cord<sup>21</sup>. Contrary to our hypothesis but consistent with the absence of correlations between the density of residual projections from LH neurons and the recovery of walking after SCI<sup>37</sup>, this anatomical survey revealed that the contusion SCI interrupted all the projections from LH neurons below the injury (Fig. 3a and Extended Data Fig. 6c). Therefore, we anticipated that improvement in walking following the activation of LH<sup>Vglut2</sup> neurons in mice with contusion SCI would need to rely on indirect neuronal relays, whereby LH<sup>Vglut2</sup> neurons project to downstream regions of the brain containing spinal cord-projecting neurons with residual projections below the injury.

To identify regions containing these putative relay neurons, we exposed the projectome of LH<sup>Vglut2</sup> neurons using stereotaxic injections of AAVs expressing reporter proteins in the LH of Vglut2<sup>Cre</sup> mice. This strategy labeled the axons emanating from LH<sup>Vglut2</sup> neurons. We found that LH<sup>Vglut2</sup> neurons project to multiple regions of the brain that are known to be involved in the production of walking (Extended Data Fig. 6d). In particular, we found that LH<sup>Vglut2</sup> neurons established synaptic contacts with each neuron of the ventral gigantocellular nucleus (vGi) that retained residual projections below the contusion SCI (Fig. 3b and Extended Data Figs. 6c and 7a–c). We previously demonstrated that the motor cortex relays executive commands through vGi<sup>Vglut2</sup> neurons to produce walking after contusion SCI<sup>36</sup>. Consistent with this mechanism, we found that vGi<sup>Vglut2</sup> neurons receive a comparable amount of direct synaptic projections from the motor cortex and LH (Extended Data Fig. 7d).

This anatomical survey, combined with our prior work, led us to hypothesize that vGi<sup>Vglut2</sup> neurons could relay information from LH<sup>Vglut2</sup>

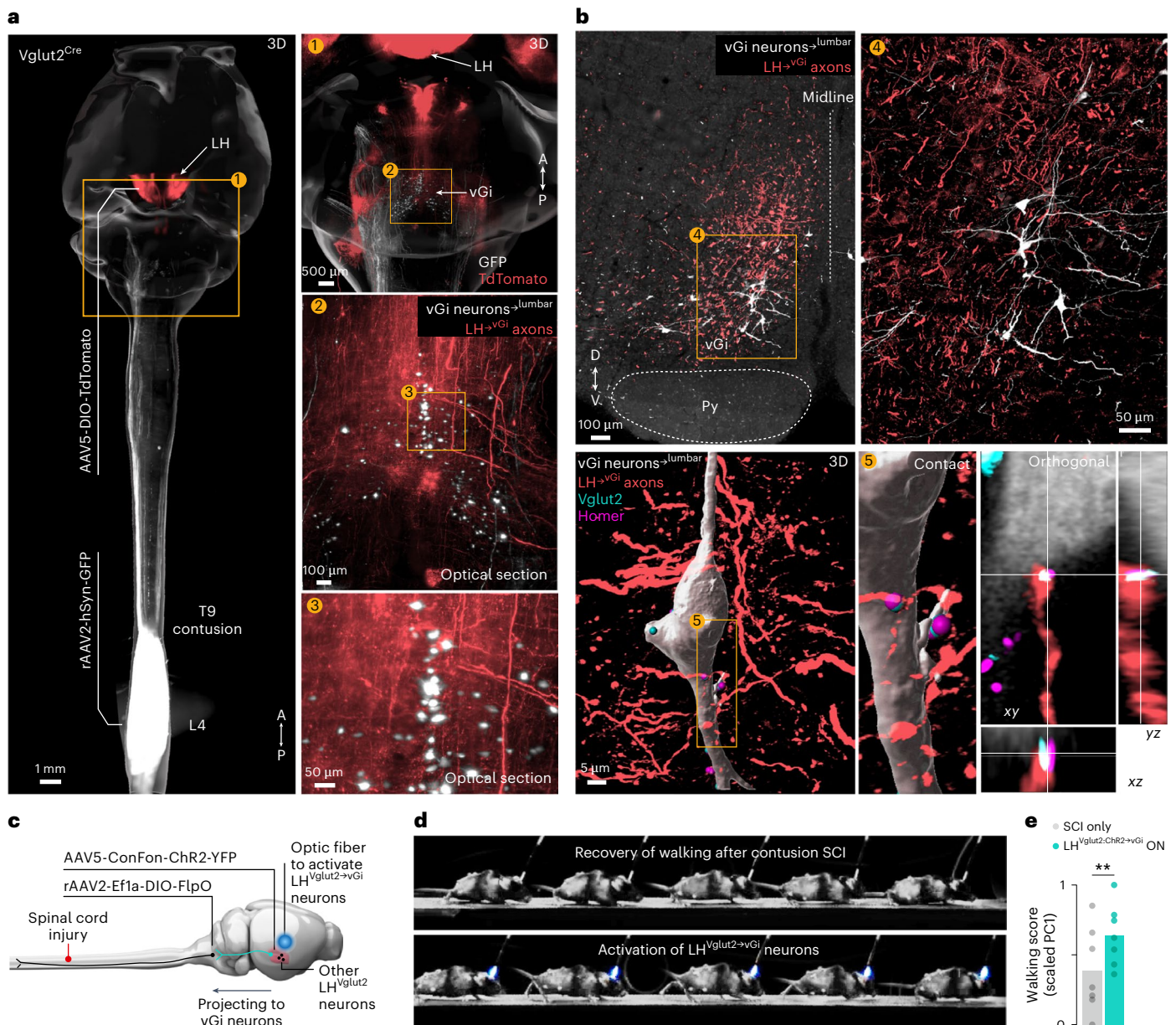
neurons to improve walking after contusion SCI. To test this possibility, we devised an intersectional genetic strategy that allowed us to restrict the expression of channelrhodopsin to LH<sup>Vglut2</sup> neurons projecting to vGi neurons<sup>38</sup>. We injected a retrograde-enabled recombinant AAV (rAAV2)<sup>39</sup> expressing Flp recombinase into the vGi of Vglut2<sup>Cre</sup> mice. We then injected AAVs expressing channelrhodopsin in a Cre- and Flp-dependent manner in the LH to manipulate the activity of LH<sup>Vglut2-vGi</sup> neurons (Fig. 3c and Extended Data Fig. 7e). The selective optogenetic activation of LH<sup>Vglut2-vGi</sup> neurons was sufficient to mediate an immediate improvement in walking in mice with contusion SCI (Fig. 3d,e, Extended Data Fig. 7f and Supplementary Video 3).

We next logically asked whether vGi<sup>Vglut2</sup> neurons are necessary to augment walking in response to the activation of LH<sup>Vglut2</sup> neurons. To manipulate the activity of vGi<sup>Vglut2</sup> and LH<sup>Vglut2</sup> neurons concomitantly, we expressed the inhibitory Gi-DREADD (Gi-coupled designer receptor exclusively activated by designer drug<sup>40</sup>) in vGi<sup>Vglut2</sup> neurons and channelrhodopsin in LH<sup>Vglut2</sup> neurons (Extended Data Fig. 8a). While optogenetic activation of LH<sup>Vglut2</sup> neurons alone improved walking, inactivation of vGi<sup>Vglut2</sup> neurons suppressed this facilitation (Extended Data Fig. 8b). These results supported the hypothesis that vGi<sup>Vglut2</sup> neurons relay information from LH<sup>Vglut2</sup> neurons to improve walking after SCI.

In summary, we found that the LH augments walking through glutamatergic neurons located in the vGi that relay the executive commands from glutamatergic neurons of the LH past the injury to the regions of the lumbar spinal cord responsible for the production of walking, which can be leveraged to augment walking after contusion SCI.

### DBS<sup>LH</sup> immediately and durably improves walking

These results raised the intriguing possibility that tapping into the LH with clinically relevant therapeutic strategies may lead to immediate



**Fig. 3 | Neurons in the vGi relay signals from LH<sup>Vglut2</sup> neurons. a**, Whole-CNS visualization with optical section insets of LH<sup>Vglut2</sup> neurons (red) and spinal cord-projecting neurons in the vGi (white) in a mouse after contusion SCI. **b**, 3D views of synapse-like contacts with pre- and postsynaptic markers of LH<sup>Vglut2</sup> neurons onto vGi neurons with residual projections to the lumbar cord. Py, pyramidal

tract. **c**, Overview of the experimental approach to activate LH<sup>Vglut2</sup> neurons projecting to vGi neurons after contusion SCI. **d**, Chronophotography of mice with and without photostimulation. **e**, Walking was quantified using principal component analysis as described in Fig. 1c ( $n \geq 10$  gait cycles per mouse,  $n = 7$  mice per group). Statistics are provided in Supplementary Data 1.

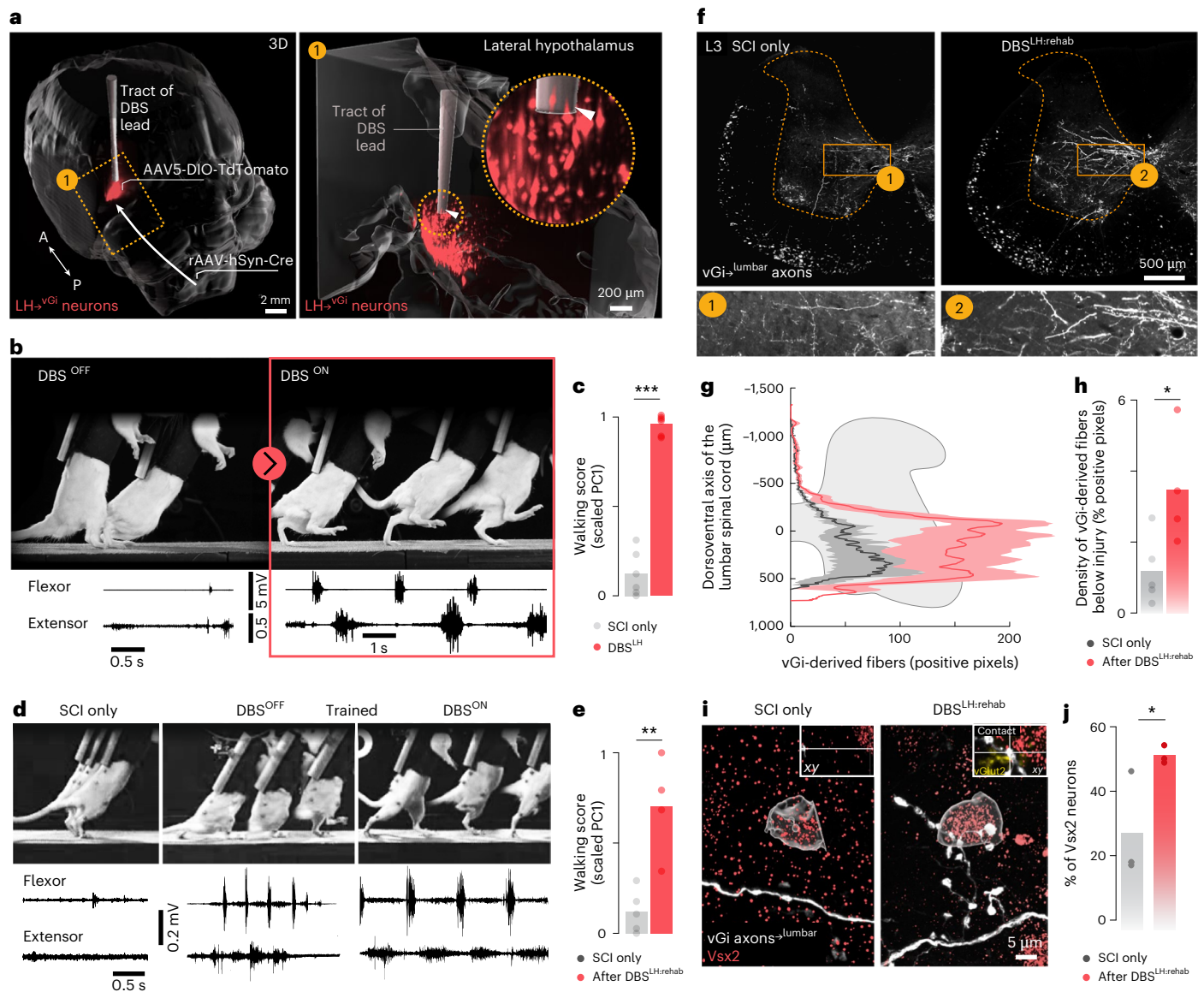
improvement in walking and that delivering this strategy during rehabilitation may trigger a reorganization of residual projections from spinal cord-projecting neurons that can promote durable recovery of walking after SCI. However, implementing optogenetically inspired treatments in humans requires a transition from photostimulation to electrical stimulation modalities<sup>41–43</sup>. Therefore, we assessed whether deep brain stimulation (DBS) therapy of the LH (DBS<sup>LH</sup>) is sufficiently selective to activate LH<sup>Vglut2</sup> neurons to augment walking after SCI.

We first tested whether DBS<sup>LH</sup> is effective in mice with contusion SCI. In all tested mice, DBS<sup>LH</sup> immediately improved walking (Extended Data Fig. 8c,d). We anticipated that these improvements would be contingent on the recruitment of LH<sup>Vglut2</sup> neurons with DBS<sup>LH</sup>. To test this possibility, we injected AAVs expressing the diphtheria toxin receptor<sup>44</sup> in Vglut2<sup>Cre</sup> mice together with the surgical placement of DBS

leads. As expected, the partial loss of LH<sup>Vglut2</sup> neurons following the administration of diphtheria toxin blunted the responses to DBS<sup>LH</sup> (Extended Data Fig. 8d).

We next tested this therapy in rats, as this preclinical model permits the evaluation and rehabilitation of walking in an upright posture, which eliminates the contribution of the upper limbs to the production of lower-limb movements<sup>4,36,45</sup>. Therefore, this experimental paradigm allowed a more rigorous assessment of whether DBS<sup>LH</sup> immediately and durably improves the activation of the lumbar spinal cord to produce walking.

We developed a stereotaxic surgical procedure to target DBS leads to the LH of rats, which we confirmed anatomically after death (Fig. 4a,b, Extended Data Fig. 9a and Supplementary Video 4). Quantification of transcriptionally active cells in response to DBS<sup>LH</sup> revealed



**Fig. 4 | DBS<sup>LH</sup> mediates immediate and long-term improvements in walking in rats with contusion SCI.** **a**, Whole-brain visualization and optical section insets of DBS<sup>LH</sup> position and intersectional tracing strategy to visualize neurons of the LH with projections to the vGi. **b**, Chronophotography of rats with and without DBS<sup>LH</sup>. **c**, Walking was quantified using principal component analysis as described in Fig. 1c ( $n \geq 10$  gait cycles per rat,  $n = 6$  rats per group). Statistics are provided in Supplementary Data 1. **d**, Chronophotography of rats with and without structured rehabilitation augmented by DBS<sup>LH</sup>. **e**, As in **c**, for rats with and without structured rehabilitation augmented by DBS<sup>LH</sup> ( $n = 5$  rats in the SCI group,  $n = 4$  rats in the SCI + rehabilitation group). Statistics are provided in Supplementary Data 1. **f**, Representative photomicrographs of vGi-derived projections (AAV5-

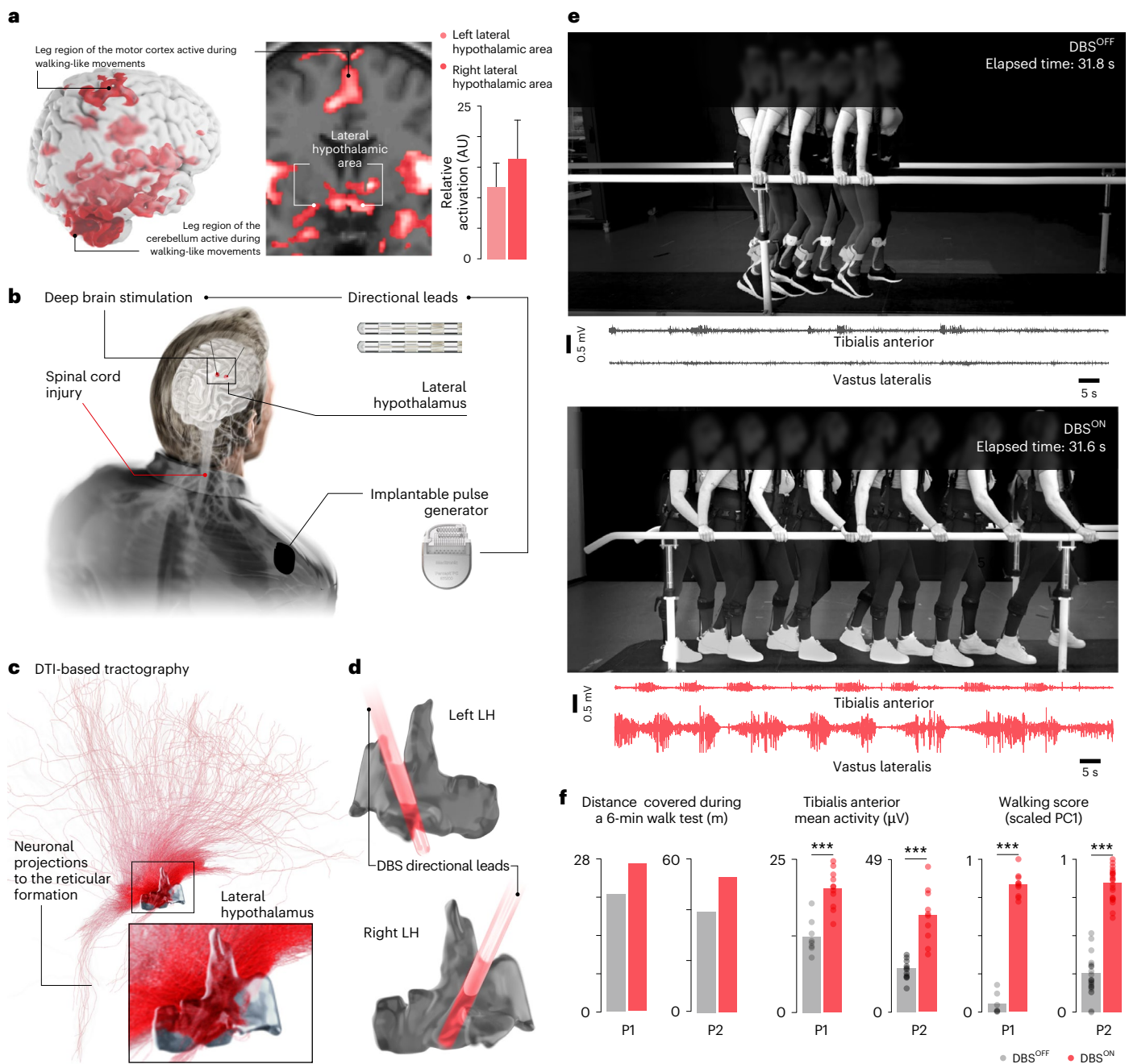
hSyn-eGFP) in the lumbar spinal cord of rats with and without structured rehabilitation augmented by DBS<sup>LH</sup>. **g**, Line graph reporting spatially resolved axon density in the lumbar gray matter ( $n = 5$  rats in the SCI group,  $n = 4$  rats in the SCI + rehabilitation group). **h**, Quantification of vGi-derived projections (shown in **g**) in the lumbar spinal cord of rats with and without rehabilitation augmented by DBS<sup>LH</sup> ( $n = 5$  rats in the SCI group,  $n = 4$  rats in the SCI + rehabilitation group; unpaired *t* test,  $P = 0.0328$ ). **i**, Photomicrograph demonstrating increased density of vGi axonal projections onto immunohistochemically labeled Vsx2-expressing neurons in the intermediate laminae of the lumbar spinal cord. **j**, Quantification of Vsx2 neurons receiving vGi-derived projections in the lumbar spinal cord of rats ( $n = 3$ ; independent samples Wilcoxon rank-sum test;  $w = 9$ ;  $P = 0.05$ ).

that DBS<sup>LH</sup> robustly activated cells located in the LH (Extended Data Fig. 9a). Finally, we tested the impact of DBS<sup>LH</sup> on the modulation of walking in the absence of SCI. We found that DBS<sup>LH</sup> instantly triggered walking and that increasing amplitudes of DBS<sup>LH</sup> elicited a proportional increase in walking speed (Extended Data Fig. 9b).

After validating the procedures to deliver DBS<sup>LH</sup> in rats, we asked whether DBS<sup>LH</sup> was able to improve walking in rats with contusion SCI. This injury damaged 83.2% of the spinal cord, which led to paralysis of the lower limbs (Fig. 4b and Extended Data Fig. 9c). From an upright posture, the rats were not able to initiate or sustain walking. We found that DBS<sup>LH</sup> phenocopied the immediate augmentation of walking

observed with optogenetic activation of LH<sup>Vglut2</sup> neurons (Fig. 4b,c and Extended Data Fig. 9c). Blinded assessments of behavioral responses showed that DBS<sup>LH</sup> did not provoke discomfort, pain or deviation from natural behaviors (Extended Data Fig. 9a).

Having validated the immediate augmentation of walking with DBS<sup>LH</sup>, we next tested whether integrating this strategy during our structured robot-assisted rehabilitation program<sup>4</sup> could mediate durable improvement in walking following contusion SCI. Rats underwent robot-assisted rehabilitation combined with DBS<sup>LH</sup> delivered daily for 8 weeks, starting 1 week after the SCI. In contrast to the permanent deficits in rats that did not undergo rehabilitation,

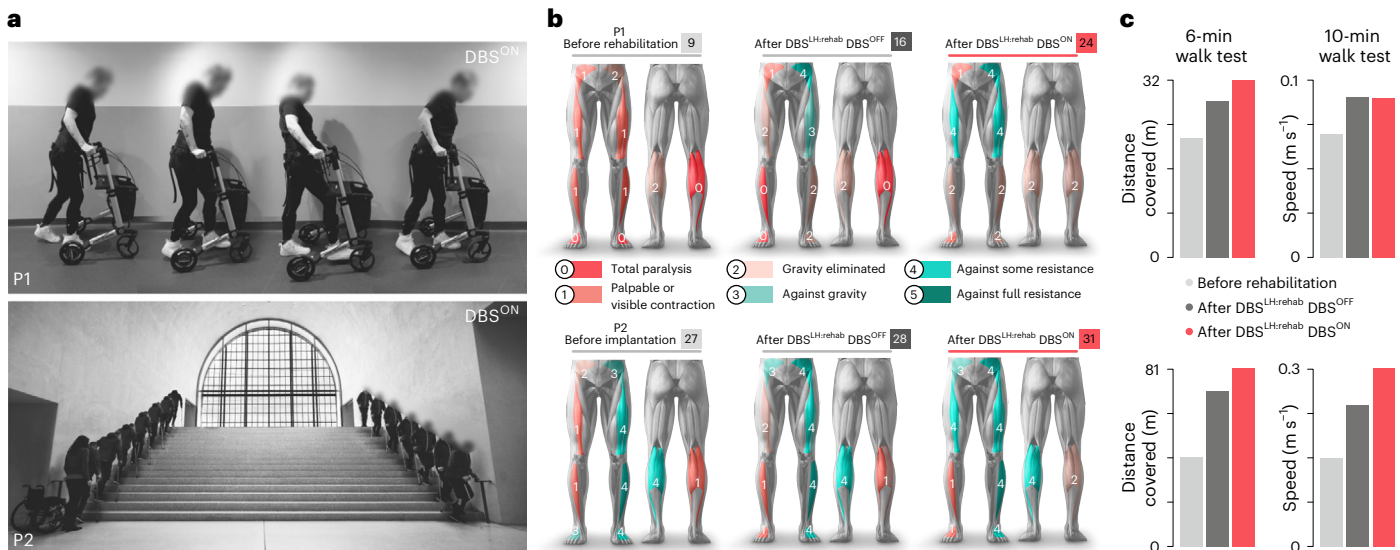


**Fig. 5 | DBS<sup>LH</sup> mediates immediate improvements in walking in humans with SCI.** **a**, fMRI demonstrating activity in various cortical and subcortical regions, including the LH (coronal plane, inset), during a motor task in 21 healthy participants. Bar graphs demonstrate the coefficients of activation in the left and right LH during walking-like movements (left,  $Z = 3.47$ ,  $P < 0.001$ ; right,  $Z = 3.09$ ,  $P = 0.001$ ; bars represent the estimates of the second-level mixed-effect linear model, with the error bars indicating the s.e.m. of the model). **b**, SenSight directional leads (Medtronic) were placed bilaterally in the LH of two human participants with incomplete SCI. The leads were connected to a Medtronic Percept implantable pulse generator. **c**, Whole-brain DTI-enabled reconstruction of fiber projections emanating from the LH of the first participant that guided DBS lead position targeting. **d**, Final electrode positions in the first participant

reconstructed from postoperative computed tomography (CT) scans, together with simulated electrical fields elicited by DBS<sup>LH</sup>. **e**, Chronophotography of walking recorded in the first participant with and without DBS<sup>LH</sup>, together with the associated recording of electromyographic (EMG) activity from extensor and flexor muscles. **f**, Left, a 6-min walk test was performed without DBS<sup>LH</sup> and with DBS<sup>LH</sup> turned on (one trial per participant and condition, no statistics). Middle, quantification of muscle activity in both participants ( $P < 0.001$  for both P1 and P2;  $n \geq 7$  gait cycles, dots represent individual trials). Right, walking was quantified in both participants using principal component analysis as described in Fig. 1c ( $P < 0.001$  for both P1 and P2,  $n \geq 7$  gait cycles). Statistics are provided in Supplementary Data 3.

the rats that followed rehabilitation demonstrated pronounced improvements in walking even when DBS<sup>LH</sup> was turned off (Fig. 4d,e and Extended Data Fig. 9e). Moreover, DBS<sup>LH</sup> continued to augment walking beyond the improvements observed from the beginning to the end of the rehabilitation program (Extended Data Fig. 9f). These

improvements coincided with a growth of vGi-derived neuronal projections in the intermediate lamina of the lumbar spinal cord (Fig. 4f–h), including a twofold increase in the density of projections onto Vsx2-expressing neurons that are necessary to regain walking after SCI (Fig. 4i,j)<sup>46–48</sup>.



**Fig. 6 | DBS<sup>LH</sup> mediates long-term improvements in walking in humans with SCI.** **a**, Chronophotography of the two participants achieving their desired goal after rehabilitation augmented by DBS<sup>LH</sup>. The first participant aimed to walk without orthoses or weight support, whereas the second participant aimed to walk up and down a staircase independently. **b**, Changes in the lower-limb motor scores of each participant before and after rehabilitation, as well as

with DBS<sup>LH</sup> turned on at the end of rehabilitation. A blind assessor conducted the assessments according to the ISNCSCI. Extended details are provided in Supplementary Table 1. **c**, Bar graphs reporting changes for each participant in the 6-min and 10-m walk tests before and after rehabilitation, as well as with DBS<sup>LH</sup> turned on at the end of rehabilitation.

### DBS<sup>LH</sup> augments walking in humans

Our results thus far identified DBS<sup>LH</sup> as an effective therapeutic strategy to promote immediate and durable improvements in walking in rodent models of SCI, raising the possibility that this strategy may also be beneficial in humans with incomplete SCI.

Before considering the surgical implantation of DBS leads in people with SCI, we sought to ascertain that the LH is activated during walking in humans. To expose this activation, we acquired functional magnetic resonance imaging (fMRI) data during walking-like movements in 21 healthy people (Fig. 5a). These acquisitions revealed a bilateral activation of the LH during walking-like movements (Extended Data Fig. 10a). We determined that these results in humans without SCI and in rodent models of SCI combined with the previously established safety profile of DBS<sup>LH</sup> for other indications<sup>49</sup> provided the necessary conditions to support a clinical study to test the preliminary safety and efficacy of DBS<sup>LH</sup> to improve the recovery of walking in people with chronic SCI (HoT-DBS, clinicaltrials.gov NCT04965727).

We enrolled two participants with chronic incomplete SCI who could ambulate to varying extents with the aid of assistive devices but exhibited persistent gait deficits despite their prior participation in standard rehabilitation programs (Extended Data Fig. 10b and Supplementary Table 1). Each enrolled participant expressed unique goals that they desired to achieve during the study. The first participant aimed to walk without the need for body weight support or extensive orthoses. The second participant, who presented with a less severe injury, expressed the objective to walk longer distances and to be able to climb and descend stairs independently at home.

To determine the placement of DBS leads in the uncharted walking-related territories of the LH, we acquired anatomical (MRI) and diffusion tensor imaging (DTI) data from both participants (Fig. 5b, Extended Data Fig. 10c and Supplementary Video 5). MRI circumscribed the anatomical contours of the LH within an irregular 3D geometry (Extended Data Fig. 10a). This large volume and complex geometry prevented DBS leads from accessing the entire LH. Therefore, we determined the optimal location of the DBS leads based on objective anatomical criteria. Concretely, we leveraged DTI-based tractography

to detect the region of the LH that extended neuronal projections to the brainstem reticular formation, where the neurons that relay LH-originating signals downstream to facilitate walking in response to DBS<sup>LH</sup> are located. In both participants, these preoperative criteria nominated the intermediate aspect of the LH as the optimal location for the DBS leads (Fig. 5c and Extended Data Fig. 10c).

To monitor behavioral responses intraoperatively, we inserted the DBS leads during an awake neurosurgical intervention that was guided by 3D imaging, electrophysiological monitoring and clinical responses. Continuous monitoring of spiking activity during the descent of microelectrodes within the LH exposed the basal activity of neurons throughout the rostrocaudal extent of the LH (Extended Data Fig. 10d). Intraoperative delivery of DBS<sup>LH</sup> elicited immediate sensations in the paralyzed lower limbs, with the first participant reporting, “I feel the urge to move my legs.” The final position of the electrodes was confirmed with intraoperative 3D imaging. No perioperative adverse events or complications occurred.

We next aimed to optimize the configuration of electrode contacts within the complex geometry of the LH. For this purpose, we combined postoperative anatomical reconstructions of the LH and computer simulations of tissue volume activation to predict the configuration of electrodes that maximized the activation of the LH while minimizing the spread of currents toward the surrounding brain structures (Fig. 5d and Extended Data Fig. 10e). To fine-tune the configuration, we conducted postoperative mapping sessions while the participant was instructed to attempt to walk. Configurations were prioritized based on the intensity of the responses in lower-limb muscles and the subjective experience of the participants during their attempt to walk.

Following these mapping sessions, we conducted formal functional evaluations that involved precise kinematic and muscle activity quantifications that we complemented with well-established clinical assessments. In both participants, DBS<sup>LH</sup> immediately augmented the activity of lower-limb muscles (Fig. 5e,f and Extended Data Fig. 10k,l). This increase in muscle activation translated into improved kinematics and endurance (Fig. 5f). The participants also reported a reduced perceived effort to walk.



**Table 1 | Adverse events and hormonal monitoring**

Event	P1	P2
Any adverse event	10	6
Any serious adverse event	0	0
Relationship to medical device under investigation		
Not related	40%	83%
Possibly related	40%	17%
Probably related	20%	0%
Related	0%	0%
Relationship to study procedures		
Not related	20%	67%
Possibly related	0%	33%
Probably related	50%	0%
Related	30%	0%
Severity		
Mild	40%	67%
Moderate	60%	33%
Severe	0%	0%
Hormonal results		
Weight (kg)		
Before implantation	51	90
Before rehabilitation	53	93
1 month after rehabilitation	51	94
3 months after rehabilitation	49	95
6 months after rehabilitation	50	98
Adrenocorticotrophic hormone (ng l <sup>-1</sup> ), range 9–52 ng l <sup>-1</sup>		
Before implantation	-	11
Before rehabilitation	47	10
1 month after rehabilitation	14	9
3 months after rehabilitation	41	10
6 months after rehabilitation	19	12
Thyroid-stimulating hormone (mUI l <sup>-1</sup> ), range 0.5–5 mUI l <sup>-1</sup>		
Before implantation	0.85	2.87
Before rehabilitation	0.82	2.30
1 month after rehabilitation	1.82	2.75
3 months after rehabilitation	1.84	2.43
6 months after rehabilitation	1.24	2.51
Free T4 (pmol l <sup>-1</sup> ), range 11–30 pmol l <sup>-1</sup>		
Before implantation	14.8	15.0
Before rehabilitation	15.8	14.8
1 month after rehabilitation	12.3	14.9
3 months after rehabilitation	15.0	16.5
6 months after rehabilitation	13.1	16.2
Morning serum cortisol (nmol l <sup>-1</sup> ), range 137–689 nmol l <sup>-1</sup>		
Before implantation	348	565
Before rehabilitation	422	410
1 month after rehabilitation	457	310
3 months after rehabilitation	547	435
6 months after rehabilitation	527	487
Prolactin (μg l <sup>-1</sup> ), range 5–25 μg l <sup>-1</sup>		

**Table 1 (continued) | Adverse events and hormonal monitoring**

Event	P1	P2
Before implantation	<sup>a</sup>	11.0
Before rehabilitation	<sup>a</sup>	9.4
1 month after rehabilitation	<sup>a</sup>	9.3
3 months after rehabilitation	4.9	9.9
6 months after rehabilitation	10.4	11.2
Testosterone (nmol l <sup>-1</sup> ), range 8–32 nmol l <sup>-1</sup>		
Before implantation	NA	12.9
Before rehabilitation	NA	-
1 month after rehabilitation	NA	12.0
3 months after rehabilitation	NA	11.7
6 months after rehabilitation	NA	11.0

NA, not assessed. <sup>a</sup>Prolactin monitoring was added during the course of the study.

The participants then underwent a 3-month structured rehabilitation program involving 3 days of gait training per week, for a total of 3 h per session. This rehabilitation program led to pronounced improvement in walking, which was captured by clinical assessments while DBS<sup>LH</sup> was turned off, including superior performance during the 10-m and 6-min walk tests and increases in lower-extremity motor scores as measured by a blind assessor according to the International Standards for Neurological Classification of SCI (ISNCSCI)<sup>50</sup> (Fig. 6a–c, Extended Data Fig. 10m and Supplementary Table 1). At this time point, turning DBS<sup>LH</sup> on still triggered immediate improvements in walking, which were captured in the 10-m and 6-min walk tests, as well as further increases in lower-extremity motor scores beyond the measurements taken at the beginning and the end of the study while DBS<sup>LH</sup> was turned off (Fig. 6b,c). Both participants achieved their respective prerehabilitation goals of walking without orthoses and being able to climb stairs independently.

All procedures throughout the trial were tolerated by both participants. The safety of DBS<sup>LH</sup> was assessed through adverse events reporting and vital signs, weight and hormonal monitoring, including adrenocorticotrophic hormone, thyroid-stimulating hormone, free thyroxine, morning serum cortisol, prolactin and testosterone. No serious adverse events were observed (Table 1 and Supplementary Table 2).

## Discussion

We identified the previously unknown function of glutamatergic neurons located in the LH in steering the recovery of walking after incomplete SCI and showed that these neurons can be targeted with DBS to augment neurological recovery in humans with chronic incomplete SCI.

Central to this discovery were reproducible anatomical, imaging and computational methods that enabled us to elaborate a space–time brain-wide atlas of recovery from SCI. These methods supported the comprehensive survey of every region of the mouse brain during the recovery of walking after incomplete SCI. We combined this survey with rational neurobiological hypotheses based on the known anatomical and functional patterns of recovery following incomplete SCI<sup>2</sup>. Unexpectedly, this analytical framework nominated a single region of the brain that fulfilled all our a priori neurobiological hypotheses. This finding demonstrates the advantages of whole-brain clearing and biologically informed quantification strategies to unravel the previously underappreciated role of specific regions of the brain in the recovery of walking after incomplete SCI. More broadly, this analytical framework can be leveraged to identify the regions of the central nervous system (CNS) that contribute to any biological perturbation or disease.

The LH has been implicated in the regulation of diverse neurological functions, including motivational behaviors, feeding and

reward<sup>24–28</sup>. Indeed, this understanding motivated previous clinical trials that assessed the potential therapeutic impact of DBS<sup>LH</sup> on obesity<sup>49</sup>. In the context of motor control, historical experiments conducted in cat and nonhuman primate models also suggested that the LH may amplify the production of movement<sup>51</sup>. Our results support this conclusion and extend the participation of the LH to recovery from SCI, whereby glutamatergic neurons in the LH contribute to the recovery of walking, and their activation is sufficient to augment the recovery of walking after incomplete SCI. Glutamatergic neurons from the LH do not directly activate the spinal cord but instead engage glutamatergic neurons in the vGi. The sparse distribution of vGi projections within the white matter ensures that a subset of these axons survives incomplete SCIs. These spared projections then establish contacts with Vsx2-expressing neurons in the lumbar spinal cord that are essential to regain walking after SCI<sup>46–48</sup>. Rehabilitation enabled by DBS<sup>LH</sup> further augmented the density of these projections. As epidural electrical stimulation of the spinal cord also modulates Vsx2-expressing neurons to improve the recovery of walking after SCI<sup>46</sup>, we anticipate that combining these two therapies may further augment this recovery in people with incomplete SCI.

These results, combined with observations from previous work<sup>2,6–8</sup>, suggest that an SCI not only affects the activity of the spinal cord below the injury but also disrupts neuronal populations distributed in various regions of the brain, including the brainstem. In turn, neuromodulation therapies are effective strategies to target the regions of the brain and spinal cord involved in the production of walking to ameliorate neurological recovery<sup>46,52–55</sup>.

DBS<sup>LH</sup> was tested in only two participants in a pilot clinical study. Consequently, the effects observed must be interpreted in the context of a pilot clinical study. While no serious adverse events were observed in these two participants, in line with the previously established safety profile of DBS<sup>LH</sup> for other indications<sup>49</sup>, additional trials must be conducted in a larger number of participants to establish the safety and efficacy profile of DBS<sup>LH</sup>, including the evaluation of potential changes in body weight, psychological status, hormonal profiles and autonomic functions. As DBS<sup>LH</sup> targets spared descending projections, we anticipate that not all individuals with SCI will respond to this therapy. Consequently, pivotal trials must establish the optimal neurological profiles of participants who may benefit from rehabilitation augmented by DBS<sup>LH</sup> and should determine the relevant clinical framework to deliver this therapy.

## Online content

Any methods, additional references, Nature Portfolio reporting summaries, source data, extended data, supplementary information, acknowledgements, peer review information; details of author contributions and competing interests; and statements of data and code availability are available at <https://doi.org/10.1038/s41591-024-03306-x>.

## References

- Courtine, G. & Sofroniew, M. V. Spinal cord repair: advances in biology and technology. *Nat. Med.* **25**, 898–908 (2019).
- Anderson, M. A. et al. Natural and targeted circuit reorganization after spinal cord injury. *Nat. Neurosci.* **25**, 1584–1596 (2022).
- Arber, S. & Costa, R. M. Connecting neuronal circuits for movement. *Science* **360**, 1403–1404 (2018).
- van den Brand, R. et al. Restoring voluntary control of locomotion after paralyzing spinal cord injury. *Science* **336**, 1182–1185 (2012).
- Courtine, G. et al. Recovery of supraspinal control of stepping via indirect propriospinal relay connections after spinal cord injury. *Nat. Med.* **14**, 69–74 (2008).
- Bachmann, L. C. et al. Deep brain stimulation of the midbrain locomotor region improves paretic hindlimb function after spinal cord injury in rats. *Sci. Transl. Med.* **5**, 208ra146 (2013).
- Bonizzato, M. et al. Multi-pronged neuromodulation intervention engages the residual motor circuitry to facilitate walking in a rat model of spinal cord injury. *Nat. Commun.* **12**, 1925 (2021).
- Bonizzato, M. & Martinez, M. An intracortical neuroprosthesis immediately alleviates walking deficits and improves recovery of leg control after spinal cord injury. *Sci. Transl. Med.* **13**, eabb4422 (2021).
- Denk, W., Briggman, K. L. & Helmstaedter, M. Structural neurobiology: missing link to a mechanistic understanding of neural computation. *Nat. Rev. Neurosci.* **13**, 351–358 (2012).
- Tomer, R., Ye, L., Hsueh, B. & Deisseroth, K. Advanced CLARITY for rapid and high-resolution imaging of intact tissues. *Nat. Protoc.* **9**, 1682–1697 (2014).
- Chung, K. et al. Structural and molecular interrogation of intact biological systems. *Nature* **497**, 332–337 (2013).
- Epp, J. R. et al. Optimization of CLARITY for clearing whole-brain and other intact organs. *eNeuro* **2**, ENEURO.0022-15.2015 (2015).
- Murray, E. et al. Simple, scalable proteomic imaging for high-dimensional profiling of intact systems. *Cell* **163**, 1500–1514 (2015).
- Renier, N. et al. iDISCO: a simple, rapid method to immunolabel large tissue samples for volume imaging. *Cell* **159**, 896–910 (2014).
- Pan, C. et al. Shrinkage-mediated imaging of entire organs and organisms using uDISCO. *Nat. Methods* **13**, 859–867 (2016).
- Friedli, L. et al. Pronounced species divergence in corticospinal tract reorganization and functional recovery after lateralized spinal cord injury favors primates. *Sci. Transl. Med.* **7**, 302ra134 (2015).
- Liu, Y. et al. A sensitized IGF1 treatment restores corticospinal axon-dependent functions. *Neuron* **95**, 817–833 (2017).
- Renier, N. et al. Mapping of brain activity by automated volume analysis of immediate early genes. *Cell* **165**, 1789–1802 (2016).
- Goubran, M. et al. Multimodal image registration and connectivity analysis for integration of connectomic data from microscopy to MRI. *Nat. Commun.* **10**, 5504 (2019).
- Lein, E. S. et al. Genome-wide atlas of gene expression in the adult mouse brain. *Nature* **445**, 168–176 (2007).
- Wickersham, I. R., Sullivan, H. A. & Seung, H. S. Production of glycoprotein-deleted rabies viruses for monosynaptic tracing and high-level gene expression in neurons. *Nat. Protoc.* **5**, 595–606 (2010).
- Voigt, F. F. et al. The mesoSPIM initiative: open-source light-sheet microscopes for imaging cleared tissue. *Nat. Methods* **16**, 1105–1108 (2019).
- Ritchie, M. E. et al. limma powers differential expression analyses for RNA-sequencing and microarray studies. *Nucleic Acids Res.* **43**, e47 (2015).
- Mickelsen, L. E. et al. Single-cell transcriptomic analysis of the lateral hypothalamic area reveals molecularly distinct populations of inhibitory and excitatory neurons. *Nat. Neurosci.* **22**, 642–656 (2019).
- Stuber, G. D. & Wise, R. A. Lateral hypothalamic circuits for feeding and reward. *Nat. Neurosci.* **19**, 198–205 (2016).
- Saper, C. B., Chou, T. C. & Scammell, T. E. The sleep switch: hypothalamic control of sleep and wakefulness. *Trends Neurosci.* **24**, 726–731 (2001).
- Margules, D. L. & Olds, J. Identical “feeding” and “rewarding” systems in the lateral hypothalamus of rats. *Science* **135**, 374–375 (1962).
- Jennings, J. H., Rizzi, G., Stamatakis, A. M., Ung, R. L. & Stuber, G. D. The inhibitory circuit architecture of the lateral hypothalamus orchestrates feeding. *Science* **341**, 1517–1521 (2013).
- Sinnamon, H. M. & Stopford, C. K. Locomotion elicited by lateral hypothalamic stimulation in the anesthetized rat does not require the dorsal midbrain. *Brain Res.* **402**, 78–86 (1987).

30. Sinnamon, H. M. Locomotor stepping elicited by electrical stimulation of the hypothalamus persists after lesion of descending fibers of passage. *Physiol. Behav.* **48**, 261–266 (1990).
31. Sinnamon, H. M., Lee, S. H., Adams, D. B. & Stopford, C. K. Locomotor stepping elicited by electrical stimulation of the lateral hypothalamus requires an ipsilateral descending pathway. *Physiol. Behav.* **33**, 209–215 (1984).
32. Boyden, E. S., Zhang, F., Bamberg, E., Nagel, G. & Deisseroth, K. Millisecond-timescale, genetically targeted optical control of neural activity. *Nat. Neurosci.* **8**, 1263–1268 (2005).
33. Yizhar, O., Fenno, L. E., Davidson, T. J., Mogri, M. & Deisseroth, K. Optogenetics in neural systems. *Neuron* **71**, 9–34 (2011).
34. Atasoy, D., Aponte, Y., Su, H. H. & Sternson, S. M. A FLEX switch targets channelrhodopsin-2 to multiple cell types for imaging and long-range circuit mapping. *J. Neurosci.* **28**, 7025–7030 (2008).
35. Scheff, S. W., Rabchevsky, A. G., Fugaccia, I., Main, J. A. & Lump, J. E. Jr. Experimental modeling of spinal cord injury: characterization of a force-defined injury device. *J. Neurotrauma* **20**, 179–193 (2003).
36. Asboth, L. et al. Cortico-reticulo-spinal circuit reorganization enables functional recovery after severe spinal cord contusion. *Nat. Neurosci.* **21**, 576–588 (2018).
37. Wang, Z. et al. Brain-wide analysis of the supraspinal connectome reveals anatomical correlates to functional recovery after spinal injury. *eLife* **11**, e76254 (2022).
38. Fenno, L. E. et al. Targeting cells with single vectors using multiple-feature Boolean logic. *Nat. Methods* **11**, 763–772 (2014).
39. Tervo, D. G. R. et al. A designer AAV variant permits efficient retrograde access to projection neurons. *Neuron* **92**, 372–382 (2016).
40. Armbruster, B. N., Li, X., Pausch, M. H., Herlitze, S. & Roth, B. L. Evolving the lock to fit the key to create a family of G protein-coupled receptors potently activated by an inert ligand. *Proc. Natl Acad. Sci. USA* **104**, 5163–5168 (2007).
41. Lüscher, C. & Pollak, P. Optogenetically inspired deep brain stimulation: linking basic with clinical research. *Swiss Med. Wkly.* **146**, w14278 (2016).
42. Chow, B. Y. & Boyden, E. S. Optogenetics and translational medicine. *Sci. Transl. Med.* **5**, 177ps5 (2013).
43. Deisseroth, K. Optogenetics and psychiatry: applications, challenges, and opportunities. *Biol. Psychiatry* **71**, 1030–1032 (2012).
44. Buch, T. et al. A Cre-inducible diphtheria toxin receptor mediates cell lineage ablation after toxin administration. *Nat. Methods* **2**, 419–426 (2005).
45. Dominici, N. et al. Versatile robotic interface to evaluate, enable and train locomotion and balance after neuromotor disorders. *Nat. Med.* **18**, 1142–1147 (2012).
46. Kathe, C. et al. The neurons that restore walking after paralysis. *Nature* **611**, 540–547 (2022).
47. Squair, J. W. et al. Recovery of walking after paralysis by regenerating characterized neurons to their natural target region. *Science* **381**, 1338–1345 (2023).
48. Skinnider, M. A. et al. Single-cell and spatial atlases of spinal cord injury in the *Tabulae Paralytica*. *Nature* **631**, 150–163 (2024).
49. Whiting, D. M. et al. Lateral hypothalamic area deep brain stimulation for refractory obesity: a pilot study with preliminary data on safety, body weight, and energy metabolism. *J. Neurosurg.* **119**, 56–63 (2013).
50. Rupp, R. et al. International Standards for Neurological Classification of Spinal Cord Injury: revised 2019. *Top. Spinal Cord Inj. Rehabil.* **27**, 1–22 (2021).
51. Murphy, J. P. & Gellhorn, E. The influence of hypothalamic stimulation on cortically induced movements and on action potentials of the cortex. *J. Neurophysiol.* **8**, 341–364 (1945).
52. Lorach, H. et al. Walking naturally after spinal cord injury using a brain–spine interface. *Nature* **618**, 126–133 (2023).
53. Rowald, A. et al. Activity-dependent spinal cord neuromodulation rapidly restores trunk and leg motor functions after complete paralysis. *Nat. Med.* **28**, 260–271 (2022).
54. Capogrosso, M. et al. A brain–spine interface alleviating gait deficits after spinal cord injury in primates. *Nature* **539**, 284–288 (2016).
55. Wagner, F. B. et al. Targeted neurotechnology restores walking in humans with spinal cord injury. *Nature* **563**, 65–71 (2018).

**Publisher's note** Springer Nature remains neutral with regard to jurisdictional claims in published maps and institutional affiliations.

Springer Nature or its licensor (e.g. a society or other partner) holds exclusive rights to this article under a publishing agreement with the author(s) or other rightsholder(s); author self-archiving of the accepted manuscript version of this article is solely governed by the terms of such publishing agreement and applicable law.

© The Author(s), under exclusive licence to Springer Nature America, Inc. 2024

<sup>1</sup>Defitech Center for Interventional Neurotherapies (.NeuroRestore), CHUV/UNIL/EPFL, Lausanne, Switzerland. <sup>2</sup>NeuroX Institute, School of Life Sciences, Swiss Federal Institute of Technology (EPFL), Lausanne, Switzerland. <sup>3</sup>Department of Neurosurgery, Lausanne University Hospital (CHUV) and University of Lausanne (UNIL), Lausanne, Switzerland. <sup>4</sup>Department of Clinical Neuroscience, Lausanne University Hospital (CHUV) and University of Lausanne (UNIL), Lausanne, Switzerland. <sup>5</sup>Lewis–Sigler Institute of Integrative Genomics and Ludwig Institute for Cancer Research, Princeton University, Princeton, NJ, USA. <sup>6</sup>Department of Medical Biophysics, University of Toronto, Toronto, Ontario, Canada. <sup>7</sup>Wyss Center for Bio and Neuroengineering, Geneva, Switzerland. <sup>8</sup>ONWARD Medical, Lausanne, Switzerland. <sup>9</sup>These authors contributed equally: Newton Cho, Jordan W. Squair. <sup>10</sup>These authors jointly supervised this work: Jocelyne Bloch, Grégoire Courtine. ✉e-mail: [jocelyne.bloch@chuv.ch](mailto:jocelyne.bloch@chuv.ch); [gregoire.courtine@epfl.ch](mailto:gregoire.courtine@epfl.ch)

## Methods

### Animal maintenance

Adult female C57BL/6 mice ( $\geq 8$  weeks of age at the start of the experiment, 15–30 g body weight) or transgenic male or female mice were used for all experiments. *Vglut2<sup>Cre</sup>* (Jackson Laboratory, 016963) and *Vgat<sup>Cre</sup>* (Jackson Laboratory, 28862) transgenic mouse strains were bred and maintained on a mixed genetic background (129/C57BL/6J). Adult female Lewis rats (200–250 g body weight) were used for the rehabilitation study. Housing, surgery, behavioral experiments and animal killing were all performed in compliance with the Swiss Veterinary Law guidelines. All procedures and surgeries were approved by the Veterinary Office of the Canton of Geneva (Switzerland; license GE/112/20).

### Perioperative care

All preoperative procedures were done according to our established methods<sup>36,46,56,57</sup>. Mouse and rats were anesthetized with a mixture of isoflurane and O<sub>2</sub>. The hair was shaved with a razor, and the surgical site was disinfected with a mixture of betadine/H<sub>2</sub>O<sub>2</sub> followed by 70% ethanol. Excess ethanol was removed, and the eyes were lubricated with vitamin A ointment. The mice and rats were then placed on a heating pad set to 37 °C and maintained on 1–3% isoflurane and O<sub>2</sub>. For longer surgical procedures, vitamin A ointment was reapplied to prevent corneal drying. Postoperatively, mice and rats were placed on a heating pad for 1 week with subcutaneous saline/Ringer's solution daily as needed. Pain control for 48 h postoperatively was also provided with carprofen (Rimadyl, Zoetis; 5 mg kg<sup>-1</sup>) given daily as a subcutaneous injection for mice and buprenorphine (0.05 mg kg<sup>-1</sup>) given twice daily subcutaneously for 2–3 days postoperatively for rats. After SCI, bladders were expressed twice daily until the animals spontaneously regained bladder function. After chronic implant surgery and contusive surgery, amoxicillin (1 ml/100 ml H<sub>2</sub>O) was placed in drinking water for 7 days after surgery.

### Lateral hemisection SCI

A midline skin incision was made using a #10 scalpel blade, and the T10 lamina was identified. After a combination of sharp and blunt muscle dissection, a T10 laminectomy was performed. A left lateral hemisection was then performed using microscissors or a microsurgical blade<sup>46,58</sup>. Any remaining spinal tissue in the hemisection was then scraped away laterally with a needle to ensure the completeness of the lesion. The muscle over the laminectomy was then sutured with 6-0 Vicryl, and the skin was closed with 6-0 Ethilon. Postoperatively, mice were placed on a heating pad and given subcutaneous saline/Ringer's solution or 5% glucose as needed. Only mice that were dragging on the ipsilesional hindlimb at least 3 days after SCI (indicating the adequacy of the lateral hemisection) were included in the study<sup>58</sup>. All hemisection lesions were also confirmed histologically to ensure the adequacy of the lesion.

### Contusion SCI

A midline skin incision was made with a #10 scalpel blade, and the T9 lamina was identified<sup>36,46</sup>. Muscle dissection was performed with a combination of sharp and blunt dissection followed by a T9 laminectomy. The Infinite Horizon impactor (IH-0400 Impactor, Precision Systems and Instrumentation)<sup>35</sup> was calibrated to a force of 75–85 kDyn for mice<sup>36,46</sup>. The laminae rostral and caudal to the laminectomy site were then secured to the clamps of the impactor device, and the spinal cord was positioned centrally and horizontally underneath the impacting element before contusion. In rats, the laminae on each side of the laminectomy were secured, and contusions were performed using the RWD Precise Impactor (RWD Life Sciences, Scintica Instrumentation) set to a speed of 1.5 m s<sup>-1</sup> and depth of 1.85 mm. After contusion, a noticeable bruising of the cord was noticed. The muscle over the laminectomy was then sutured together with 6-0 Vicryl, and the skin was closed with 6-0 Ethilon.

### EMG implantation

EMG implantation in rats was performed<sup>36</sup>. Briefly, bipolar intramuscular electrodes (AS632, Cooner Wire) were inserted into the left medial gastrocnemius (ankle extensor) and left tibialis anterior (ankle flexor). Wires were connected to a head plug (Omnetics Connector Corporation) that was passed subcutaneously to the cranial surface and secured with dental cement and cranial screws.

### Virus production

Viruses used in this study were either acquired commercially or produced locally. The following vectors were used, and sequence information is available as detailed or upon request: AAV5-EF1a-DIO-hChR2(H134R)-EYFP (UNC Vector Core, titer  $4 \times 10^{12}$  genome copies (GC) per ml), AAV5-Ef1a-DIO-eNpHR3.0-eYFP (Addgene, plasmid #26966, titer  $1.1 \times 10^{13}$  GC per ml), AAV5-hSyn-DIO-hM4D(Gi)-mCherry (Addgene, plasmid #44362, titer  $1.2 \times 10^{13}$  GC per ml), AAV-DJ-hSyn-DIO-mGFP-2A-synaptophysin-mRuby (Stanford Vector Core, titer  $2.64 \times 10^{13}$  GC per ml), AAV8-DIO-TC66T-2A-eGFP-2A-oG (Salk Institute, titer  $1.64 \times 10^{13}$  GC per ml), EnvA G-deleted Rabies-mCherry (Salk Institute, titer  $3 \times 10^7$  GC per ml), rAAV-Ef1a-DIO-FLPo-WRPE-hGHPA (Addgene, plasmid #87306,  $1.6 \times 10^{13}$  GC per ml), AAV5-hSyn-Con/Fon-hChR2(H134R)-EYFP (Addgene, plasmid #55645,  $7.7 \times 10^{12}$  GC per ml), rAAV-hSyn-Cre (Addgene, plasmid #105553; titer  $1.9 \times 10^{13}$  GC per ml), AAV5-CAG-DIO-tdTomato (plasmid gifted by S. Arber, titer  $1.9 \times 10^{14}$  vector genomes (vg) per ml), rAAV-hSyn-GFP (Addgene, plasmid #50465, titer  $1.8 \times 10^{13}$  GC per ml), AAV5-hSyn-eGFP (Addgene, plasmid #50465, titer  $1.5 \times 10^{13}$  GC per ml) and AAV5-CAG-DIO-DTR (plasmid gifted by S. Arber, titer  $1.8 \times 10^{13}$  vg per ml). G-deleted rabies viruses were kindly provided by S. Arber, as follows: Rabies-GCVS-RFP (titer  $2.12 \times 10^9$  GC per ml) and Rabies-GCVS-GFP (titer  $3.23 \times 10^9$  GC per ml).

### Cranial viral injections

The cranium was secured with a stereotaxic frame (Kopf Instruments). A skin incision was made with a #10 scalpel blade. The periosteum was removed with fine dissection. Care was taken to ensure that the skull was made level. A craniotomy was made by thinning the bone first using an electric burr, followed by removal of the remaining bone with fine tweezers. Care was taken to keep the dura and underlying brain uninjured and moist with saline. Using a pulled glass pipette (Drummond Scientific Company), injection of AAV5-EF1a-DIO-hChR2(H134R)-EYFP, AAV5-Ef1a-DIO-eNpHR3.0-eYFP, AAV-DJ-hSyn-DIO-mGFP-2A-synaptophysin-mRuby, AAV5-hSyn-Con/Fon-hChR2(H134R)-EYFP, AAV5-CAG-DIO-tdTomato or AAV5-CAG-DIO-DTR was performed in the LH (anterior–posterior (AP): –1.30 mm relative to bregma, medial–lateral (ML):  $\pm 1.00$  mm, dorsal–ventral (DV): –5.25 and –5.30 mm) with 75 nl of the virus at each injection site at a rate of 2 nl s<sup>-1</sup> using a nanoliter pump (Nanoliter 2010 injector, World Precision Instruments). The needle was left in place for 5 min and then slowly removed. For monosynaptic retrograde rabies tracing, 50 nl of AAV8-DIO-TC66T-2A-eGFP-2A-oG was injected at the above coordinates<sup>59</sup>. After 2 weeks, 100 nl per injection of EnvA G-deleted Rabies-mCherry was injected into the LH at the same coordinates. After 7 days, the mice were perfused, and the brains were dissected. Injection of AAV5-hSyn-DIO-hM4D(Gi)-mCherry or rAAV-Ef1a-DIO-FLPo-WRPE-hGHPA was performed in the vGi (AP: –2.30 mm relative to lambda, ML:  $\pm 0.30$  mm, DV: –5.70 mm) with 100 nl of the virus at each injection site at a rate of 3 nl s<sup>-1</sup>. The needle was left in place for 3 min and then slowly removed. In rats, injection of AAV5-CAG-DIO-tdTomato was performed in the LH (AP: –2.75 mm relative to bregma, ML: +1.4 mm, DV: –8.55 mm) with 150 nl of the virus at a rate of 3 nl s<sup>-1</sup> using a nanoliter pump. Injection of rAAV2-hSyn-cre was performed in the vGi as follows: AP: –12 mm from bregma, ML:  $\pm 1$  mm, DV: –8.5 mm with 150 nl of the virus at a rate of 3 nl s<sup>-1</sup> using a nanoliter pump.

### Lumbar spinal cord viral injections

A skin incision was made with a #10 scalpel blade. The ligament between T13 and L1 was then carefully removed to create a window for spinal injections into the lumbar spinal cord. The spine was then secured using a stereotaxic frame (Kopf Instruments). With a pulled glass pipette (Drummond Scientific Company), six injection sites (three on each side of the midline) were then injected each with 100 nl of the virus (50 nl dorsally at 300- $\mu$ m depth and 50 nl ventrally at 600- $\mu$ m depth from the spinal cord surface) at a rate of 3 nl s<sup>-1</sup> using a nanoliter pump (Nanoliter 2010 injector, World Precision Instruments). Both ventral and dorsal injections were made before leaving the needle in place for 2 min and the slow removal of the needle<sup>60</sup>. For hemicord injections, 300 nl of each virus (100 nl per site with 50 nl dorsally and 50 nl ventrally for three sites) was injected laterally on the same side as the hemisection at the T13/L1 spinal level (lower lumbar cord) at 600  $\mu$ m lateral to the midline. Both ventral and dorsal injections were made before leaving the needle in place for 2 min per site and the slow removal of the needle. The muscle was then closed with 6-0 Vicryl, followed by skin closure with 6-0 Ethilon. The laterality of the injection site was confirmed histologically for hemicord injections.

To understand how brain inputs to the lumbar spinal cord change after injury, we used G-deleted rabies viruses as a retrograde tracer from the lumbar cord to label neurons in the brain with direct inputs to the lumbar spinal cord<sup>58</sup>. For hemisected animals, lumbar spinal cord injections ipsilesional to the site of injury (left side) were performed in uninjured mice and mice 1 and 8 weeks after injury. For contused animals, bilateral lumbar spinal cord injections were performed 8 weeks after injury. Four days of viral expression were allowed before mouse perfusion. Mouse brains were collected and subjected to clearing, imaging and brain registration.

### DBS electrode implantation

Mice or rats were placed in a stereotaxic frame (Kopf Instruments). A midline skin incision was made, and the underlying periosteum was dissected bluntly. The bregma and coronal sutures were identified, and cranial screws were inserted into the skull around the proposed site of electrode implantation. A craniotomy was then performed centered on the point of insertion for the right-sided LH. The stimulation electrode (PI-SNE-100, Science Products) was then lowered using the stereotaxic frame into the right LH (mouse coordinates, AP: -1.30 mm relative to bregma, ML: +1.00 mm, DV: -5.05 mm; rat coordinates, AP: -2.75 mm, ML: +1.4 mm relative to bregma, DV: -8.55 mm relative to the dural surface). Kwik-Cast sealant (World Precision Instruments) was then placed on the exposed cortex and around the electrode insertion site. Dental cement was then placed around the electrode and cranial screws to secure it in place. Excess skin was then sutured together around the dental cement.

### Whole-brain clearing sample preparation

Adult mice were deeply anesthetized with an intraperitoneal injection of pentobarbital (150 mg kg<sup>-1</sup>). Intracardiac perfusion was then performed first with 1 $\times$  PBS, followed by 4% paraformaldehyde (PFA) in PBS. Dissection of the brain and spinal cord was then performed, and the sample was postfixed in 4% PFA overnight at 4 °C. Samples were stored in 1 $\times$  PBS with 0.02% sodium azide at 4 °C until further processing.

### iDISCO+

iDISCO+ was used to immunolabel and clear the mouse brains<sup>14,18</sup>. Briefly, the samples were pretreated with methanol in 5-ml Eppendorf tubes by dehydrating with a methanol/H<sub>2</sub>O series at 1 h each at room temperature: 20%, 40%, 60%, 80% and 100%. This was followed by further washing the samples with 100% methanol for 1 h and then chilling them at 4 °C. The samples were then incubated overnight with shaking in 66% dichloromethane/33% methanol at room temperature. They

were then washed twice in 100% methanol at room temperature and then bleached in chilled fresh 5% H<sub>2</sub>O<sub>2</sub> in methanol overnight at 4 °C. The samples were then rehydrated with a methanol/H<sub>2</sub>O series (80%, 60%, 40%, 20%) and PBS, each for 1 h at room temperature. They were then washed for 1 h two times at room temperature in PTx.2 buffer (1 $\times$  PBS and 0.2% Triton X-100). The samples were then incubated each in 4.5 ml of permeabilization solution (400 ml PTx.2, 11.5 g glycine, 100 ml dimethyl sulfoxide (DMSO) for a total stock volume of 500 ml) for 2 days at 37 °C with shaking. This was followed by incubation in 4.5 ml of blocking solution (42 ml PTx.2, 3 ml normal donkey serum, 5 ml DMSO for a total stock volume of 50 ml) for 2 days at 37 °C with shaking. The samples were then incubated in a primary antibody solution consisting of PTwH (1 $\times$  PBS, 2 ml Tween 20, 1 ml of 10 mg ml<sup>-1</sup> heparin stock solution for a total stock volume of 1 l), 5% DMSO, 3% normal donkey serum and cFos (rabbit anti-cFos, 1:2,000, Synaptic Systems, #226 003) for a total volume of 4.5 ml per sample. The samples were incubated in the primary antibody solution for 7 days at 37 °C with shaking. The samples were then washed in PTwH for 24 h and then incubated in a secondary antibody solution consisting of PTwH, 3% normal donkey serum and donkey anti-rabbit Alexa Fluor 647 (1:500, Thermo Fisher Scientific) for a total solution volume of 4.5 ml per sample. The samples were incubated in the secondary antibody solution for 7 days at 37 °C with shaking. The samples were then washed in PTwH for 24 h, and final clearing was performed<sup>18</sup>. Briefly, samples were dehydrated in a methanol/H<sub>2</sub>O series, as follows: 20%, 40%, 60%, 80% and 100%, two times each for 1 h at room temperature. Then, they were incubated for 3 h with shaking in 66% dichloromethane/33% methanol at room temperature. This was followed by incubation in 100% dichloromethane for 15 min two times with shaking to wash out residual methanol. Finally, the samples were incubated in dibenzyl ether without shaking for refractive index matching of the solution for at least 24 h before imaging.

### CLARITY

Clearing of mouse brains was performed using CLARITY<sup>11,61</sup>. Briefly, after the removal of the dura, whole mouse brains were each incubated in 10 ml of A4P0 hydrogel solution with gentle nutation at 4 °C for 24 h. The samples were then degassed with N<sub>2</sub> for 3 min and then placed in a water bath at 37 °C for 2 h to initiate polymerization. Commercial polymerization (Logos Biosystems) was also used as available. Excess hydrogel was removed, and the samples were washed in 0.001 M PBS for 5 min at room temperature. Then, the samples were cleared using the X-CLARITY system (Logos Biosystems) at 1.2–1.5 A, 100 rpm and 37 °C using a 4% SDS clearing solution. The samples were then washed at room temperature in 1 $\times$  PBS with 0.1% Triton X-100 for 24 h to remove residual SDS. The samples were then incubated in RIMS solution (refractive index 1.45–1.485) for at least 24 h before imaging.

### Optogenetic experiments

Optic fiber implantation was performed at the same time as viral delivery. After viral delivery, the optic ferrule (230- $\mu$ m diameter, Thorlabs) was attached to the stereotaxic frame (Kopf Instruments) and carefully lowered over the craniotomy site at the desired coordinates. The tip of the optic fiber was then slowly directed into the right LH (AP: -1.30 mm relative to bregma, ML: +1.00 mm, DV: -5.05 mm). A drop of biocompatible glue was placed around the area of optic fiber insertion (Kwik-Cast sealant, World Precision Instruments) to protect the underlying cortical surface of the brain. Dental cement, mixed with carbon to prevent light-scattering effects, was then used in combination with cranial screws to secure the ferrule in place<sup>36,46</sup>. Light was transmitted using a ferrule-to-ferrule connection cable. An external stimulator (A-M Systems) was used to drive laser pulses at the desired pulse length and frequency. Optogenetic stimulation and inhibition of the LH were performed in hemisected animals after spontaneous recovery occurred (at least 7–8 weeks after injury). Correct placement of the optic fiber and injection of the virus were confirmed histologically.

Blue light stimulation (Laserglow, 473-nm blue DPSS laser system) was delivered at 40 Hz, 5-ms pulses with -1–20 mW to the right-sided LH. In *Vglut2<sup>Cre</sup>* mice, we determined the optimal frequency of LH stimulation with frequency ramp-up experiments, which were performed to compare the effects on walking of blue light stimulation at 5, 10, 20 and 40 Hz relative to no light stimulation in chronically hemisected animals. In *Vgat<sup>Cre</sup>* mice, stimulation at higher intensities resulted in a strong chewing or feeding response during which time the animal would not walk. The intensity was decreased until the animal still demonstrated a chewing response but also could be motivated to walk across the runway. Finally, for the stimulation of AAV5-Ef1a-DIO-eNpH R3.0-eYFP-infected neurons, continuous yellow light (Laserglow, 589-nm yellow DPSS laser system) was delivered at -10–15 mW. As an additional control, the same parameters of blue and yellow light delivery were applied to animals infected with a reporter-only virus. Control experiments were conducted by delivering a reporter-only virus, AAV-DJ-hSyn-DIO-mGFP-2A-synaptophysin-mRuby, to assess for nonspecific stimulation effects. The reporter-only virus was injected 6 weeks after injury, and 4 weeks were allowed for viral expression before kinematic testing and then perfusion for histological analysis. Finally, as an internal control to assess the effect of heat-related alteration of neuronal function, yellow light (Laserglow, 589-nm yellow DPSS laser system) was delivered at 40 Hz, 5-ms pulses with -20 mW to the right-sided LH<sup>36</sup>.

### DREADD inactivation experiments

Viral delivery was performed as described in the vGi of the brainstem. Testing was performed in mice at least 7–8 weeks after lateral hemisection and 15–60 min after intraperitoneal injection of clozapine-*N*-oxide (Carbosynth, 5 mg kg<sup>-1</sup> of body weight, diluted in 0.9% NaCl)<sup>36,46</sup>, both with and without 473-nm light to activate AAV5-Ef1a-DIO-hChR2(H13 4R)-EYFP-infected neurons in the right LH. Intraperitoneal injection of saline served as an internal control for each animal.

### Behavioral assessments

For our cFos whole-brain labeling behavioral task for hemisected animals, mice were trained to run on a treadmill quadrupedally (Robo-medica) 5 days a week for 2 weeks before hemisection injury<sup>46</sup>. After hemisection and a 1-week recovery period, maintenance training occurred twice per week to maintain proficiency on the task but to avoid training-dependent changes in plasticity and gait performance<sup>58</sup>. On the day of perfusion, mice were made to run on the treadmill for 45 min at a speed of 9 cm s<sup>-1</sup> and then perfused 1 h after the end of the task. The speed was kept constant to avoid confounds of brain activity related to differences in walking speed<sup>62</sup>. To avoid confounds of walking in the home cage after the task for uninjured and hemisected animals that may be quite active, we placed mice in a small box filled with bedding 1 h before and 1 h after the task before perfusion. Mice were acclimated to this box 1 week before the task to reduce brain-related changes secondary to exploratory behavior and walking. All tasks were performed in the morning between 8 AM and 12 PM for each group to avoid confounds in brain activity dependent on the time of day. Uninjured mice and mice at 1 and 8 weeks after SCI were perfused for analysis. Before perfusion, kinematic recordings on the treadmill were performed. Mouse brains were collected and subjected to clearing, imaging and brain registration.

### Kinematic recordings

Detailed procedures were fully outlined previously<sup>4,36,45,46,57,63</sup>. In brief, hindlimb kinematics were recorded using the Vicon motion capture system (Vicon Motion Systems) with 12 infrared cameras (200 Hz). Reflective markers were attached bilaterally to the mouse iliac crest, greater trochanter (hip), lateral condyle (knee), malleolus (ankle) and metatarsal-phalangeal joint (foot). For the rat, markers were attached bilaterally to the iliac crest, greater trochanter (hip), lateral condyle

(knee), malleolus (ankle) and metatarsal-phalangeal joint (foot) for quadrupedal recordings. For bipedal recordings, a toe marker was also added. A 3D reconstruction of the markers was then performed offline using Vicon Nexus software, and gait parameters for each gait cycle were determined using custom MATLAB scripts developed previously<sup>45</sup>. EMG recordings were performed using the Vicon motion capture system. The frequency of the signal was set to 2,000 Hz. The EMG recordings were then analyzed using custom MATLAB scripts for representative tracings during different conditions throughout the study. Kinematic files and videos that could not be properly processed were excluded from the analysis. Animals that were not cooperative in a particular task were excluded from the analysis for that task.

For mice, at least ten gait cycles were recorded for each animal from trials on the treadmill or an elevated runway. For the chronic implant test in uninjured rats, 1 week after implantation, at least ten gait cycles were recorded for each condition quadrupedally on an elevated runway. The threshold was defined as the amplitude of LH stimulation when the animal began exhibiting sudden chewing behavior. DBS in rats was performed at a frequency of 50 Hz with 0.2-ms pulses. The amplitude of stimulation was increased in increments of 10% of the threshold until a maximum amplitude of 1.5× the threshold was reached. For recordings in rats undergoing bipedal rehabilitation, at least ten gait cycles were recorded for each condition on the runway. The stimulation intensity of DBS<sup>LH</sup> for these recordings was personalized to each rat to elicit the maximal possible response.

### Structured robot-assisted rehabilitation in rats

Rats underwent a structured rehabilitation program for 8–10 weeks, as previously outlined<sup>4</sup>. The training regimen involved sessions conducted 5 days a week, each lasting 25 min. Initially, the training commenced with bipedal walking on a treadmill set at a speed of 11 cm s<sup>-1</sup>, with adjustable body weight support provided by the Robo-medica system. Following the completion of 1 week of treadmill training, the rats were transitioned to overground training settings using a custom-built robotic weight support system, as described in our prior work<sup>4,45,63</sup>. During the overground training sessions, the rats received DBS<sup>LH</sup> characterized by a 0.2-ms pulse width, 40- to 200-μA amplitude and 50-Hz frequency. This stimulation protocol was administered during each overground run.

### Immunohistochemistry

The spinal cords from lesioned mice after perfusion were postfixed overnight at 4 °C in 4% PFA/1× PBS to assess hemisection lesions. They were then placed in 30% sucrose/0.1 M phosphate buffer (PB) for at least two to three nights before embedding in cryomatrix and freezing. Coronal sections of 40-μm thickness were then cut from a piece of the thoracic spinal cord centering around the lesion. These sections were then processed with hematoxylin and eosin staining to delineate lesion scar from normal tissue. More specifically, slides with coronal sections of the spinal cord were sequentially incubated in various solutions to complete the hematoxylin and eosin staining as follows: Mayer's hematoxylin for 5 min, tap water for 2 min, distilled water for 1 min, HCl-ethanol for 30 s, tap water for 3 min, 0.5% eosin for 40 s, tap water for 1 min, 70% ethanol for 1 min, 96% ethanol for 3 min, 100% ethanol for 3 min, 100% ethanol for 3 min and xylene for 5 min. Slides were then manually coverslipped with Pertex mounting medium (Histolab Products) and left to dry at room temperature before imaging.

To assess the lesion area after contusion, we performed immunohistochemistry<sup>36,60,64</sup>. The spinal cords from lesioned mice and rats after perfusion were postfixed overnight at 4 °C in 4% PFA/1× PBS. They were then placed in 30% sucrose/0.1 M PB for at least two to three nights before embedding in cryomatrix and freezing. Coronal sections of 40-μm thickness were then cut from a piece of the thoracic spinal cord centering around the lesion. Lesion visualization was then performed using glial fibrillary acidic protein (GFAP)

immunohistochemistry. Sections were washed two to three times in 0.1 M PBS and blocked using 1% Triton X-100 and 5% normal goat serum in 0.1 M PBS for 1 h at room temperature. This was followed by incubation in a rabbit anti-GFAP (1:1,000, Dako) primary antibody diluted in 1% Triton X-100 and 2% normal goat serum in 0.1 M PBS overnight at 4 °C. Thereafter, the samples were washed three times in 0.1 M PBS and incubated in a goat anti-rabbit Alexa Fluor 647 (1:400, Thermo Fisher Scientific) secondary antibody diluted in 1% Triton X-100 and 2% normal goat serum in 0.1 M PBS for 1 h at room temperature. Samples were then washed once in 0.1 M PBS followed by incubation in DAPI (1:1,000, Thermo Fisher Scientific) diluted in 0.1 M PBS for 20 min. The samples were then washed again in 0.1 M PBS three times before air-drying and coverslipping with Mowiol.

To confirm LH activation, we performed cFos staining to verify neuronal activation after optogenetic stimulation and DBS. Hemisected mice infected with AAV5-EF1a-DIO-hChR2(H134R)-EYFP and AAV-DJ-hSyn-DIO-mGFP-2A-synaptophysin-mRuby were each stimulated optogenetically continuously for 10 min at 20 Hz at -20 mW. They were then left in their home cage for 60 min before perfusion. In rats implanted with a chronic electrode in the right LH, cFos activation was elicited by anesthetizing the animals using a mixture of 25% ketamine and 10% medetomidine in saline. A 0.4- to 0.8-ml volume of the mixture was administered intraperitoneally in the rats, and 90 min of stable anesthesia was provided. The right LH was then stimulated at 50 Hz with 0.2-ms pulses for a total of 15 min (cycles of 20 s ON and 10 s OFF). The amplitude of stimulation was adjusted until there was an increase in breathing rate with stimulation, which is reliably seen with LH stimulation. Rats were perfused 45 min after the completion of stimulation. Control rats received only anesthesia without electrode implantation and subsequent LH stimulation.

After perfusion, mouse and rat brains were postfixed overnight at 4 °C in 4% PFA/1× PBS. They were then placed in 30% sucrose/0.1 M PB for at least two to three nights before embedding in cryomatrix and freezing. Coronal sections of 40- $\mu$ m thickness were then cut and stored free-floating in 0.1 M PB with 0.03% sodium azide. Slices were first washed in 0.1 M PBS for 5 min, followed by washing for 10 min. They were then blocked with 0.5% BSA with 0.3% Triton X-100 in 0.1 M PBS for 1 h at room temperature. This was followed by incubation in primary antibody diluted in blocking solution for two nights (rabbit anti-cFos, 1:500, Synaptic Systems, #226 003) at room temperature with shaking. The slices were then washed for 5, 10 and 15 min with 0.1 M PBS with shaking at room temperature. This was followed by secondary antibody incubation (goat anti-rabbit Alexa Fluor 647, 1:400, Thermo Fisher Scientific) in blocking solution for 90 min at room temperature in the dark with shaking. The slices were again washed for 5 min and then for 10 min, followed by a 15-min incubation in DAPI (1:1,000, Thermo Fisher Scientific) diluted in 0.1 M PBS. This was followed by a final 15-min wash in 0.1 M PBS with shaking at room temperature. The slices were then mounted on slides and allowed to air-dry, followed by coverslipping with Mowiol.

To visualize LH<sup>vGi</sup> synaptic connections, we immunolabeled vGi slices using a mouse anti-vGlut2 antibody (1:1,000, Millipore, MAB5504) and a guinea pig anti-Homer1 antibody (1:600, Synaptic Systems) and incubated them overnight at room temperature, followed by a 2-h incubation with goat anti-mouse Alexa Fluor 405 (1:250, Thermo Fisher Scientific) and goat anti-guinea pig Alexa Fluor 647 (1:250, Thermo Fisher Scientific). Slices were then mounted on slides, and synaptic contacts to vGi neurons were imaged at high resolution using an LSM 880 confocal microscope. Images were processed using Imaris for visualization. We manually quantified the number of vGi<sup>lumbar</sup> neurons receiving at least one Vglut2<sup>+</sup>/Homer1<sup>+</sup> LH<sup>vGi</sup> synaptic connection. As all vGi<sup>lumbar</sup> neurons received such connections, we further manually quantified the number of Vglut2<sup>+</sup>/Homer1<sup>+</sup> LH<sup>vGi</sup> synaptic connections that each vGi<sup>lumbar</sup> neuron received, based on high-resolution confocal images.

Finally, to visualize and confirm the location of LH electrode implantation, we stained the slices with Nissl dye. Brain slices collected on object slides were first washed with 0.1 M PBS for 5, 10 and 15 min. They were then incubated with NeuroTrace (1:50, Thermo Fisher Scientific) diluted in 0.1 M PBS for 30 min at room temperature at a volume of 200  $\mu$ l per slide. Slides were then washed with 0.1 M PBS for 5 and 10 min and then left to air-dry at room temperature. Slides were then coverslipped with Mowiol and stored at 4 °C protected from light until imaging.

### Fluorescence in situ hybridization

To quantify the number of Vglut2<sup>+</sup> neurons in the LH after diphtheria toxin receptor ablation, we performed RNA in situ hybridization against Vglut2 mRNA on 40- $\mu$ m brain slices according to a standard protocol. Briefly, samples were placed in 5× SSCT (20× SSC buffer, Invitrogen; 10% Tween 20, Applichem) for 10 min and then prehybridized in 30% probe hybridization buffer (Molecular Instruments) for 30 min at 37 °C. Samples were hybridized overnight at 1  $\mu$ M probe concentration (Mouse-VGLUT2-B1, Molecular Instruments) in a 30% probe hybridization buffer at 37 °C. Following hybridization, samples were washed in a solution of 30% probe wash buffer (Molecular Instruments) and 5× SSCT four times for 15 min per wash. Sections were then incubated in an amplification buffer (Molecular Instruments) for 30 min at room temperature. Amplification was performed overnight at room temperature at a concentration of 120 nM per hairpin (Molecular Instruments) in the amplification buffer. Quantification of Vglut2<sup>+</sup> cells within the LH was performed using segmentation algorithms in QuPath (v0.4.3)<sup>65</sup>.

### Imaging

Imaging of cFos iDISCO+ whole brains was performed using a custom-built COLM<sup>10</sup>. This system offers a pixel resolution of 1.4 × 1.4 × 5  $\mu$ m in the *x*, *y* and *z* dimensions, respectively, using the 4×/0.28 (d) objective, which is ideal for resolving cell nuclei labeled by cFos. Whole brains were placed in a custom-made quartz cuvette filled with dibenzyl ether, which was then attached to a stage that was lowered into an oil immersion medium. Given the potential for intensity variability of cFos staining, all acquisitions were performed using the same microscope parameters. For all brains, one channel with autofluorescence ('auto' channel, 488 nm) to demonstrate anatomy was imaged, and the other channel demonstrating cFos labeling ('cell' channel, 647 nm) was imaged<sup>18</sup>. All raw images were acquired as 16-bit TIFF files and were stitched together using TeraStitcher at maximal resolution<sup>66</sup>. The cell channel was stitched first, and the merge XML file from this channel was then used to stitch the auto channel to ensure equivalent dimensions in all axes between the two channels.

Imaging of whole brains with rabies labeling, which were processed with CLARITY, was performed using a custom-built lightsheet mesoSPIM<sup>22</sup>. The expansion of the brain observed with CLARITY considerably increases the size of the image files when using the COLM. The mesoSPIM allows a fast whole-brain scan and provides a resolution sufficient for single-neuron detection. Imaging was performed at 0.8× zoom with a resulting pixel resolution of 8.23 × 8.23 × 5  $\mu$ m in the *x*, *y* and *z* dimensions. Accordingly, the whole brain could be imaged in a single field of view (FoV) without the need for stitching while still resolving individual neurons. All raw images were acquired as 16-bit TIFF files, with one channel imaged for autofluorescence (488 or 561 nm) and the other respective channel imaged for viral labeling.

Imaging for whole mouse CNS and rat brains was performed using a 1.25× or 2.5× zoom factor at the mesoSPIM for overview images and a 4×/0.28 (d) or 10×/0.8 (d) objective at the COLM targeting the region of interest, using one or two light sheets illuminating the sample from the left and right sides. The voxel resolution in the *x*, *y* and *z* directions was 5.3 × 5.3 × 5  $\mu$ m for the 1.25× acquisition and 2.6 × 2.6 × 3  $\mu$ m for the 2.5× acquisition. The voxel resolution of the COLM was 1.4 × 1.4 × 5  $\mu$ m for the 4× acquisition and 0.59 × 0.59 × 3  $\mu$ m for the 10× acquisition.

Images were generated as 16-bit TIFF files and then stitched using TeraStitcher. All 3D reconstructions and optical sections of raw images were generated using Imaris software.

All other imaging was performed using an Olympus slide scanner VS120-L100 microscope or a Zeiss LSM 880 confocal microscope. Airyscan acquisition was performed at 20× magnification.

### Whole-brain atlas registration and cell quantification

Registration of whole cleared mouse brains to the mouse Allen Brain Atlas was performed in an automated fashion using MIRACL (Multi-modal Image Registration And Connectivity Analysis)<sup>19</sup>. To provide MIRACL with a binary, segmented image stack, we proceeded separately for cFos (processed with iDISCO+) and rabies (processed with CLARITY) brains due to the unique features of cFos staining (nuclear in nature) versus rabies labeling (whole neurons). For cFos brains, segmentation was performed using a customized macro based on Fiji plugins to preprocess images in combination with the Arivis Vision4D (Arivis) platform. Downsampling of images by a factor of 2 was first performed to reduce the data footprint. Preprocessing of raw images was performed to remove the background and enhance contrast in Fiji. Images were then imported into the Arivis Vision4D platform, and the Blob Finder segmentation algorithm was used to detect cFos<sup>+</sup> nuclei or cells in an automated fashion. We opted to use the highest threshold of detection on the Blob Finder platform to ensure that segmented nuclei were likely to be true nuclei. The same settings were applied to all mouse brains in each group. Images corresponding to segmented cFos-labeled nuclei and cells were then exported as a TIFF stack and binarized in Fiji. The binarized image was then imported into MIRACL<sup>19</sup> to perform brain region-specific counts based on registration to the Allen Brain Atlas.

For rabies-labeled neurons, the Arivis Vision4D platform was used to segment neuronal cell bodies in a semiautomated fashion. Preprocessing background subtraction using Arivis Vision4D was first performed. The presence of some blood vessels and residual axons made the segmentation of neuronal soma more complicated to perform reliably in a fully automated fashion. In this regard, we opted to adopt a semiautomated approach by using the Blob Finder segmentation algorithm of Arivis Vision4D on the preprocessed image stacks. The settings of the Blob Finder, including the diameter of detection, threshold of detection and split sensitivity, were iteratively changed until satisfactory labeling and splitting of neurons were observed. The pipeline was then run throughout the various regions of the whole mouse brain noted to have neurons. This was followed by the manual removal of Vision4D annotations that were not neuronal soma, including portions of axons and blood vessels. Raw images of both the autofluorescence and cell channels were cross-referenced with the segmented images to ensure that blood vessels were not counted as neurons. An annotation mask was then created and saved as a TIFF stack, which was then binarized and used to perform cell counts within each brain region using the registration with the Allen Brain Atlas through MIRACL<sup>19</sup>.

### Spinal cord lesion quantification

Olympus VS desktop software was used to quantify lesions from images acquired using the Olympus slide scanner VS120-L100 microscope, as we have previously described<sup>36,46</sup>. One slice demonstrating the greatest lesion area (lesion epicenter) and one to two normal slices above and below the epicenter were chosen. The interpolated polygon function was used to trace and determine the area of the spared tissue at the epicenter and the areas of the slices above and below the epicenter. The average area of the slices above and below the epicenter was calculated, and the spared tissue was expressed as a percentage of this average area. The percent lesion was then calculated by subtracting the percent spared from 100%. Note that, for contusion injuries, some animals demonstrated substantial spreading of the lesion rostrally and distally, especially along the dorsal aspect of the cord. In these cases,

slices that most closely approximated normal morphology above and below the epicenter were chosen.

### Quantification of cFos activation

Quantification of optogenetic cFos activation was performed by selecting four slices immediately surrounding the site of electrode implantation. Quantification of DBS-related cFos activation was performed by selecting the slice at the site of electrode implantation. Cell counts were performed with QuPath using the 'Cell detection' function on images obtained with the Olympus slide scanner VS120-L100 microscope, as previously described<sup>65</sup>.

### Output analysis of glutamatergic neurons of the LH

Three to five tissue slices were imaged per region per animal. Confocal images were background-subtracted in Fiji/ImageJ, followed by the generation of a maximum intensity projection of the tissue slice imaged per region. A custom Fiji/ImageJ script was then used to manually trace the region of interest in each maximum intensity projection, followed by automatic thresholding to isolate axons. The density of positive pixels (as a proxy for axon fiber density) was then calculated for each tissue slice, and tissue slices were averaged for each region for each animal. The average pixel (fiber) density was then compared across regions. To assess vGlu<sup>+</sup>l<sup>umbar</sup> synaptic connections to Vsx2 neurons, we stained lumbar sections with a rabbit anti-Chx10 antibody (1:500, Novus Biologicals, #NBP1-84476), a guinea pig anti-NeuN antibody (1:500, Millipore, #ABN90P) and a mouse anti-vGlu<sup>+</sup>l<sup>umbar</sup> antibody (1:1,000, Millipore, MAB5504). We then manually quantified the number of Vsx2 neurons receiving at least one vGlu<sup>+</sup>l<sup>umbar</sup> synaptic connection in three lumbar sections per animal.

### Stress response quantification

The stress response to DBS in rats was assessed using the Rat Grimace Scale<sup>67</sup>. Videos focusing on the facial features of the rats were obtained. To guarantee the capture of stress responses, we captured short video segments to ensure that the stimulation was on long enough to induce a stress response, if present. Although the original Rat Grimace Scale protocol involved the use of still photos, we opted to use short video segments to capture the facial features fully during stimulation. These video segments were blinded and assessed by two independent evaluators. Four parameters were evaluated for each rat: orbital tightening, nose/cheek flattening, ear changes and whisker changes. For each parameter, a score of 0–2 was given, with 0 indicating the absence of the parameter and 2 demonstrating the obvious presence of the parameter. Scores were collected for all rats and averaged across the two evaluators to result in a composite score for each animal for the DBS<sup>LH</sup> ON and DBS<sup>LH</sup> OFF conditions. The animals' scores were then averaged for each condition and expressed as a percentage of the maximal average score (of 2) for statistical comparison between DBS<sup>LH</sup> ON and DBS<sup>LH</sup> OFF.

### Neuromorphological quantification

To quantify the vGlu<sup>+</sup>l<sup>umbar</sup> projections in rats, we chose a minimum of five sections per rat, evenly between the spinal cord L2 and L4 segments. Images were acquired with high-resolution settings using an Olympus slide scanner. The experimenter was blinded to the images, and the fiber density of axonal projections was measured and analyzed using custom-written scripts in Fiji. Images were divided into regions of interest corresponding to the gray matter, and densities were computed within each region of interest as the ratio of pixels for segmented fibers to the total pixels of gray matter. Files were color-filtered and binarized by means of an intensity threshold. Threshold values were set empirically and maintained within the same range across sections, animals and groups.

### Principal component analysis

Briefly, reconstructed kinematic data were processed with custom MATLAB scripts to compute gait parameters. The limbs were modeled



as an interconnected chain of segments, and gait parameters were calculated from the recordings. To evaluate differences between experimental conditions, as well as to identify the most relevant parameters to account for these differences, we implemented a multistep multifactorial analysis based on principal component analysis, which we described in detail previously<sup>36,57,58</sup>. For each experiment, a principal component analysis was performed by computing the covariance matrix  $A$  of the ensemble of parameters over the gait cycle, after subtracting their respective mean values. The principal components were computed from eigenvalues  $\lambda_i$  and eigenvectors  $U_i$  of  $A$ . The principal components were ordered according to the amount of data variance accounted for by each component. The coordinate of each gait cycle on the first principal component, that is, the component vector explaining the greatest amount of variance across the gait parameters, was thereafter referred to as the walking score. This score was then scaled from 0 to 1 for each experiment to provide a natural comparison that estimates that change across groups. Individual parameters were then selected to be compared between groups based on their correlation to the first principal component. All statistical analyses were conducted at the level of individual mice, after taking the mean of each principal component or outcome measure for each biological replicate (mouse or rat).

### Statistical procedures

All statistical analyses were conducted as  $t$  tests, paired  $t$  tests, one-way analysis of variance or repeated-measures one-way analysis of variance, as appropriate. All graphs show mean values, and all bar graphs are overlaid with dot plots in which each dot represents the value for one animal. For whole-brain analysis (cFos and rabies), cell counts within each brain region annotated in the Allen Brain Atlas were tabulated. As these count data naturally follow the expected mean–variance relationship, differential activation (cFos) and differential residual projections (rabies) were assessed using linear models with empirical Bayesian stabilization<sup>23</sup>. In this case, regions were ranked by their nominal  $P$  values for each a priori biological hypothesis. The statistical significance level was set to  $P < 0.05$ . Unless otherwise indicated,  $P$  values in the figures are represented as follows: \* $P < 0.05$ , \*\* $P < 0.01$  and \*\*\* $P < 0.001$ .

### Human fMRI experiment pilot project

fMRI experiments on a non-SCI population were carried out as part of a pilot project (CER-VD protocol 207/10, version 23.06.2014). To show associated neural activity, we engaged five individuals in bipedal lower-limb motor tasks while an fMRI was performed.

Participants were lying in the MRI scanner and asked to perform monopodal and bipedal foot flexion/extension movements in a visually cued block-design paradigm. Each block consisted of eight monopodal or bipedal movements cued externally every 2 s by a visual symbol depicting the corresponding body part. The 21 blocks (7 monopodal, 14 bipedal; that is, 168 movements in total) were interspersed with an equal number of rest periods (fixation cross for 16 s). Before each block, the participants saw a brief instruction about the upcoming task to perform, followed by a countdown of 3 s. The order of movements was balanced and pseudorandomized.

The participants' real-time behavioral performance during the fMRI data acquisition was collected using a magnetic resonance-compatible pneumatic device. Air pressure sensors transduced pressure into an electrical signal after the gain amplification, and the resulting output was sent to Signal 6 software through a CED MICRO3 1401 data acquisition unit (Cambridge Electronic Design Limited) at a sampling rate of 500 Hz. Motor response peaks were detected using a modified version of a previously published algorithm<sup>68</sup>.

MRI data were acquired on a Siemens Prisma 3-T scanner using a 64-channel head coil. Functional images were acquired using a 3D multishot echo-planar imaging (EPI) sequence<sup>69</sup> at 2-mm isotropic voxel size (number of volumes: 239, 60 axial slices parallel to the anterior commissure–posterior commissure line, matrix size: 92 × 92, slice repetition

time (TR) = 52 ms, volume TR = 3.328 s, echo time (TE) = 30 ms, flip angle  $\alpha = 15^\circ$ , slice oversampling: 6.7%). Anatomical data were acquired at 1.5-mm voxel size (matrix size: 160 × 150 × 120, FoV: 256 × 240 × 176 mm) using a 3D fast low-angle shot (FLASH) sequence, providing estimates of the longitudinal relaxation rate, effective proton density, magnetization transfer and transverse relaxation rate<sup>70</sup>.

All steps of data processing and analysis were performed in the framework of SPM12 (Wellcome Trust Centre for Neuroimaging, [www.fil.ion.ucl.ac.uk/spm](http://www.fil.ion.ucl.ac.uk/spm)) running under MATLAB 7.13 (The MathWorks). Functional data were realigned to the session mean, corrected for receive coil inhomogeneities and EPI distortion<sup>71</sup>, and coregistered to the high-resolution structural data. This was followed by spatial smoothing using a 3D Gaussian kernel of 3-mm full width at half maximum.

For fMRI analysis, we used the generalized linear model with all cued and noncued movements as separate events, the preparation periods as epochs of 3 s and spatial realignment parameters—six parameters encoding for  $x$ ,  $y$  and  $z$  displacement, as well as pitch, yaw and roll—as nuisance variables. In all generalized linear model fits, we removed low-frequency drifts and used a canonical hemodynamic response function to convolve the events. Testing for main effects at the subject level, we created contrasts corresponding to each cued movement (right and left feet separately or right and left hands separately). These models were then used as the outcome measure in a mixed-effect linear model wherein a random effect was included for participants and fixed effects for sex and age. The adjusted estimate and  $P$  value for this final second-level model are reported.

### DBS<sup>LH</sup> clinical study design and objectives

All clinical experiments were carried out as part of the ongoing clinical feasibility study HoT-DBS, which investigates the safety and effectiveness of DBS<sup>LH</sup> in acutely augmenting leg motor function and acting as an adjunct to rehabilitation in patients with chronic SCI. This study was approved by the Swiss authorities (Swissethics reference no. 2021-00095, Swissmedic reference no. 10000839) and conducted in accordance with the Declaration of Helsinki. All participants signed a written informed consent form before their participation. Additional consent for the publication of identifiable images was obtained from each participant. More information is available at [www.clinicaltrials.gov](http://www.clinicaltrials.gov) (NCT04965727). All surgical and experimental procedures were performed at the Lausanne University Hospital. The study involved assessments before surgery, the surgical implantation of the neurostimulation system, a 1-week DBS calibration period, a 3-month rehabilitation period with physiotherapists taking place three times per week for 3 h, and 3 months of independent use of the DBS system. The rehabilitation program was personalized based on the participants' improvements. At the end of the independent-use period, the participants were given the opportunity to be enrolled in a study extension phase during which they could continue using the DBS system at home. Safety was assessed through adverse events reporting and vital signs, weight and hormonal monitoring (adrenocorticotropic hormone, thyroid-stimulating hormone, free thyroxine, morning serum cortisol, prolactin and testosterone). Data are reported in Table 1 and Supplementary Table 2.

### DBS<sup>LH</sup> study participants

To date, two individuals have completed the main part of the study. Their neurological status was evaluated according to the ISNCSCI<sup>50</sup> and is reported in Supplementary Table 1. At the time of study enrollment, the following characteristics of the participants were recorded: participant P1 was 29 years old and classified as having a motor and sensory incomplete (American Spinal Injury Association Impairment Scale (AIS) C) T1 lesion that had occurred 5 years earlier, and participant P2 was 51 years old and classified as having a motor and sensory incomplete (AIS D) C5 lesion that had occurred 16 years earlier.

### Anatomical MRI data

Anatomical brain data were acquired on a 3-T Prisma Fit MRI scanner equipped with a 64-channel head coil (Siemens Healthineers, VE11E software version). For each participant, anatomical data were acquired using an MPRAGE (Magnetization-Prepared Rapid Gradient Echo) 3D high-resolution isotropic T1-weighted sequence before and after the injection of gadolinium (Dotarem 0.5 mmol Gd per ml, Guerbet), a SPACE (Sampling Perfection with Application optimized Contrasts using different flip angle Evolution) 3D high-resolution isotropic T2-weighted sequence and a FLAWS (FLuid And White matter Suppression) based on an MP2RAGE (Magnetization-Prepared 2 Rapidly Acquired Gradient Echo) 3D sequence. The sequences were used to reconstruct the brain anatomy with the blood vessels.

### Diffusion tensor imaging

Magnetic resonance images were acquired on a 3-T whole-body MRI system (Magnetom Prisma, Siemens Medical Systems) using a 64-channel radiofrequency head coil and body coil for transmission.

To define and label the LH, we implemented a qMRI protocol including three multiecho 3D FLASH acquisitions with magnetization transfer-weighted ( $TR = 24.5$  ms,  $\alpha = 6^\circ$ ), proton density-weighted ( $TR = 24.5$  ms,  $\alpha = 6^\circ$ ) and T1-weighted ( $TR = 24.5$  ms,  $\alpha = 21^\circ$ ) contrasts at 1-mm isotropic resolution<sup>70,72</sup>. To correct for the effects of radiofrequency transmit field inhomogeneities<sup>73</sup>, we acquired B1 mapping data using the 3D EPI spin-echo and stimulated echo method, as previously described (4-mm<sup>3</sup> resolution,  $TE = 39.06$  ms,  $TR = 500$  ms)<sup>73,74</sup>. B0-field mapping data were acquired to correct image distortions in the EPI data (2D double-echo FLASH sequence with slice thickness = 2 mm,  $TR = 1,020$  ms,  $TE1/TE2 = 10/12.46$  ms,  $\alpha = 90^\circ$ , bandwidth = 260 Hz per pixel). The total acquisition time was 27 min.

All structural data were processed in the framework of Statistical Parametric Mapping SPM12 ([www.fil.ion.ucl.ac.uk/spm](http://www.fil.ion.ucl.ac.uk/spm); Wellcome Trust Centre for Neuroimaging, London) using custom MATLAB tools (The Mathworks). To label the LH in the individuals' native space, we used the framework of maximum probability tissue labels derived from the Medical Image Computing and Computer Assisted Intervention Society 2012 Grand Challenge and Workshop on Multi-atlas Labeling (<https://my.vanderbilt.edu/masi/about-us/resources-data/>) with cortical and subcortical labels and included the previously published definition of the LH<sup>75</sup>. The labels were spatially registered to the individuals' native space using SPM12's diffeomorphic 'geodesic shoot' registration<sup>76</sup>.

### Diffusion-based tractography

The diffusion-weighted imaging (DWI) protocol consisted of a 2D echo-planar sequence with the following parameters:  $TR = 7,400$  ms,  $TE = 69$  ms, parallel GRAPPA (GeneRALized Autocalibrating Partially Parallel Acquisition) acceleration factor = 2,  $FoV = 192 \times 212$  mm<sup>2</sup>, voxel size =  $2 \times 2 \times 2$  mm, matrix size =  $96 \times 106$ , 70 axial slices, 118 gradient directions (15 at  $b = 650$  s mm<sup>-2</sup>, 30 at  $b = 1,000$  s mm<sup>-2</sup>, 60 at  $b = 2,000$  s mm<sup>-2</sup> and 13 at  $b = 0$  interleaved throughout the acquisition). We also acquired B0-field maps (2D double-echo FLASH sequence with slice thickness = 2 mm,  $TR = 1,020$  ms,  $TE1/TE2 = 10/12.46$  ms,  $\alpha = 90^\circ$ , bandwidth = 260 Hz per pixel) to correct for geometric distortions in EPI data.

DWI data were preprocessed with MRtrix3 (ref. 77), including denoising<sup>78</sup> and Gibbs ringing artifacts removal<sup>78</sup>. We corrected for eddy current distortions and subject movements with the FSL 5.0 EDDY tool<sup>79</sup>. For EPI susceptibility distortion correction, we used the acquired B0 maps with the SPM FieldMap toolbox. The bias field was estimated from the mean  $b = 0$  images and corrected for in all DWI data. We then aligned the preprocessed diffusion maps to the magnetization transfer saturation images using SPM12 rigid body registration. For tractography, we defined the LH as the seed, as described above, and all cortical and subcortical gray matter structures as the target.

### DBS<sup>LH</sup> technology

DBS was delivered using the CE-marked Medtronic neurostimulation system for DBS therapy, including the Percept PC neurostimulator (model B35200) implanted below the clavicle, and two SenSight directional leads (model B3301542(M) for P1 and model B3300542(M) for P2) implanted in the LH. The neurostimulator was controlled by the clinical team using the Medtronic Clinician Programmer app (model A610) or by the participants using the Patient Programmer app (model A620). The whole system was used off-label for a different indication: to augment motor function in patients with SCI.

### Neurosurgical intervention

**Bilateral insertion of DBS leads in the LH.** Preoperative 3-T anatomical brain MRI, functional MRI and DTI sequences were merged onto StealthStation Surgical Navigation software (Medtronic). The left and right sides of the LH were identified on the anatomical MRI and double-checked with the standard stereotactic brain atlas. The precise surgical target was then selected by combining the data acquired from the functional MRI and DTI sequences. The stereotactic coordinates used for P1 were 5.7 mm (left) and 6.0 mm (right) lateral to the mid-commissural line, 10.8 mm anterior to the midcommissural point and 5.7 mm inferior to the midcommissural line. The stereotactic coordinates used for P2 were 6.7 mm (left) and 6.1 mm (right) lateral to the midcommissural line, 7.3 mm anterior to the midcommissural point and 7.2 mm inferior to the midcommissural line. On the morning of the surgery, the Cosman–Roberts–Wells stereotactic frame was placed on the patient's head under local anesthesia. A CT scan with contrast was performed to determine the location of the frame in relation to the patient's anatomy. The CT scan was geometrically aligned with the aforementioned sequences to obtain the stereotactic coordinates of the surgical target. Intraoperative imaging with the O-arm (Medtronic) and electrophysiological neuromonitoring were used to assess and verify the final location of the electrode based on the defined target. This first stage of the surgery was conducted while the patient was awake to monitor sensations and potential side effects. The second stage of the surgery consisted of implanting the Percept PC neurostimulator (Medtronic) in a subcutaneous pocket located in the infraclavicular area. The electrodes and extensions were tunneled under the skin to the neurostimulator location. This stage was performed under general anesthesia.

**Electrophysiological neuromonitoring.** Before the final Medtronic DBS lead insertion, a testing probe (micro–macro electrodes MiMa, Inomed Medizintechnik) with a microrecording electrode at the tip and a macrostimulating electrode ring was inserted through the cannula. The probe was connected to a neuromonitoring system (Neuro Omega (AlphaOmega Engineering) for P1 and Dantec KeyPoint Focus (Natus Medical) for P2). Neuronal spike amplitudes with the microelectrode were recorded from 10 mm above the target down to 2 mm below the target. Stimulation was performed at 2, 20, 50 and 170 Hz, with a 30- $\mu$ s pulse width and 0- to 7-mA amplitude, from 5 mm above the target down to the target location to assess for motor and sensory effects as well as potential side effects.

### 3D anatomical reconstruction and tissue volume activation

Lead-DBS v2.6 MATLAB toolbox<sup>80,81</sup> was used for postoperative electrode localization and simulation of the volume of tissue activated (VTA). The SPM12 (<https://www.fil.ion.ucl.ac.uk/spm/software/spm12/>)<sup>82</sup> and Advanced Normalization Tools<sup>83,84</sup> methods were applied to coregister the preoperative MRI (T1-weighted, T2-weighted and additional T2-weighted for P1 or FLAWS for P2; with 1-mm isovoxel resolution) and postoperative CT (with non-isovoxel resolution;  $0.43 \times 0.43 \times 1.25$  mm for P1 and  $0.43 \times 0.43 \times 1$  mm for P2) scans and to normalize to the standard Montreal Neurological Institute (MNI) 152 2009b NLIN ASYM space<sup>85</sup> with a brainshift correction<sup>86</sup>. The PaCER approach<sup>87</sup> was performed to localize the electrodes automatically. The

Atlas of the Human Hypothalamus<sup>75</sup> was used to define the subcortical segmentations visualized in the MNI space.

Lead Group<sup>88</sup> was used to simulate various configurations of VTAs following the SimBio/FieldTrip model<sup>89</sup>. As the latter pipeline does not support directional electrodes yet, electrode models were modified to Medtronic 3387 for P1 and Medtronic 3389 for P2, which are nondirectional electrodes equivalent to Medtronic B33015 and Medtronic B33005, respectively. The overlap between the VTA and each structure included in the Atlas of the Human Hypothalamus<sup>75</sup> and the DBS Tractography Atlas<sup>90</sup> was calculated for various configurations to obtain the selectivity of the stimulation of the LH.

### DBS<sup>LH</sup> calibration sessions

During the 1-week calibration period, the predicted electrode configurations, as well as other configurations, were tested. Sensory perception, general sensations and muscle activity were reported for each configuration tested in the supine position to define the configurations with the fewest side effects. The stimulation parameters (frequency and amplitude) were then optimized when walking in parallel bars and during voluntary leg movements to achieve optimal stimulation that elicited greater muscle activity and amplitude of movement. The pulse width was set at 60  $\mu$ s and was not calibrated. As no locomotor effects were observed with regard to the stimulation frequency, this was defined on the basis of the participant's perception.

### Clinical evaluations

**International Standards for Neurological Classification of SCI.** Each participant's neurological status was assessed based on the ISNCSCI, a comprehensive clinician-administered neurological examination of residual sensory and motor function quantifying SCI severity<sup>50</sup>. The examiner was blinded to the DBS condition. This test was performed at the start (M0) and end (M3) of the 3 months of rehabilitation.

**Six-minute walk test.** Endurance was assessed by the distance covered overground within 6 min with a standard four-wheel walker, as well as full-leg orthoses for P1. The test was performed in the DBS<sup>ON</sup> and DBS<sup>OFF</sup> conditions assessed within the same week. This test was performed at the start of the rehabilitation period (M0) and the end of the main study phase (M6)<sup>91</sup>.

**Ten-meter walk test.** Walking speed was assessed by a timed 10-m walk test with a standard four-wheel walker, as well as full-leg orthoses for P1. This test was repeated two times while walking at a fast speed. The test was performed in the DBS<sup>ON</sup> and DBS<sup>OFF</sup> conditions assessed within the same week. This test was performed at the start of the rehabilitation (M0) and the end of the main study phase (M6)<sup>91</sup>.

### Rehabilitation program

Participants followed a rehabilitation program three times per week for 3 months. The rehabilitation program was personalized to the participants' performance and goals. This period of rehabilitation comprised walking overground with multiple assistive devices, sit-to-stand, standing, and leg and trunk muscle exercises. When necessary, a tailored amount of body weight support was provided to P1 using an overhead support system based on the cable robot technology (Rysen, Motek Medical). This robotic system allows the application of tailored forces to the trunk through a dedicated harness along the vertical and anteroposterior directions.

P1 trained to walk without the need for her full-leg orthoses and weight support, and P2 trained to walk longer distances and to be able to climb and descend stairs independently in his house. DBS<sup>LH</sup> was delivered to enable the participants to practice these activities.

### Recording of kinematic and muscle activity

Participants were asked to walk with the aid of a parallel bar and body weight support (Rysen, Motek Medical) when necessary while recording

muscle activity and kinematics. These recordings were performed in the DBS<sup>ON</sup> and DBS<sup>OFF</sup> conditions assessed within the same week.

EMG activity was recorded bilaterally from the iliopsoas, rectus femoris, vastus lateralis, semitendinosus, tibialis anterior, medial gastrocnemius and soleus muscles. Each electrode was placed centrally over the muscle with a longitudinal alignment. An abrasive paste (Nuprep, Weaver and Company) was used for skin preparation to reduce electrode-skin resistance and improve EMG signal quality. Muscle activity was acquired at a 2-kHz sample rate using the 16-channel wireless Delsys system.

Kinematic recordings were obtained at a 100-Hz sampling rate using a 3D motion capture system (Vicon Motion Systems and Nexus v1.8.5 software) consisting of 14 infrared cameras that covered a 12  $\times$  4  $\times$  2.5-m workspace. Body kinematics were captured by these infrared cameras through the use of infrared-reflective markers positioned over standardized anatomical landmarks (hip, knee, ankle and toe).

Reconstructed kinematic data and EMG activity data were processed with custom MATLAB scripts, and a principal component analysis was performed. The analysis is further described in 'Principal component analysis' in Methods.

### Chronophotography

Chronophotography was used to generate a representative series of still pictures arranged in a single photograph to illustrate the locomotor abilities of animals and human participants. Videos at 25 fps or photographs at 15 fps were recorded during locomotor tasks. Images from these recordings were chosen to illustrate the different consecutive phases of walking of the limbs (that is, stance phases and swing phases). The frequency of chosen pictures varied due to the varying velocity. The series of pictures were assembled in Adobe Photoshop while blending out nonessential details.

### Reporting summary

Further information on research design is available in the Nature Portfolio Reporting Summary linked to this article.

### Data availability

Data underpinning this publication have been deposited in Zenodo at <https://doi.org/10.5281/zenodo.10628681> (ref. 92) and are publicly available under a Creative Commons Attribution 4.0 International license.

### References

- Squair, J. W. et al. Neuroprosthetic baroreflex controls haemodynamics after spinal cord injury. *Nature* **590**, 308–314 (2021).
- Kathe, C. et al. Wireless closed-loop optogenetics across the entire dorsoventral spinal cord in mice. *Nat. Biotechnol.* **40**, 198–208 (2022).
- Takeoka, A., Vollenweider, I., Courtine, G. & Arber, S. Muscle spindle feedback directs locomotor recovery and circuit reorganization after spinal cord injury. *Cell* **159**, 1626–1639 (2014).
- Caggiano, V. et al. Midbrain circuits that set locomotor speed and gait selection. *Nature* **553**, 455–460 (2018).
- Anderson, M. A. et al. Required growth facilitators propel axon regeneration across complete spinal cord injury. *Nature* **561**, 396–400 (2018).
- Lee, E. et al. ACT-PRESTO: rapid and consistent tissue clearing and labeling method for 3-dimensional (3D) imaging. *Sci. Rep.* **6**, 18631 (2016).
- Capelli, P., Pivetta, C., Esposito, M. S. & Arber, S. Locomotor speed control circuits in the caudal brainstem. *Nature* **551**, 373–377 (2017).
- Wenger, N. et al. Spatiotemporal neuromodulation therapies engaging muscle synergies improve motor control after spinal cord injury. *Nat. Med.* **22**, 138–145 (2016).
- Anderson, M. A. et al. Astrocyte scar formation aids central nervous system axon regeneration. *Nature* **532**, 195–200 (2016).
- Bankhead, P. et al. QuPath: open source software for digital pathology image analysis. *Sci. Rep.* **7**, 16878 (2017).

66. Bria, A. & Iannello, G. TeraStitcher—a tool for fast automatic 3D-stitching of teravoxel-sized microscopy images. *BMC Bioinformatics* **13**, 316 (2012).
67. Sotocinal, S. G. et al. The Rat Grimace Scale: a partially automated method for quantifying pain in the laboratory rat via facial expressions. *Mol. Pain* **7**, 55 (2011).
68. Elgendi, M., Norton, I., Brearley, M., Abbott, D. & Schuurmans, D. Systolic peak detection in acceleration photoplethysmograms measured from emergency responders in tropical conditions. *PLoS ONE* **8**, e76585 (2013).
69. Lutti, A., Thomas, D. L., Hutton, C. & Weiskopf, N. High-resolution functional MRI at 3T: 3D/2D echo-planar imaging with optimized physiological noise correction. *Magn. Reson. Med.* **69**, 1657–1664 (2013).
70. Weiskopf, N. et al. Quantitative multi-parameter mapping of R1, PD\*, MT, and R2\* at 3T: a multi-center validation. *Front. Neurosci.* **7**, 95 (2013).
71. Hutton, C. et al. Image distortion correction in fMRI: a quantitative evaluation. *NeuroImage* **16**, 217–240 (2002).
72. Draganski, B. et al. Regional specificity of MRI contrast parameter changes in normal ageing revealed by voxel-based quantification (VBQ). *NeuroImage* **55**, 1423–1434 (2011).
73. Lutti, A., Dick, F., Sereno, M. I. & Weiskopf, N. Using high-resolution quantitative mapping of R1 as an index of cortical myelination. *NeuroImage* **93**, 176–188 (2014).
74. Lutti, A. et al. Robust and fast whole brain mapping of the RF transmit field B1 at 7T. *PLoS ONE* **7**, e32379 (2012).
75. Neudorfer, C. et al. A high-resolution in vivo magnetic resonance imaging atlas of the human hypothalamic region. *Sci. Data* **7**, 305 (2020).
76. Ashburner, J. & Friston, K. J. Diffeomorphic registration using geodesic shooting and Gauss–Newton optimisation. *NeuroImage* **55**, 954–967 (2011).
77. Tournier, J.-D. et al. MRtrix3: a fast, flexible and open software framework for medical image processing and visualisation. *NeuroImage* **202**, 116137 (2019).
78. Veraart, J. et al. Denoising of diffusion MRI using random matrix theory. *NeuroImage* **142**, 394–406 (2016).
79. Andersson, J. L. R. & Sotiropoulos, S. N. An integrated approach to correction for off-resonance effects and subject movement in diffusion MR imaging. *NeuroImage* **125**, 1063–1078 (2016).
80. Horn, A. & Kühn, A. A. Lead-DBS: a toolbox for deep brain stimulation electrode localizations and visualizations. *NeuroImage* **107**, 127–135 (2015).
81. Horn, A. et al. Lead-DBS v2: towards a comprehensive pipeline for deep brain stimulation imaging. *NeuroImage* **184**, 293–316 (2019).
82. Friston, K. J. et al. Statistical parametric maps in functional imaging: a general linear approach. *Hum. Brain Mapp.* **2**, 189–210 (1994).
83. Avants, B. B. et al. A reproducible evaluation of ANTs similarity metric performance in brain image registration. *NeuroImage* **54**, 2033–2044 (2011).
84. Avants, B. B., Epstein, C. L., Grossman, M. & Gee, J. C. Symmetric diffeomorphic image registration with cross-correlation: evaluating automated labeling of elderly and neurodegenerative brain. *Med. Image Anal.* **12**, 26–41 (2008).
85. Fonov, V. et al. Unbiased average age-appropriate atlases for pediatric studies. *NeuroImage* **54**, 313–327 (2011).
86. Schönecker, T., Kupsch, A., Kühn, A. A., Schneider, G.-H. & Hoffmann, K.-T. Automated optimization of subcortical cerebral MR imaging–atlas coregistration for improved postoperative electrode localization in deep brain stimulation. *AJNR Am. J. Neuroradiol.* **30**, 1914–1921 (2009).
87. Husch, A., Petersen, M. V., Gemmar, P., Goncalves, J. & Hertel, F. PaCER—a fully automated method for electrode trajectory and contact reconstruction in deep brain stimulation. *NeuroImage Clin.* **17**, 80–89 (2018).
88. Treu, S. et al. Deep brain stimulation: imaging on a group level. *NeuroImage* **219**, 117018 (2020).
89. Horn, A. et al. Connectivity predicts deep brain stimulation outcome in Parkinson disease. *Ann. Neurol.* **82**, 67–78 (2017).
90. Middlebrooks, E. H. et al. Neuroimaging advances in deep brain stimulation: review of indications, anatomy, and brain connectomics. *AJNR Am. J. Neuroradiol.* **41**, 1558–1568 (2020).
91. Jackson, A. B. et al. Outcome measures for gait and ambulation in the spinal cord injury population. *J. Spinal Cord Med.* **31**, 487–499 (2008).
92. Courtine, G., Barraud, Q. & Squair, J. Datasets related to the manuscript ‘Hypothalamic deep brain stimulation augments walking after spinal cord injury’. *Zenodo* <https://doi.org/10.5281/zenodo.10628681> (2024).

## Acknowledgements

This study was supported by ONWARD Medical, the Swiss National Science Foundation (Ambizione fellowship to J.W.S., PZ00P3\_208988) and subsidy to G.C. (310030\_185214 and 310030\_215668), Canadian Institutes of Health Research (Research Fellowship Award to N.C.), European Research Council (ERC-2015-CoG HOW2WALKAGAIN 682999; Marie Skłodowska-Curie individual fellowship 842578 to J.W.S.), H2020-MSCA-COFUND-2016 EPFL Fellows program (no. 665667 to C.K.), Human Frontiers in Science Program long-term fellowship (LTO01278/2017-L to C.K.) and the Swiss National Supercomputing Center (CSCS). We are grateful to B. Schneider and S. Arber for providing viral vectors, as well as to the Advanced Lightsheet Imaging Center (ALICe) at the Wyss Center for Bio and Neuroengineering, Geneva.

## Author contributions

V.A., N.D.J. and L.B.-F. contributed equally to this work. N.C., N.D.J., L. Baud, T.H.H. and C.K. performed the animal experiments. J.W.S. and M.A.S. performed computational analysis. N.C., N.D.J., K.G. and Q.B. performed the anatomical experiments. N.C., Q.B. and K.G. performed clearing protocols. M. Goubran developed and shared MIRACL. N.C., J.W.S., Q.B., I.D., A. Leonhartsberger, K.S., M. Gautier, K.G., L. Batti, S.P., K.A.B., A. Laskaratos and M.H. performed image acquisition, processing and analysis. J.R. and F.M. prepared illustrations. N.C., J.W.S., V.A., I.D., A. Leonhartsberger, K.S. and M.A.A. analyzed the experimental data. L.B.-F., V.A., N.H., N.I., C.V., S.C., R.D., L.A. and J.B. performed human experiments. N.I. and L.B.-F. conducted rehabilitation sessions. L.B.-F., N.H., C.V., N.B., L.A. and R.D. analyzed the human data. L.B.-F., L.A., A.W. and L.D. managed regulatory affairs. J.B. and V.A. performed neurosurgical interventions. B.D. performed the fMRI experiments and analyzed the data. G.C. and J.B. conceived and supervised the study. G.C. and J.B. secured funding. G.C. wrote the paper with J.B., N.C., J.W.S., Q.B. and L.A., and all authors contributed to its editing.

## Competing interests

G.C., J.B., N.C., J.W.S., R.D., L.A. and L.B.-F. hold various patents in relation to the present work. G.C. is a consultant of ONWARD Medical. G.C. and J.B. are minority shareholders of ONWARD Medical, a company with partial relationships with the presented work. The other authors declare no competing interests.

## Additional information

**Extended data** is available for this paper at <https://doi.org/10.1038/s41591-024-03306-x>.

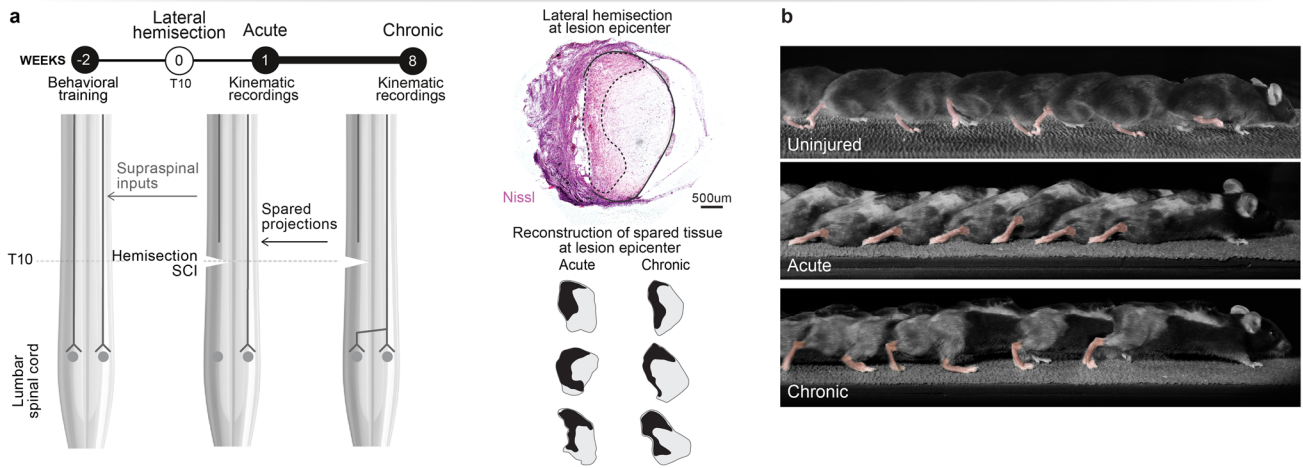
**Supplementary information** The online version contains supplementary material available at <https://doi.org/10.1038/s41591-024-03306-x>.

**Correspondence and requests for materials** should be addressed to Jocelyne Bloch or Grégoire Courtine.

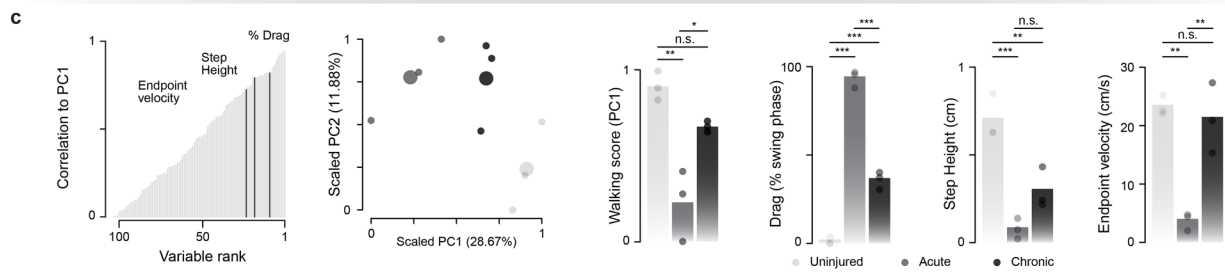
**Peer review information** *Nature Medicine* thanks the anonymous reviewers for their contribution to the peer review of this work. Primary Handling Editor: Jerome Staal, in collaboration with the *Nature Medicine* team.

**Reprints and permissions information** is available at [www.nature.com/reprints](http://www.nature.com/reprints).

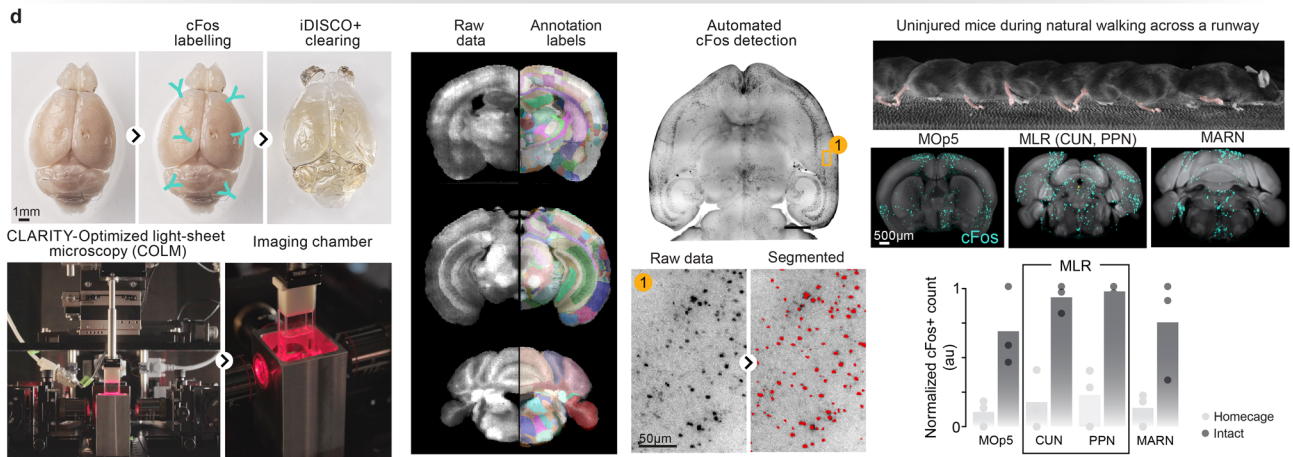
Anatomical and functional characterization of a mouse model of lateral hemisection SCI



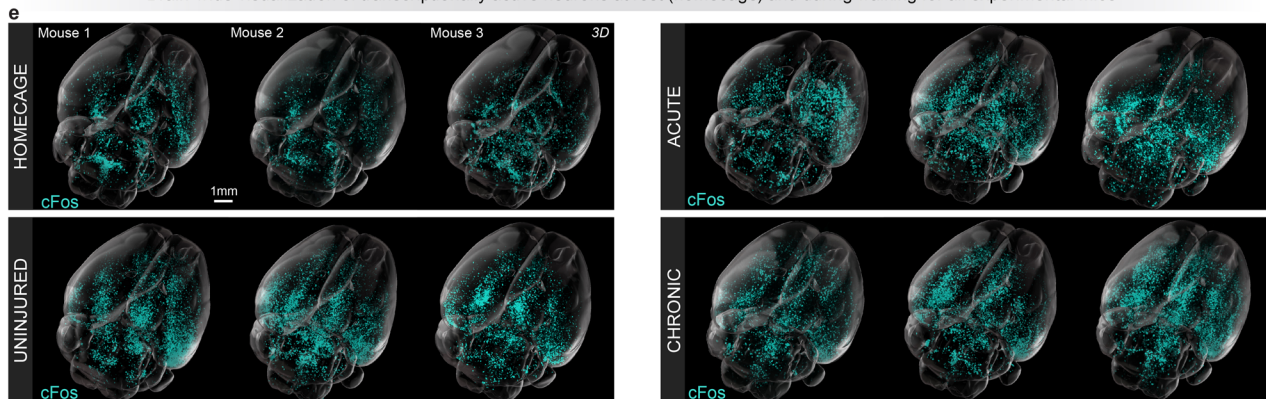
Spontaneous recovery of walking after lateral hemisection SCI



Optimization of iDISCO+ procedures for labelling of transcriptionally active neurons across the entire brain



Brain-wide visualization of transcriptionally active neurons at rest (homeage) and during walking for all experimental mice

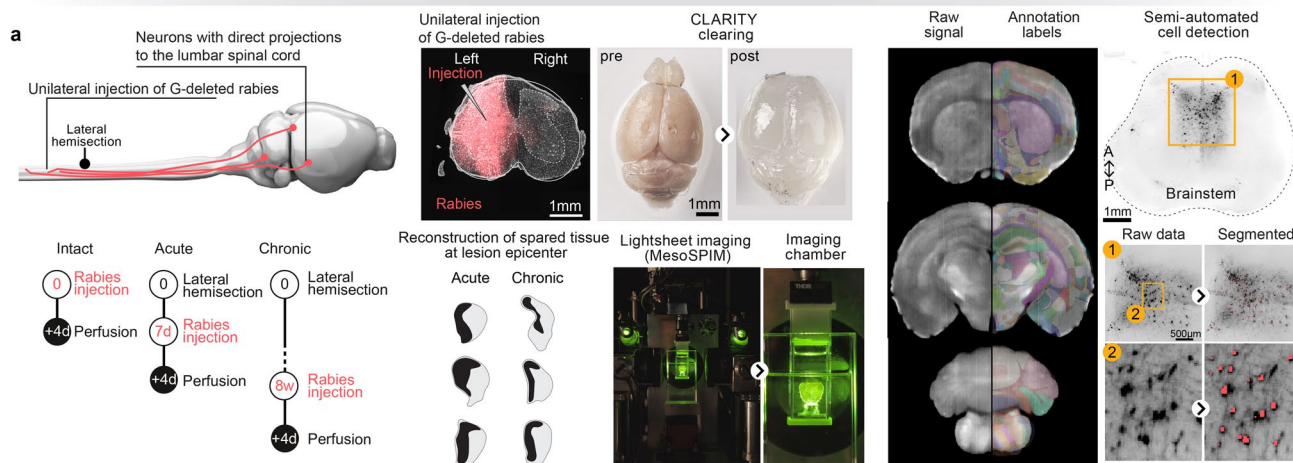


Extended Data Fig. 1 | See next page for caption.

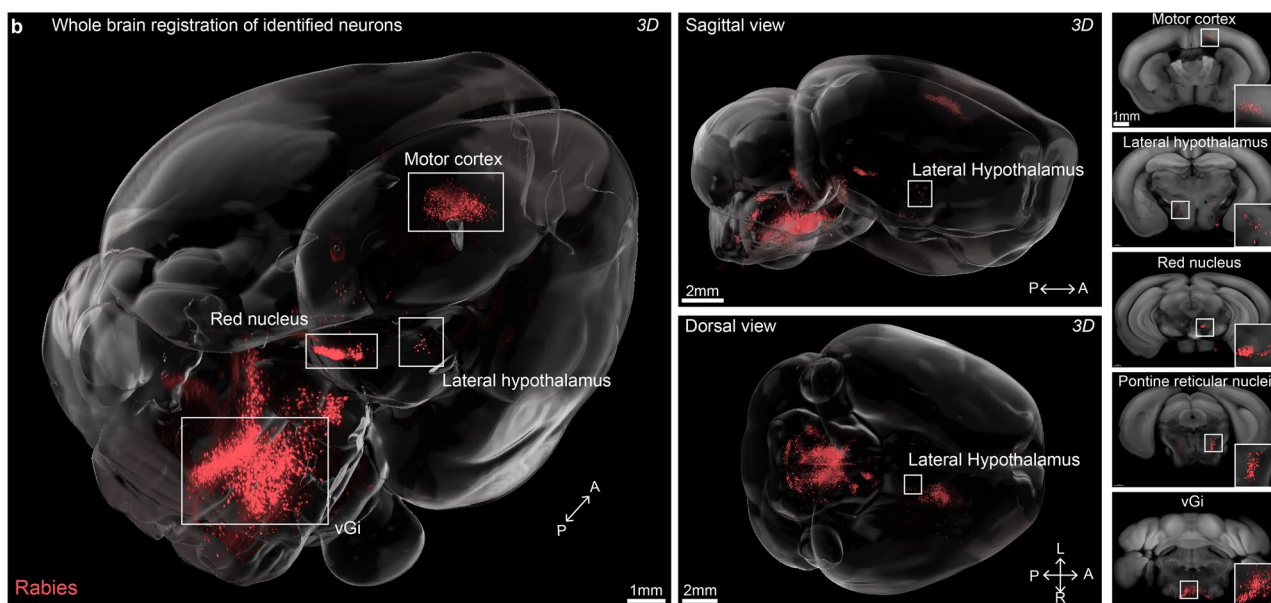
**Extended Data Fig. 1 | Characterization of whole brain activity after recovery after incomplete SCI.** **a**, Overview of experimental approach for lateral hemisection SCI in mice. Mice were trained to run continuously on a treadmill for 2 weeks prior to injury. Uninjured mice and mice after 1 week (acute) and 8 weeks (chronic) after injury then ran on the treadmill to assess recovery of function. **b**, Chronophotography of walking captured in uninjured mice and at 1 week (acute) and 8 weeks (chronic) after a lateral hemisection SCI. Ipsilesional (left) leg visualized (mirrored image presented). **c**, Walking was quantified using principal component analysis applied to gait parameters calculated from kinematic recordings. In this denoised space, each dot represents a mouse ( $n \geq 10$  gait cycles per mouse,  $n = 3$  mice per group). Larger dots represent the mean of each experimental group. The first principal component (PC1) distinguished gaits of mice without SCI from mice with SCI. Walking scores were thus quantified as the scores on PC1. Analysis of factor loadings on PC1 revealed that the percentage of paw dragging, step height, and endpoint velocity were the parameters that showed high correlation with PC1. Bars report the mean values of these gait parameters. Statistics are provided in Supplementary Data 1. **d**, To examine whole brain activity, mice ( $n = 3$  mice per group) ran on a treadmill for 45 minutes

after which they were perfused 1 hour after the task to allow expression of cFos. iDISCO+ was utilized due to its reliable whole brain immunolabeling methodology<sup>14</sup>. To visualize cFos (nuclear) staining, a custom-built COLM (CLARITY-optimized lightsheet microscope)<sup>10</sup> was used at 4x magnification to ensure adequate resolution of nuclei. Whole mouse brain registration to the Allen Brain Atlas was performed using MIRACL<sup>19,20</sup>. Raw autofluorescence channel optical sections with demonstration of registration of the Allen Mouse Brain Atlas. Representative visualization of raw data demonstrating labeled cFos-positive cells. This was followed by automated segmentation via the Arivis Vision 4D “Blob Finder” function. Bar plot demonstrating cFos expression in intact mice in areas known to be involved in locomotion with representative optical sections through those regions demonstrating cFos labeling. Representative chronophotography of uninjured mouse walking across the runway shown (mirrored image). MOp5: primary motor area, layer 5; MLR: mesencephalic locomotor region; CUN: cuneiform nucleus; PPN: pedunclopontine nucleus; MARN: magnocellular reticular nucleus. **e**, 3D representations of all brains used in the analysis of cFos activity. Mice left in the homecage without any treadmill locomotion are also provided for reference.

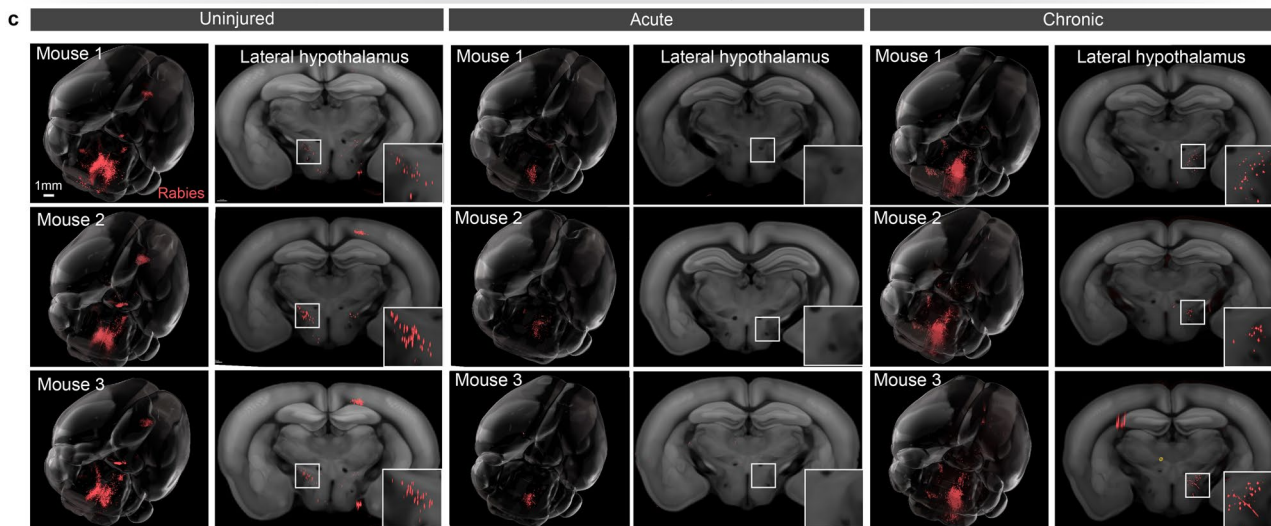
Experimental strategy for whole-brain labelling and registration of neurons with projections to the lumbar spinal cord ipsilateral to the lateral hemisection SCI



Whole brain registration of neurons with direct projections to the lumbar spinal cord ipsilateral to the side of lateral hemisection SCI



Brain-wide visualization of neurons with direct projections to the lumbar spinal cord ipsilateral to the lateral hemisection SCI

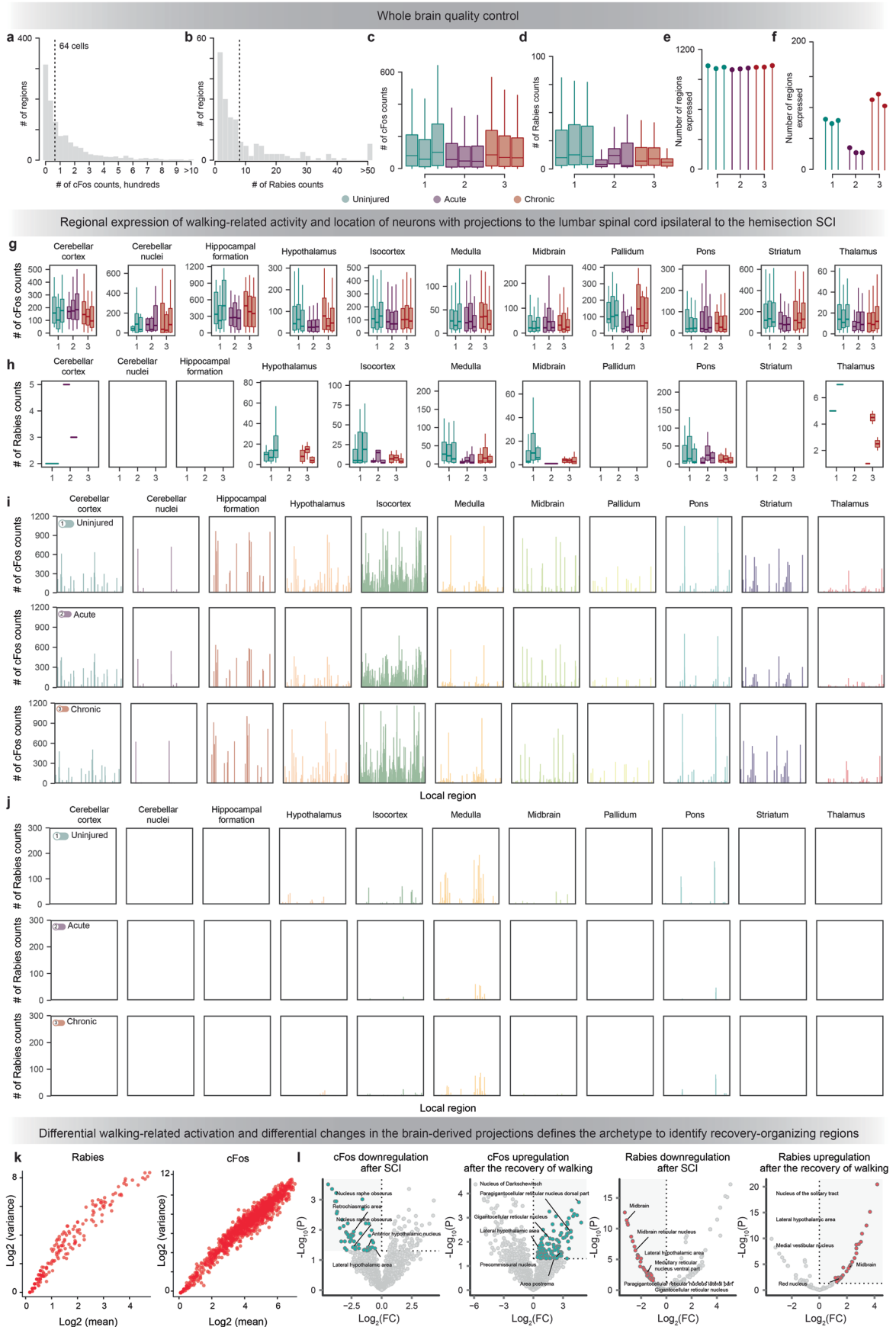


Extended Data Fig. 2 | See next page for caption.



**Extended Data Fig. 2 | Characterization of spinal cord-projecting neurons across the whole brain during recovery from SCI.** **a**, Uninjured mice, and mice 1 (acute) and 8 weeks (chronic) ( $n = 3$  mice per group) after left lateral hemisection at T10 were examined. G-deleted rabies was injected into the left (ipsilesional) lumbar spinal cord. Representative injection site of the left lumbar spinal cord demonstrating laterality of the injection. Demonstration of the whole brain clearing and imaging pipeline for mice injected with rabies. CLARITY was utilized due to its ability to preserve endogenous fluorescence, followed by imaging with a custom-built mesoSPIM lightsheet microscope<sup>22</sup>. Whole mouse brain registration was performed using MIRACL<sup>19,20</sup>. Optical sections

demonstrating registration of the mouse Allen Brain Atlas on raw CLARITY data of a mouse brain. Representative visualization of labeled neurons with subsequent semi-automated segmentation of neurons using the Arivis Vision 4D three-dimensional analysis software. **b**, 3D visualization of whole brain labeling of all neurons with direct connections to the lumbar spinal cord. Representative whole brain of uninjured animal with optical sections highlighting labeling in key regions of the brain. **c**, 3D representations of all brains used in the analysis of whole brain connectivity with time after SCI including uninjured mice and mice 1 week and 8 weeks after injury. The lateral hypothalamus is highlighted with optical sections.

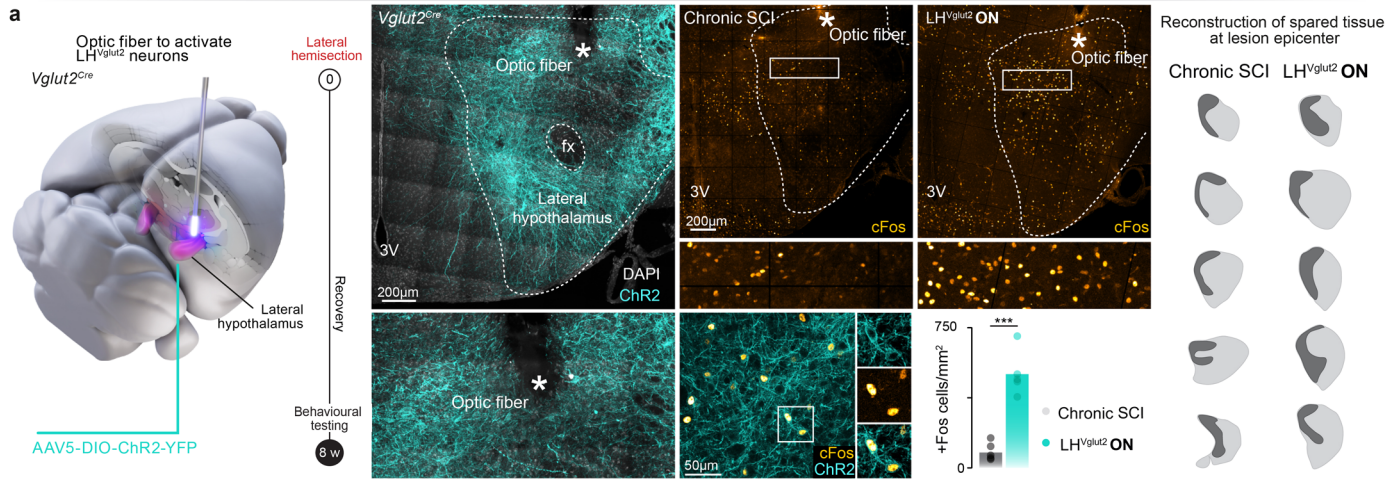


**Extended Data Fig. 3 | See next page for caption.**

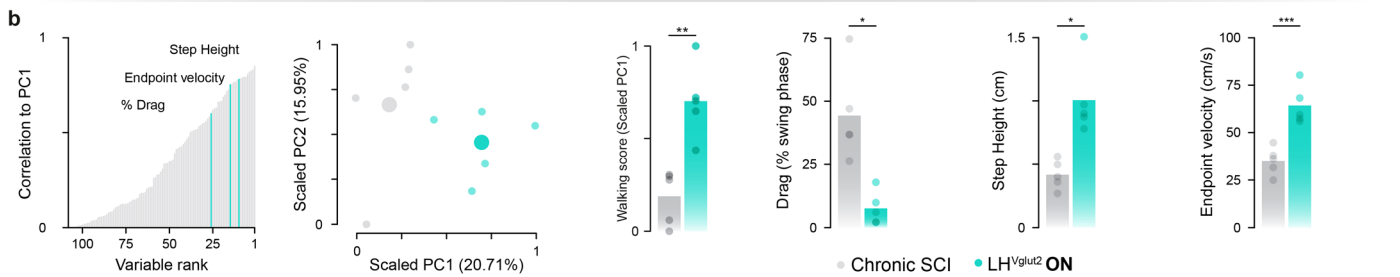
**Extended Data Fig. 3 | Quality control and differential analysis of whole brain transcriptional activity and anatomical connectivity.** **a**, Number of counts per region throughout the brain with transcriptional activity. Dashed line represents the median number of counts in each region. **b**, As in **a**, for spinal cord-projecting neuron counts. **c**, Number of transcriptionally active cells across the whole brain for each brain. Brains are colored by experimental group. Distribution reflects the variance across regions within each brain ( $n = 3$  mice per group). Box plots reflect the median, with the limits of the box as the first and third quartile, and the range represented by the plot whiskers. **d**, As in **c**, for spinal cord-projecting neuron counts ( $n = 3$  mice per group). Box plots reflect the median, with the limits of the box as the first and third quartile, and the range represented by the plot whiskers. **e**, Number of regions with transcriptionally active cells throughout the whole brain, for each brain. Brains are colored by experimental group. **f**, As in **e**, for spinal cord-projecting neuron counts. **g**, Number of transcriptionally

active cells in each major region of the brain, for each brain. Brains are colored by experimental group ( $n = 3$  mice per group). Box plots reflect the median, with the limits of the box as the first and third quartile, and the range represented by the plot whiskers. **h**, As in **g**, for spinal cord-projecting neuron counts ( $n = 3$  mice per group). Box plots reflect the median, with the limits of the box as the first and third quartile, and the range represented by the plot whiskers. **i**, Spike plot indicating the number of transcriptionally active cells in each region of the brain (x-axis). Plots are faceted by major region of the brain (horizontal) and experimental group (vertical). Each spike represents the counts for a single region. **j**, As in **i**, for spinal cord-projecting neuron counts. **k**, Mean-variance relationship for count data from transcriptionally active cells and spinal cord-projecting neurons. **l**, Volcano plots indicate differential analysis of each comparison outlined in **k**. Colored dots represent those meeting statistical significance. FC: Fold Change.

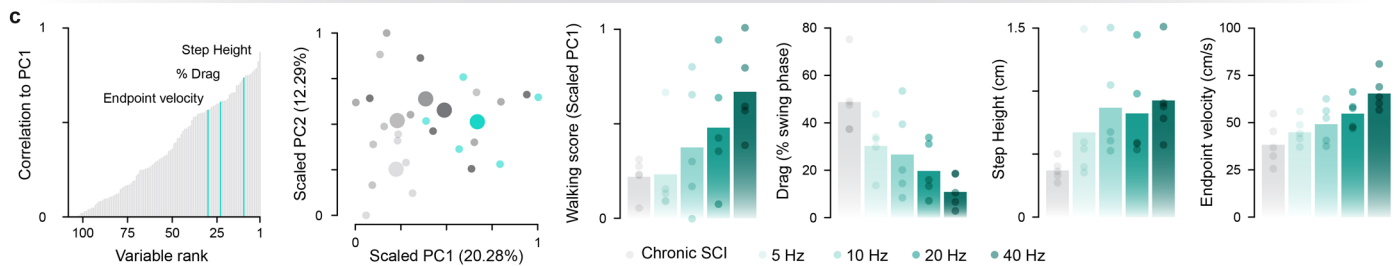
Optogenetic activation of glutamatergic neurons located in the lateral hypothalamus



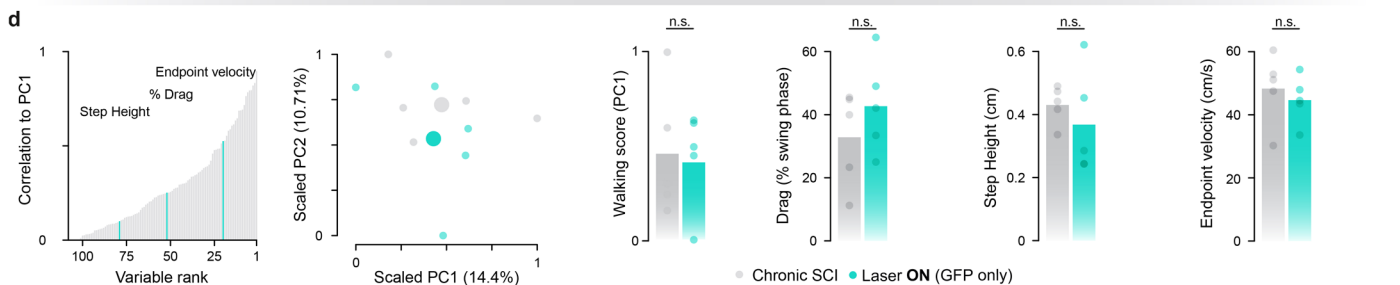
Optogenetic activation of glutamatergic neurons located in the lateral hypothalamus improves walking after lateral hemisection SCI



Augmentation of walking scales up with the frequency of optogenetic stimulation



Optogenetic stimulation following the expression of GFP in glutamatergic neurons of the lateral hypothalamus has no effect on walking after lateral hemisection SCI

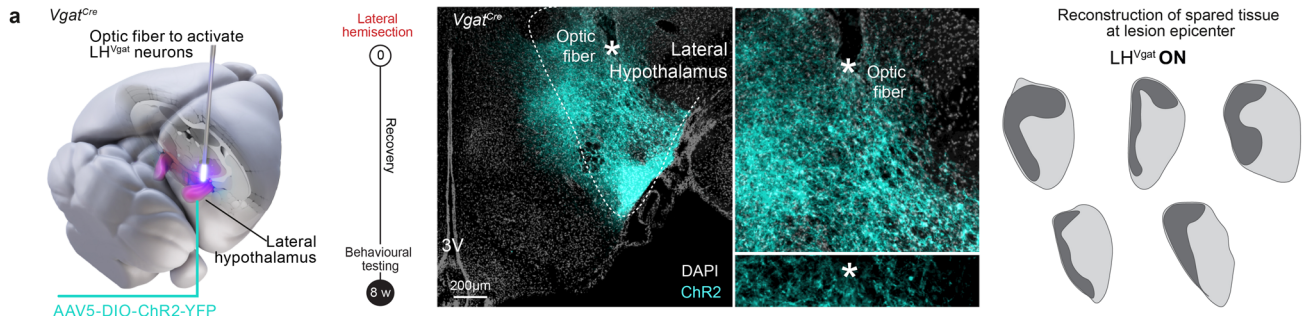


**Extended Data Fig. 4 | Optogenetic stimulation of LH<sup>Vglut2</sup> neurons**

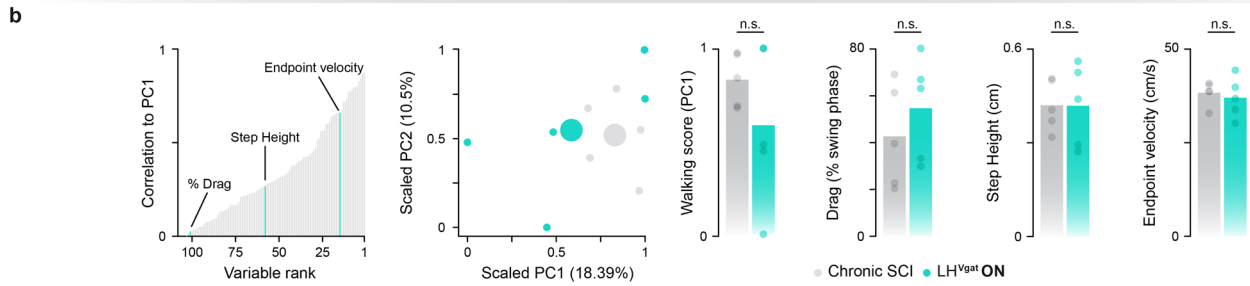
**significantly augments walking after chronic SCI.** **a**, Schematic of the experimental scheme demonstrating injection of an AAV5-DIO-ChR2-YFP into the right-sided LH of *Vglut2<sup>Cre</sup>* mice with insertion of an optic fiber. Mice underwent a left lateral hemisection at T10, and behavioral recordings were performed at 8 weeks post-SCI. Representative photomicrograph demonstrating Chr2 expression in LH<sup>Vglut2</sup> neurons following injections of AAV5-DIO-ChR2-YFP. The tract of the optic fiber is also visible in the LH, magnified in the inset. 3 V: third ventricle. Photomicrographs demonstrating cFos activation in the LH in response to 10 minutes of blue light stimulation in a *Vglut2<sup>Cre</sup>* animal injected with AAV5-DIO-ChR2-YFP compared to a *Vglut2<sup>Cre</sup>* mice injected with control virus. Quantification of cFos-positive cells revealed significantly more cFos<sup>ON</sup> cells in

mice injected with AAV5-DIO-ChR2-YFP compared to control virus ( $n = 5$  mice per group; independent samples two-tailed t-test;  $t = 7.068$ ;  $p = 0.0001$ ). Lesion reconstructions of animals included in kinematic analysis are provided. **b**, Kinematic analysis of mice following optogenetic activation of LH<sup>Vglut2</sup> neurons. Walking was quantified using principal component analysis as described in Fig. 1c and Extended Data Fig. 1c ( $n \geq 10$  gait cycles per mouse,  $n = 5$  mice per group). Statistics are provided in Supplementary Data 1. **c**, As in **b**, for mice following different frequencies of optogenetic stimulation ( $n \geq 10$  gait cycles per mouse,  $n = 5$  mice per group). **d**, As in **b**, for mice following photostimulation and injections of AAVs expressing only the reporter protein GFP, with no opsin expression ( $n \geq 10$  gait cycles per mouse,  $n = 5$  mice per group). Statistics are provided in Supplementary Data 1.

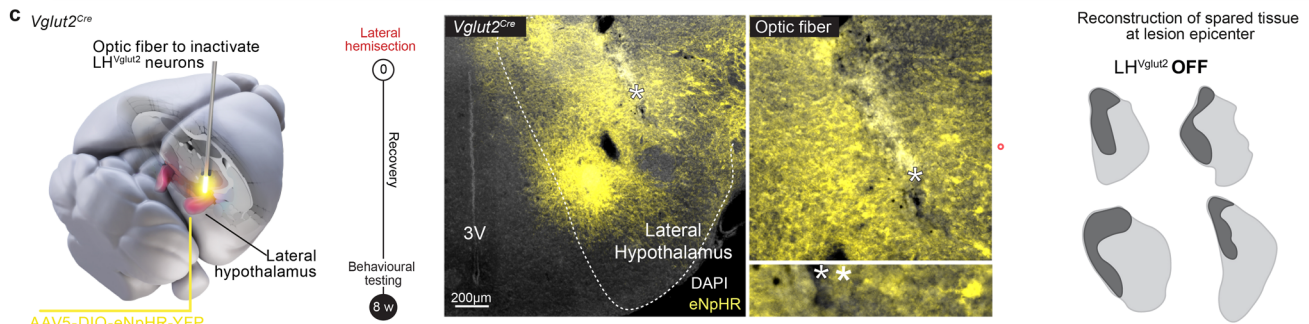
Optogenetic activation of GABAergic neurons located in the lateral hypothalamus



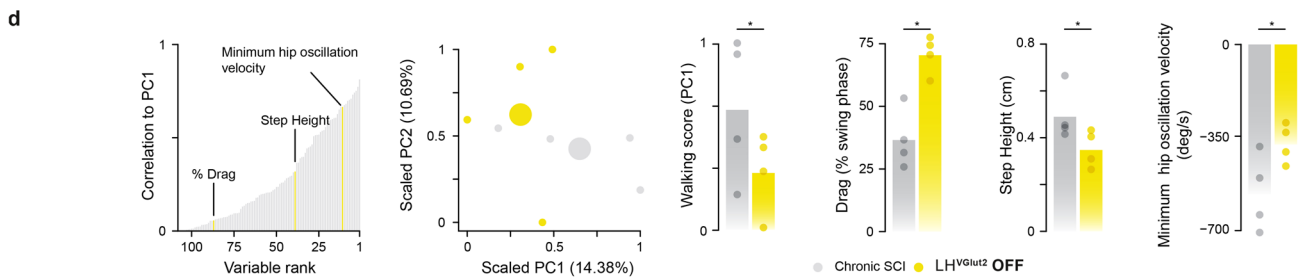
Optogenetic activation of GABAergic neurons in the lateral hypothalamus does not improve walking after lateral hemisection SCI



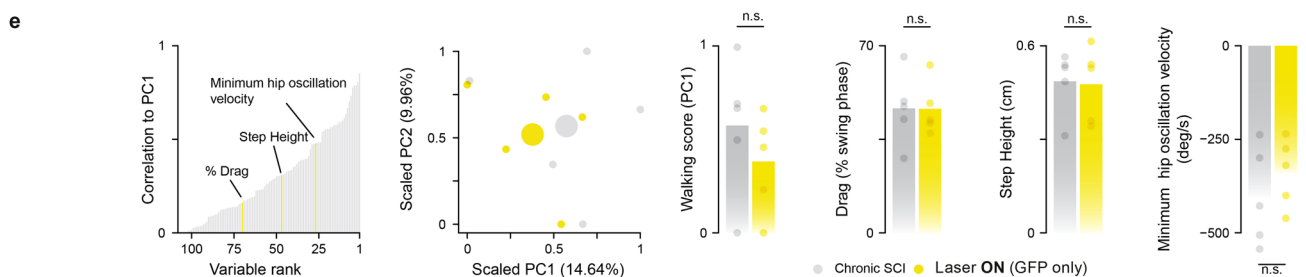
Optogenetic inhibition of glutamatergic neurons in the lateral hypothalamus



Optogenetic inhibition of glutamatergic neurons in the lateral hypothalamus impairs walking after lateral hemisection SCI



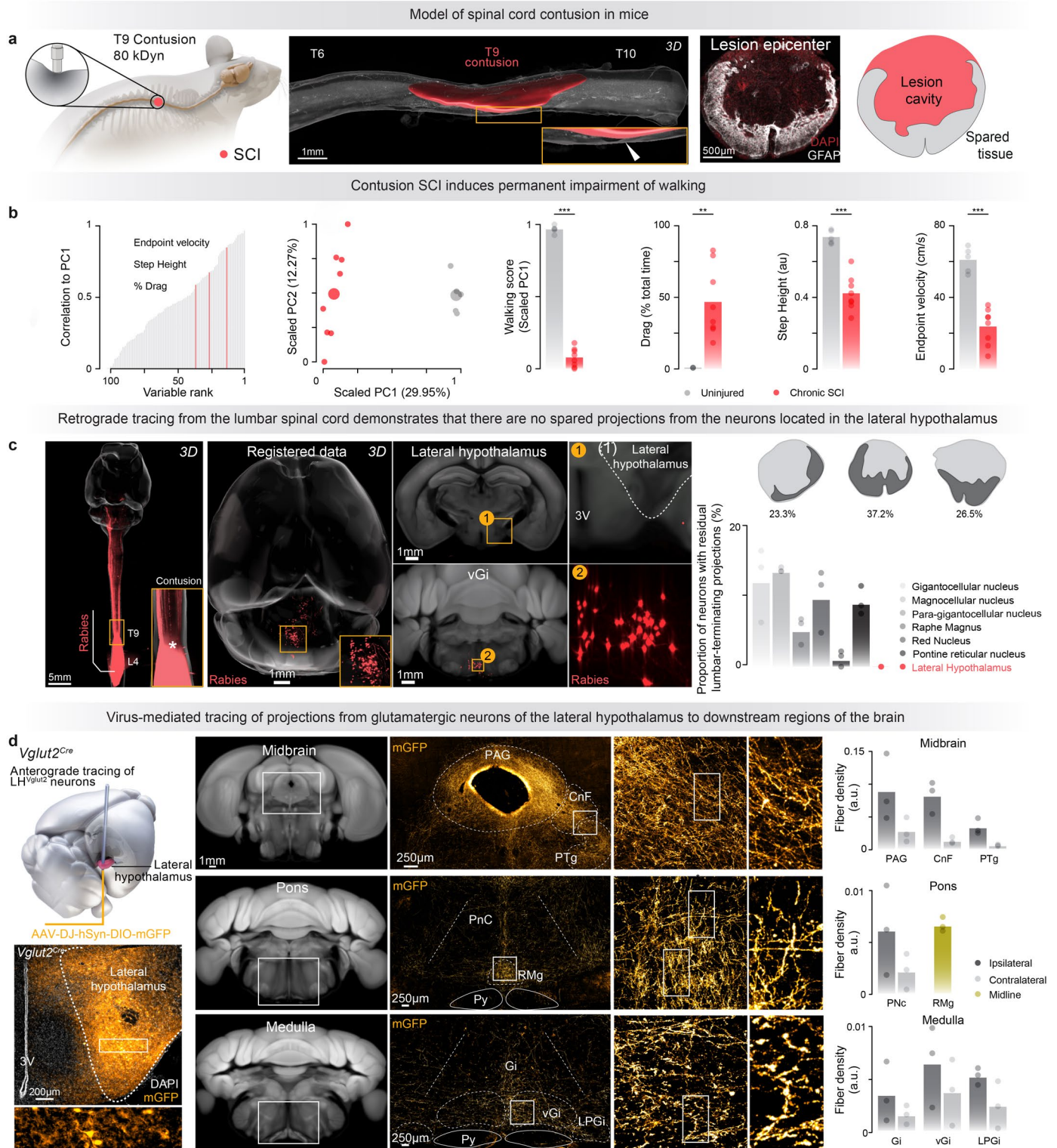
Optogenetic inhibition of the lateral hypothalamus in the presence of control virus does not reduce walking performance after lateral hemisection SCI



Extended Data Fig. 5 | See next page for caption.

**Extended Data Fig. 5 | Optogenetic stimulation of LH<sup>Vgat</sup> neurons does not alter walking while optogenetic inhibition of LH<sup>Vglut2</sup> degrades walking after chronic SCI.** **a**, Schematic of the experimental scheme demonstrating injections of AAV5-DIO-ChR2-YFP into the right-sided LH of Vgat<sup>Cre</sup> mice with insertion of an optic fiber. Mice underwent a left lateral hemisection at T10, and behavioral recordings were performed at 8 weeks post-SCI. Representative photomicrograph demonstrating ChR2 expression in LH<sup>Vgat</sup> neurons. The tract of the optic fiber is also visible in the LH, magnified in the inset. Spared tissue reconstructions for mice included in kinematic analyses are provided on the right. **b**, Kinematic analysis of mice following optogenetic activation of LH<sup>Vgat</sup> neurons. Walking was quantified using principal component analysis as described in Fig. 1c and Extended Data Fig. 1c ( $n \geq 10$  gait cycles per mouse,  $n = 5$

mice per group). Statistics are provided in Supplementary Data 1. **c**, Schematic of the experimental scheme demonstrating injection of an AAV5-DIO-eNpHR-YFP into the right-sided LH of Vglut2<sup>Cre</sup> mice with insertion of an optic fiber. Remaining experimental procedures mirror those outlined in **a**. Spared tissue reconstructions for mice included in kinematic analyses are provided on the right. **d**, As in **b**, for mice following optogenetic inhibition of LH<sup>Vglut2</sup> neurons with yellow light ( $n \geq 10$  gait cycles per mouse,  $n = 4$  mice per group). Statistics are provided in Supplementary Data 1. **e**, As in **b**, for mice following photostimulation and injections of AAVs expressing only the reporter protein GFP, with no opsin expression ( $n \geq 10$  gait cycles per mouse,  $n = 5$  mice per group). Statistics are provided in Supplementary Data 1.



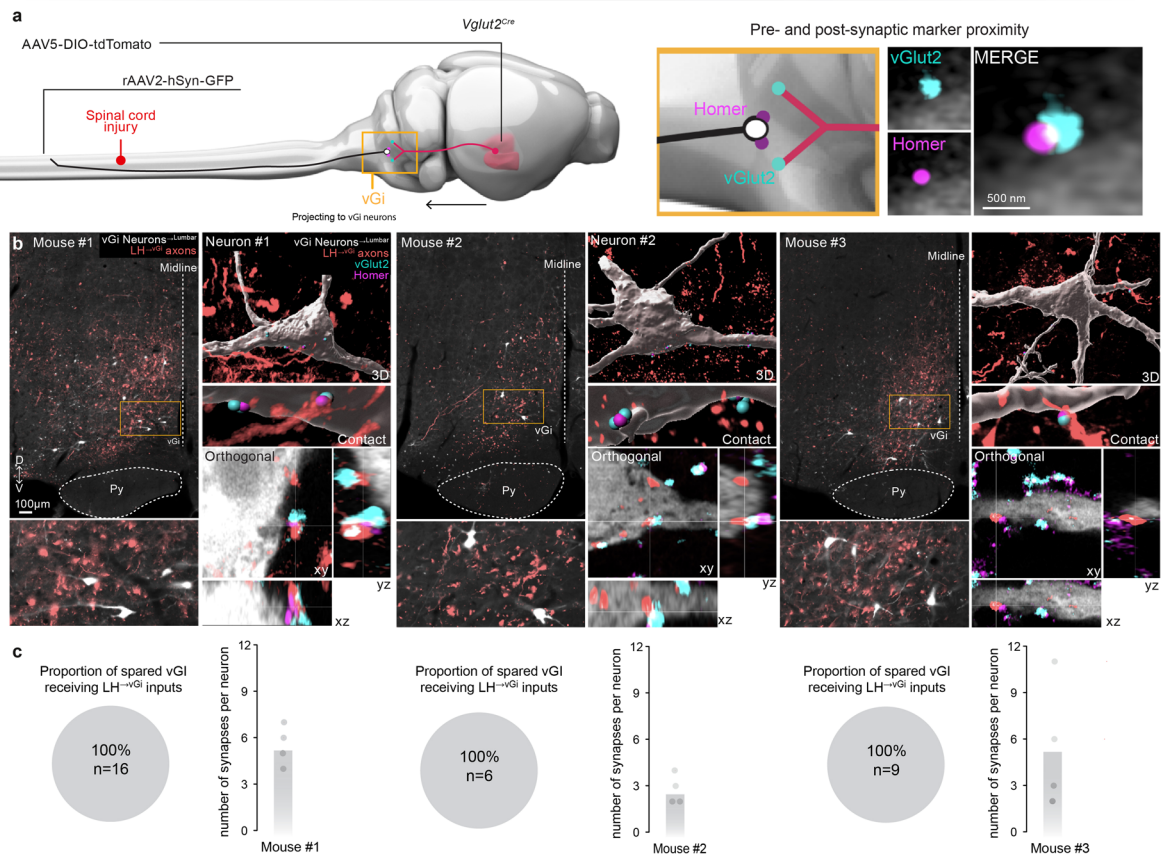
Extended Data Fig. 6 | See next page for caption.

**Extended Data Fig. 6 | Optogenetic stimulation of LH<sup>Vglut2</sup> neurons augments walking after contusion SCI via vGi neurons.** **a**, Schematic of the experimental scheme demonstrating contusion at T9 in the mouse. Cleared spinal cord demonstrating a representative lesion with cross-sectional histology of the lesion epicenter (preserved tissue stained with GFAP) and associated lesion reconstruction. **b**, Kinematic analysis of mice following contusion SCI. Walking was quantified using principal component analysis as described in Fig. 1c and Extended Data Fig. 1c ( $n \geq 10$  gait cycles per mouse,  $n = 5$  mice in the uninjured group,  $n = 8$  in the contusion SCI group). Statistics are provided in Supplementary Data 1. **c**, LH connections with the lumbar spinal cord are not reliably preserved after contusion SCI. Bilateral G-deleted rabies were injected into the lumbar spinal cord at 8 weeks post-SCI ( $n = 3$  mice). After 4 days, mice were perfused and the brains extracted, cleared, imaged, and registered to the Allen Brain Atlas. Neurons were segmented and quantified. *Left*, Representative cleared whole mouse brain and spinal cord demonstrating injection site, contusion, and labeling of brain neurons. *Middle*, 3D brain representations demonstrating labeling in the vGi but not the lateral hypothalamus with associated optical sections ( $50 \mu\text{m}$  projection). *Right*, Bar plots demonstrating the percentage of all neurons with direct connections to the lumbar spinal cord after contusion for several regions with the highest proportion of neurons. vGi neurons (gigantocellular nucleus, magnocellular nucleus) with direct

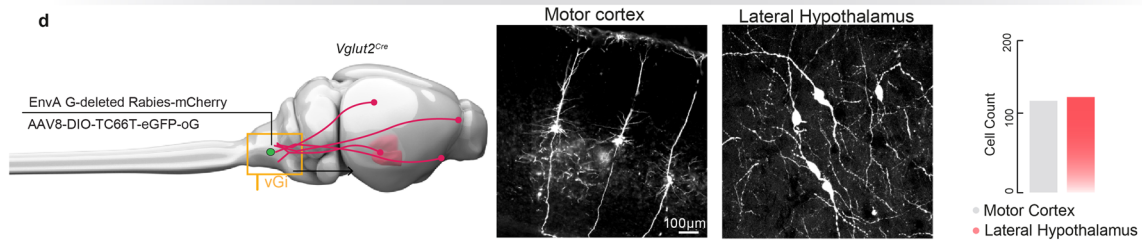
projections past the contusion SCI were prominent. We noted an absence of direct projections from the LH to the lumbar spinal cord. Lesion reconstructions and quantifications for the animals analyzed are also provided. Mean sparing = 29.0%. 3 V: third ventricle. **d**, Schematic of the experimental scheme to understand efferent projections from LH<sup>Vglut2</sup> neurons to various motor centers in the brainstem. Vglut2<sup>Cre</sup> mice underwent a left lateral thoracic hemisection and were allowed to spontaneously recover for 6 weeks ( $n = 3$  mice). To understand the efferent projections of recovered mice, AAV5-DIO-mGFP was injected into the right LH of these mice, which was allowed to express for 4 weeks. Photomicrograph demonstrating a representative injection site with labeled LH<sup>Vglut2</sup> neurons. Representative images demonstrating axon projections from LH<sup>Vglut2</sup> neurons to various brainstem motor centers. Top panel demonstrates projections to the PAG (periaqueductal gray), CnF (cuneiform nucleus), and PTG (pedunculopontine tegmental nucleus). Middle panels demonstrate projections to the PnC (pontine reticular nucleus) and RMg (raphe magnus). Bottom panels demonstrate projections to the medullary reticular formation including the Gi (gigantocellular reticular nucleus) and vGi, and LPGi (lateral paragigantocellular reticular nucleus). Insets demonstrate magnified views of the axons. Density quantification of fibers to each of the brainstem motor centers divided into ipsilateral, contralateral, and midline (for RMg) quantifications. 3 V: third ventricle.



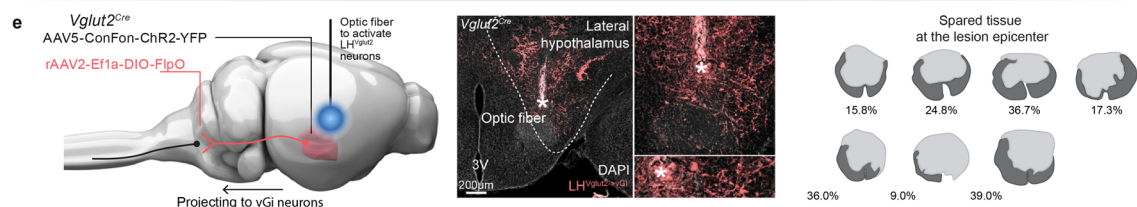
Spared vGI vGlut2 neurons receive Synaptic inputs from vGlut2 LH neurons



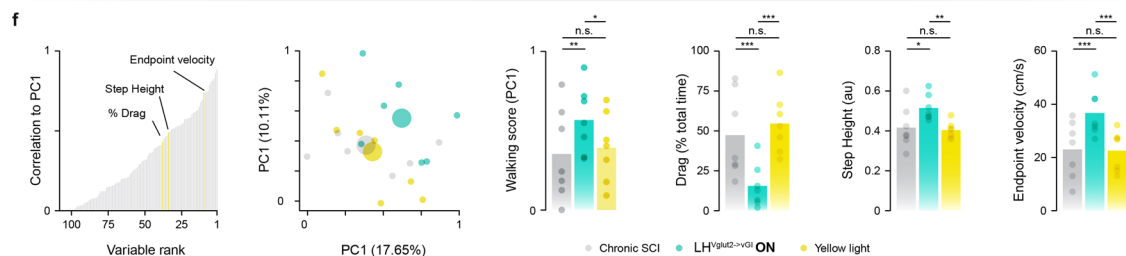
Neurons with synaptic input to vGI vGlut2 neurons



Restricted expression of ChR2 to glutamatergic neurons projecting to the vGI



Optogenetic activation of glutamatergic neurons of the lateral hypothalamus with direct projections to the vGI improves walking after contusion SCI

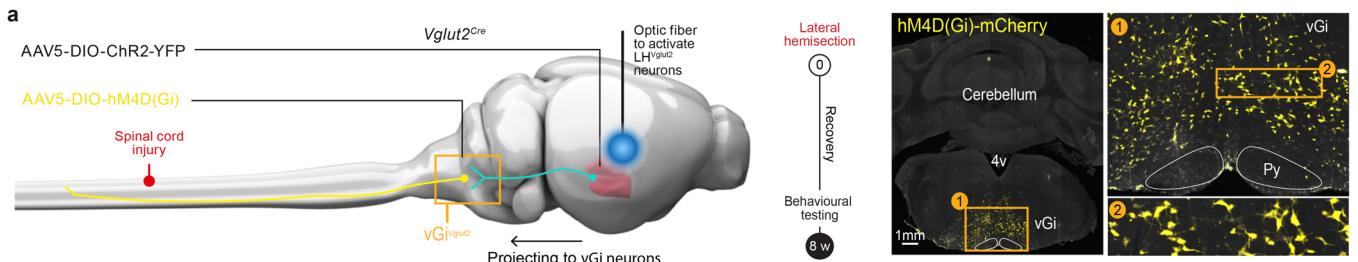


Extended Data Fig. 7 | See next page for caption.

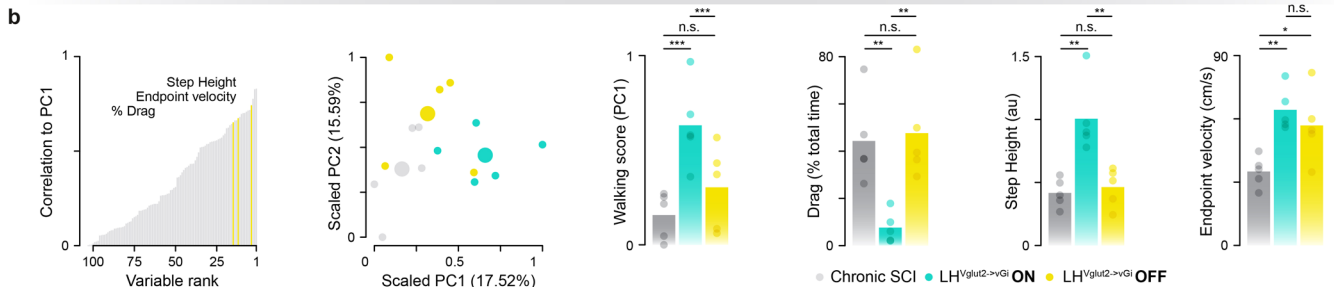
**Extended Data Fig. 7 | Characterization of neurons in the LH and motor cortex with projections to vGi<sup>Vglut2</sup> neurons.** **a**, Schematic of the experimental scheme to understand projection inputs on vGi<sup>Vglut2</sup> neurons with spared projections to the lumbar spinal cord. Vglut2<sup>Cre</sup> mice underwent a contusion SCI and were allowed to spontaneously recover for one month (n = 3 mice). To understand the inputs onto vGi<sup>Vglut2</sup> neurons with spared projections to the lumbar spinal cord, rAAV2-hSyn-GFP was injected into the lumbar spinal cord bilaterally. AAV-DIO-tdTomato was concomitantly injected into the right LH of these mice, which was allowed to express for 4 weeks. Photomicrographs were acquired with immunohistochemical staining for Homer and vGlut2, in addition to the viral labelling. **b**, Photomicrographs from each of the three tested mice, demonstrating synaptic-like appositions of LH<sup>Vglut2</sup> projections to vGi<sup>Vglut2</sup> with spared axonal projections to the lumbar spinal cord. Sections have been labelled with immunohistochemistry for the presynaptic marker vGlut2 and the postsynaptic marker Homer. **c**, Quantification of the number of vGi<sup>Vglut2</sup> neurons with at least one synaptic-like apposition from LH<sup>Vglut2</sup> neurons. **d**, Schematic

of the experimental scheme to label neurons in the motor cortex and LH with monosynaptic projections to vGi<sup>Vglut2</sup> neurons. Vglut2<sup>Cre</sup> mice were injected with AAV8-DIO-TC66T-eGFP-oG in the vGi, followed by injections of EnvA G-deleted Rabies-mCherry two weeks later. Photomicrographs demonstrate neurons in the motor cortex and LH with monosynaptic projections to vGi<sup>Vglut2</sup> neurons. **Right**, quantification of the number of labelled neurons in each region. **e**, Schematic of the experimental scheme demonstrating injection of AAV5-Con/Fon-ChR2-YFP into the right LH with insertion of an optic fiber and of retro-AAV2-DIO-FLPo into the vGi of Vglut2<sup>Cre</sup> mice. Mice underwent a contusion injury at T9, and behavioral recordings were performed at 6 weeks post-SCI. **Middle**, Representative image demonstrating AAV5-Con/Fon-ChR2-YFP expression in the right LH and position of the optic fiber. **Right**, Contusion lesion epicenter reconstructions with percent spared tissue. Mean sparing = 25.5%. 3 V: third ventricle. **f**, As in Extended Data Fig. 6b, for mice following optogenetic activation of LH<sup>Vglut2</sup> neurons with direct projects to the vGi (n ≥ 10 gait cycles per mouse, n = 7 mice per group). Statistics are provided in Supplementary Data 1.

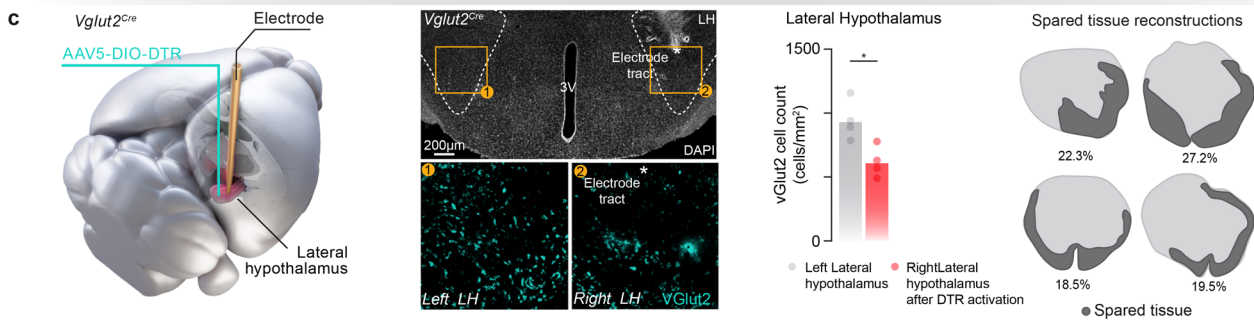
Expression of DREADDs in glutamatergic neurons located in the vGi



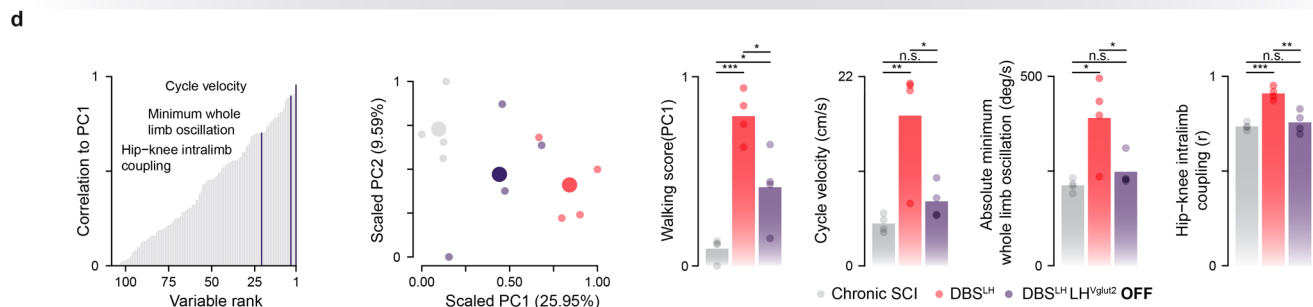
Inactivation of glutamatergic neurons in the vGi abolishes improvement of walking resulting from the activation of glutamatergic neurons in the lateral hypothalamus



Ablation of glutamatergic neurons located in the lateral hypothalamus



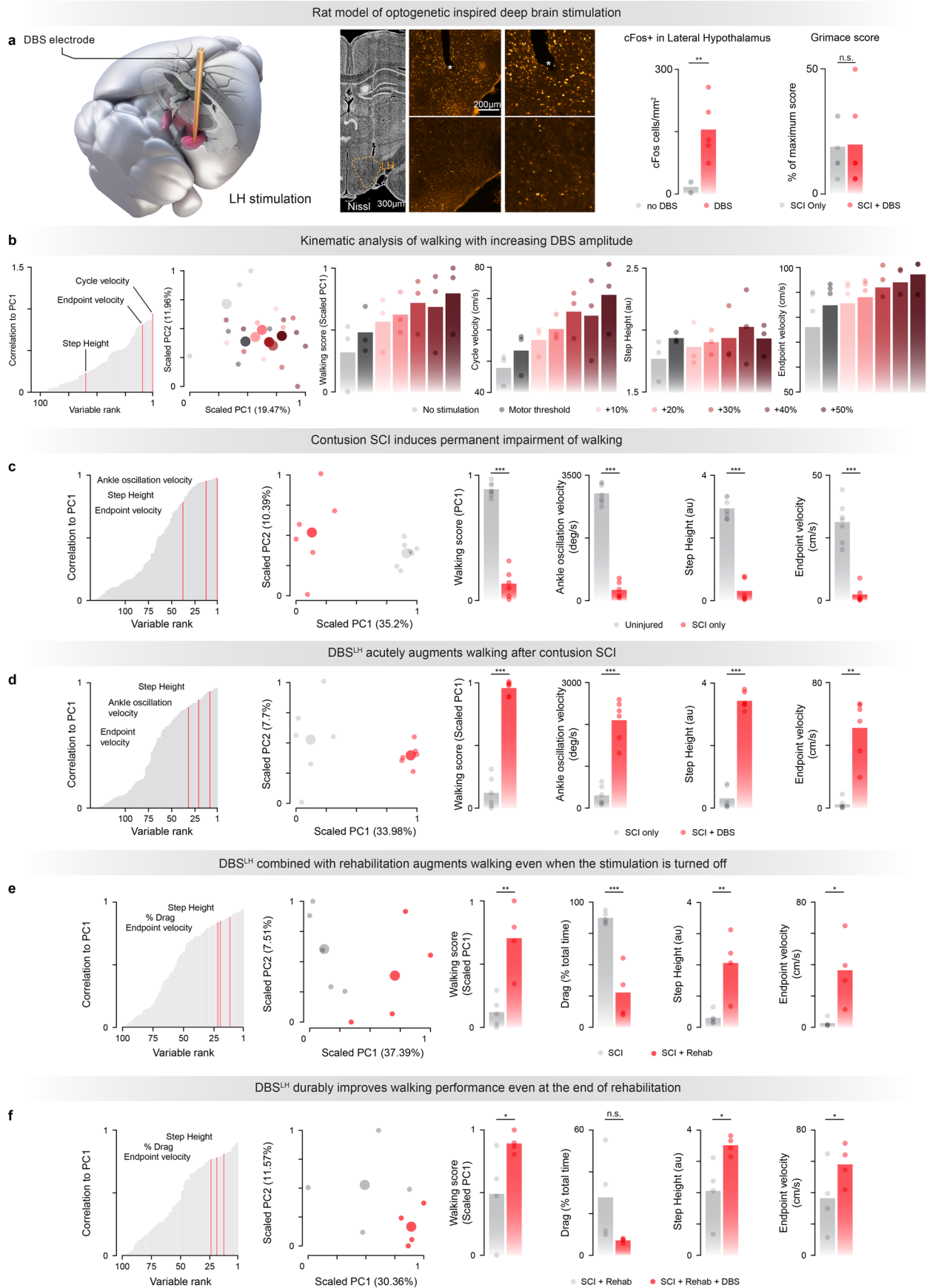
Ablation of glutamatergic neurons located in the lateral hypothalamus blunts improvement of walking resulting from DBS of the lateral hypothalamus



**Extended Data Fig. 8 | vGi<sup>vGlut2</sup> neuron activation is necessary for LH-mediated improvements in walking after SCI and these effects are phenocopied by electrical deep brain stimulation.**

**a**, Schematic of the experimental scheme demonstrating injections of AAV5-DIO-ChR2-YFP into the right LH with insertion of an optic fiber and AAV5-hSyn-DIO-hM4D(Gi)-mCherry into the vGi of Vglut2<sup>Cre</sup> mice. Mice underwent a left lateral hemisection injury at T10, and behavioral recordings were performed at 8 weeks post-SCI after spontaneous recovery. Representative images demonstrating hM4D(Gi)-mCherry expression in the vGi. py: pyramidal tract; 4v: Fourth ventricle. **b**, Kinematic analysis of mice following optogenetic activation of LH<sup>vGlut2</sup> neurons and concomitant chemogenetic inactivation of vGi<sup>vGlut2</sup> neurons after SCI. Walking was quantified using principal component analysis as described in Fig. 1c and Extended Data Fig. 1c (n ≥ 10 gait

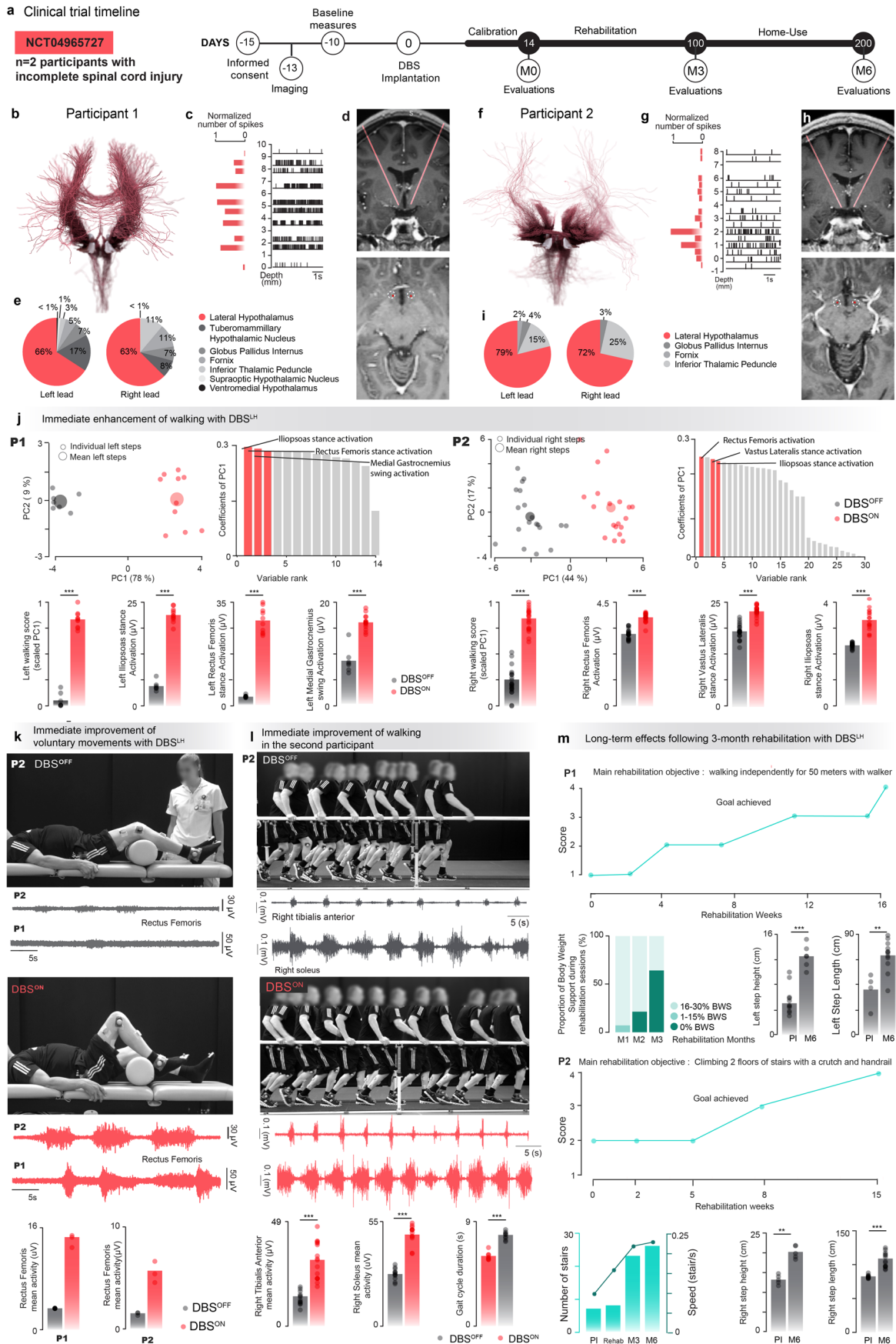
cycles per mouse, n = 5 mice per group). Statistics are provided in Supplementary Data 1. **c**, Schematic of the experimental scheme demonstrating injections of AAV5-DIO-DTR into the right LH of Vglut2<sup>Cre</sup> mice, with electrical stimulation of the LH (DBS<sup>LH</sup>). Mice underwent a contusion injury at T9, and behavioral recordings were performed at 6 weeks post-SCI. **Middle**, Representative image demonstrating ablation of LH<sup>vGlut2</sup> neurons. Bar graph demonstrates significant reduction in LH<sup>vGlut2</sup> neurons (n = 4 per group; independent samples t-test; t = 0.2548; p-value = 0.0145). **Right**, Lesion reconstructions and quantifications for the animals analyzed are also provided. Mean sparing = 21.8%. **d**, As in **b**, for mice with DBS followed by DBS and ablation of LH<sup>vGlut2</sup> neurons (n ≥ 10 gait cycles per mouse, n = 4 mice per group). Statistics are provided in Supplementary Data 1.



**Extended Data Fig. 9 | See next page for caption.**

**Extended Data Fig. 9 | DBS<sup>LH</sup> in rats with contusion SCI leads to immediate and durable improvements in walking even when DBS<sup>LH</sup> is turned off.** **a**, Schematic of the experimental scheme demonstrating electrical stimulation of the LH (DBS<sup>LH</sup>) in rats with contusion SCI at T9. *Middle*, Representative image demonstrating electrode location in the LH. Bar graph demonstrates significant increase in cFos positive cells in the LH with stimulation (n = 4 no DBS, n = 5 DBS; independent samples two-tailed t-test; t = 3.741; p-value = 0.0073). The stimulation was well-tolerated by all rats, as evidenced by no significant difference in grimace score (n = 6 per group; paired samples two-tailed t-test; t = 0.2548; p-value = 0.8090). **b**, Kinematic analysis of uninjured rats following increasing amplitudes of DBS<sup>LH</sup>. Walking was quantified using principal

component analysis as described in Fig. 1c and Extended Data Fig. 1c (n ≥ 10 gait cycles per rat, n = 3 rats). **c**, As in **b**, for rats after contusion SCI (n ≥ 10 gait cycles per rat, n = 7 rats in the uninjured group, n = 6 rats in the contusion group). Statistics are provided in Supplementary Data 1. **d**, As in **b**, for rats after contusion SCI and acute activation of DBS<sup>LH</sup> at five weeks post-SCI (n ≥ 10 gait cycles per rat, n = 6 rats per group). Statistics are provided in Supplementary Data 1. **e**, As in **b**, for rats after contusion SCI and rehabilitation enabled by DBS<sup>LH</sup> (n ≥ 10 gait cycles per rat, n = 5 rats in SCI group, n = 4 rats in SCI + Rehab group). Statistics are provided in Supplementary Data 1. **f**, As in **b**, for rats after contusion SCI with rehabilitation, and acute activation of DBS<sup>LH</sup> after rehabilitation (n ≥ 10 gait cycles per rat, n = 4 rats per group). Statistics are provided in Supplementary Data 1.



Extended Data Fig. 10 | See next page for caption.

**Extended Data Fig. 10 | DBSLH in two incomplete SCI individuals leads to immediate and durable improvements in walking.** **a**, Clinical trial timeline. **b**, Diffusion tensor imaging (DTI)-based tractography exploring LH neuronal projections in the first participant. **c**, Intra-operative spiking activity of the first participant while descending a micro-electrode within the LH exposes basal activity of neurons throughout the rostrocaudal extent of the LH. **d**, Coronal and axial sections of the preoperative MRI of the first participant showing the projection of the DBS leads. **e**, Computer simulations of volume of activated tissues of the most-used stimulation program of the first participant. The distribution of the proportion of activated regions shows the LH as the main activated region. P1 stimulation program: left & right DBS contacts 0 + 1-2 + , amplitude 7 mA. **f**, As in b, for the second participant. **g**, As in c, for the second participant. **h**, As in d, for the second participant. **i**, As in e, for the second participant. P2 stimulation program: left & right DBS contacts 1 + 2-3 + , amplitude 7 mA. Pulse width and frequency are not taken into account when calculating the activation volume. **j**, Kinematic and muscle analysis of participants P1 and P2 walking on parallel bars with and without DBSLH during the same calibration session. Walking was quantified using principal component analysis applied to gait parameters calculated from kinematic and muscle recordings. For both participants, the first principal component (PC1) distinguished steps enhanced by DBSLH from steps without DBSLH. Gait

scores were thus quantified as the scores on PC1 ( $n \geq 7$  gait cycles). Statistics are provided in Supplementary Data 3. **k**, Attempts of participants P1 and P2 to perform 3 voluntary hip flexions with and without DBSLH, during the same calibration session. Associated recording of electromyographic activity from flexor muscle and its quantification ( $n = 3$ ). **l**, Chronophotography of walking recorded in the second participant with and without DBSLH, together with the associated recording of electromyographic activity from extensor and flexor muscles and their quantification ( $n = 11$  gait cycles, dots represent individual trials). Statistics are provided in Supplementary Data 3. **m**, Quantification of the walking improvements following 3 months of rehabilitation enhanced with DBS, for P1 and P2. Goal achievement score throughout rehabilitation for P1 and P2 (scale: 1, not achieved/with significant help; 2, very partially achieved / with light to moderate help; 3, partially achieved / under supervision; 4, achieved / independent). Proportion of weight support (BWS) provided to P1 during sessions. Quantification of number of stairs climbed and related speed of P2 throughout the whole study (P1: pre-implantation; Rehab: during rehabilitation, DBSON; M3: post-rehabilitation, DBSON; M6: end of main study, DBSON). Quantification of step height and step length while standing and walking on parallel bars respectively for P1 and P2, pre-implantation (P1) and at the end of main study (M6), DBSOFF. Statistics are provided in Supplementary Data 3.

## Reporting Summary

Nature Portfolio wishes to improve the reproducibility of the work that we publish. This form provides structure for consistency and transparency in reporting. For further information on Nature Portfolio policies, see our [Editorial Policies](#) and the [Editorial Policy Checklist](#).

### Statistics

For all statistical analyses, confirm that the following items are present in the figure legend, table legend, main text, or Methods section.

n/a Confirmed

- The exact sample size ( $n$ ) for each experimental group/condition, given as a discrete number and unit of measurement
- A statement on whether measurements were taken from distinct samples or whether the same sample was measured repeatedly
- The statistical test(s) used AND whether they are one- or two-sided  
*Only common tests should be described solely by name; describe more complex techniques in the Methods section.*
- A description of all covariates tested
- A description of any assumptions or corrections, such as tests of normality and adjustment for multiple comparisons
- A full description of the statistical parameters including central tendency (e.g. means) or other basic estimates (e.g. regression coefficient) AND variation (e.g. standard deviation) or associated estimates of uncertainty (e.g. confidence intervals)
- For null hypothesis testing, the test statistic (e.g.  $F$ ,  $t$ ,  $r$ ) with confidence intervals, effect sizes, degrees of freedom and  $P$  value noted  
*Give  $P$  values as exact values whenever suitable.*
- For Bayesian analysis, information on the choice of priors and Markov chain Monte Carlo settings
- For hierarchical and complex designs, identification of the appropriate level for tests and full reporting of outcomes
- Estimates of effect sizes (e.g. Cohen's  $d$ , Pearson's  $r$ ), indicating how they were calculated

*Our web collection on [statistics for biologists](#) contains articles on many of the points above.*

### Software and code

Policy information about [availability of computer code](#)

Data collection

Human Data: Surgery with the StealthStation Surgical Navigation software (Medtronic), Intra-operative electrophysiological recordings with Neuro Omega (AlphaOmega Engineering) Dantec KeyPoint Focus (Natus Medical), Kinematics with Vicon (Motion Systems), Brain recordings with the Percept PC neurostimulator (Medtronic), EMG with Delsys Trigno (Delsys), fMRI with a Siemens Prisma 3T (Siemens).  
Mouse and Rat Data were collected using Vicon 5, Zen Black (Zeiss), ImageJ (FIJI), Olympus VS-Desktop, QuPath(v0.4.3), Arivis Vision4D (Arivis AG, Germany), Imaris (9.1.2, 64Bit, Bitplane), Matlab.

Data analysis

All softwares and software versions used to analyze data are described in the Method section at the relevant paragraph: Imaris, Arivis, QuPath, Olympus Vs-Desktop, ImageJ, Labchart, MATLAB and R. Illustrations were generated using Autodesk 2020.2, Maya 2020.2, Adobe Illustrator 2023. R (version 3.6.0) and GraphPrism (version 10.0.3) were used for statistical evaluation.

For manuscripts utilizing custom algorithms or software that are central to the research but not yet described in published literature, software must be made available to editors and reviewers. We strongly encourage code deposition in a community repository (e.g. GitHub). See the Nature Portfolio [guidelines for submitting code & software](#) for further information.



## Data

Policy information about [availability of data](#)

All manuscripts must include a [data availability statement](#). This statement should provide the following information, where applicable:

- Accession codes, unique identifiers, or web links for publicly available datasets
- A description of any restrictions on data availability
- For clinical datasets or third party data, please ensure that the statement adheres to our [policy](#)

Data that supports the findings and software routines developed for the data analysis will be made available upon reasonable request to the corresponding authors at [jocelyne.bloch@chuv.ch](mailto:jocelyne.bloch@chuv.ch) or [gregoire.courtine@epfl.ch](mailto:gregoire.courtine@epfl.ch). Datasets underpinning this manuscript are available on Zenodo (<https://zenodo.org/records/10628681>)

## Research involving human participants, their data, or biological material

Policy information about studies with [human participants or human data](#). See also policy information about [sex, gender \(identity/presentation\), and sexual orientation](#) and [race, ethnicity and racism](#).

### Reporting on sex and gender

Information on sex (Female/Male) and ethnicity (Caucasian/Black/Asian/Other) was determined based on self reporting and is provided in Supplementary data 4 (study participants). 2 participants were included in the study (1 Male, 1 Female), thereby including equal distribution of male and female participants. The sex of the participants was taken into consideration when measuring testosterone levels as part of the blood sampling measurements. Gender information was not explicitly collected during the study.

### Reporting on race, ethnicity, or other socially relevant groupings

The categorization of individuals into different ethnic groups is based on the concept of ethnicity that pertains to an individual's cultural and social identity, encompassing shared traditions, language, heritage, and historical connections to particular social or cultural groups. The collected data regarding the participants ethnicity is provided directly by the participants themselves. This method of classification relies on self-report, meaning that individuals are asked to choose or self-identify with the ethnic category that best represents their own background. Considering the very few number of participants in this trial, no ethnicity-based analysis was performed in this trial.

### Population characteristics

Two participants that have suffered traumatic spinal cord injury were included in the study. Demographic data (Age, Sex, Height, Weight, Ethnicity) was collected in the study. Moreover, their neurological status was evaluated according to the International Standards for Neurological Classification of Spinal Cord Injury and is fully reported in Supplementary Data 4.

### Recruitment

Participants could only be recruited after obtaining approval from the competent authorities in Switzerland (Swissmedic) and the ethical committee (CER-VD). Investigators were responsible for screening patients for enrollment in the study. Participants may be recruited within the list of patients commonly followed by the research and clinical department at the hospital or may be referred to the principal investigator via their networks from other primary care facilities and/or rehabilitation institutions. A first contact is then established between the principal investigator and eligible patients. During this first visit, the study will be presented to the eligible patients via a printed information sheet. The participants receive full oral and written information about the investigation using non-technical language and was given time to decide whether to participate. No direct financial incentive was offered to the participants although fees related to travel expenses and lodging are covered/reimbursed by the study.

### Ethics oversight

Competent Ethic Committee (CEC) : The Sponsor submitted the investigation to the "Commission Cantonale d'Éthique de la Recherche sur l'Être Humain – CER-VD (Swissethics)" and obtain ethical committee approval before the start of the investigation.

Competent Authorities (CA) : The Sponsor submitted an investigation to Swissmedic and obtain regulatory approval before the start of this study.

Note that full information on the approval of the study protocol must also be provided in the manuscript.

## Field-specific reporting

Please select the one below that is the best fit for your research. If you are not sure, read the appropriate sections before making your selection.

- Life sciences       Behavioural & social sciences       Ecological, evolutionary & environmental sciences

For a reference copy of the document with all sections, see [nature.com/documents/nr-reporting-summary-flat.pdf](https://nature.com/documents/nr-reporting-summary-flat.pdf)

## Life sciences study design

All studies must disclose on these points even when the disclosure is negative.

### Sample size

Rodent: Sample sizes were chosen based on previous physiological studies and similar animal models (Kathe et al., Nature 2022; Squair et al., Science 2023; Squair et al., Nature 2021).

Human: Pilot studies to examine feasibility of novel therapies have previously been published using 1 to 4 participants. We employed a similar strategy for this study (Lorach et al., Nature 2023; Squair et al., Nature 2021; Milekovic et al., Nature Medicine 2023). Here, we report

the first proof-of-concept results in two patients who contributed to a First-in-Man study. No previous data existed to predetermine sample size.

Data exclusions	The exclusion criteria for data was established prior to the experiments: In rodents, expression of viral vectors were confirmed post-mortem. If here was a lack of expression, the animal was excluded from behavioural analysis. No data were excluded in human clinical data sets.
Replication	All tested conditions were repeated across multiple trials (see gait cycles in the manuscript for number of repeated trials to ensure consistency). The trials were averaged to obtain single-subject mean performance. Histological assessments were repeated in at least 3 animals showing consistent outcomes.
Randomization	Animals were randomly assigned to groups. Randomization for human participants was not sought in the present study. Each participant served as their own control (stimulation off vs. on conditions; evaluations at different points over time throughout the rehabilitation training period).
Blinding	For kinematic analysis blinding was not possible (and irrelevant, due to behavioral changes across conditions), however the investigator was blinded to group allocation during data collection (i.e. recordings) and video tracking is a highly automatized task. All histological analysis were blinded. For clinical studies, investigators were not blinded. Their expertise was required to optimize the intervention and to apply the intervention during evaluations. Furthermore, the effects of the intervention were obvious, acutely producing changes in the kinematics and muscle activities of the participants during walking.

## Reporting for specific materials, systems and methods

We require information from authors about some types of materials, experimental systems and methods used in many studies. Here, indicate whether each material, system or method listed is relevant to your study. If you are not sure if a list item applies to your research, read the appropriate section before selecting a response.

### Materials & experimental systems

### Methods

n/a	Included in the study
<input type="checkbox"/>	<input checked="" type="checkbox"/> Antibodies
<input checked="" type="checkbox"/>	<input type="checkbox"/> Eukaryotic cell lines
<input checked="" type="checkbox"/>	<input type="checkbox"/> Palaeontology and archaeology
<input type="checkbox"/>	<input checked="" type="checkbox"/> Animals and other organisms
<input type="checkbox"/>	<input checked="" type="checkbox"/> Clinical data
<input checked="" type="checkbox"/>	<input type="checkbox"/> Dual use research of concern
<input checked="" type="checkbox"/>	<input type="checkbox"/> Plants

n/a	Included in the study
<input checked="" type="checkbox"/>	<input type="checkbox"/> ChIP-seq
<input checked="" type="checkbox"/>	<input type="checkbox"/> Flow cytometry
<input type="checkbox"/>	<input checked="" type="checkbox"/> MRI-based neuroimaging

## Antibodies

Antibodies used	Primary antibodies were rabbit anti-GFAP (1:1000, Dako Z0334, USA); rabbit anti-cFos, 1:500 and 1:2000, Synaptic Systems, #226 003; a mouse anti-vGlut2 antibody (1:1000, Millipore MAB5504); guinea pig anti homer1 (synaptic systems #160004). Appropriate secondary antibodies were used at a dilution of 1:300, as follow: Goat anti Rabbit 488 (Invitrogen A11008/lot 2420730); Goat anti Rabbit 555 (Invitrogen A21428/lot 1726587); Goat anti Mouse 647 (Invitrogen A21235 /2284596); Goat anti Guinea pig (Invitrogen A214435 /1842614)
Validation	We only used commercial antibodies. All of them were quality controlled and validated by the manufacturer. Validation statements can be found on the manufacturer's website.

## Animals and other research organisms

Policy information about [studies involving animals](#); [ARRIVE guidelines](#) recommended for reporting animal research, and [Sex and Gender in Research](#)

Laboratory animals	Adult female C57BL/6 mice ( $\geq 8$ weeks at the start of the experiment, 15-30 g body weight) or transgenic male or female mice were used for all experiments. Vglut2Cre (Jackson Laboratory 016963) and VgatCre (Jackson Laboratory 28862) transgenic mouse strains were bred and maintained on a mixed genetic background (129/C57BL/6J). Adult female Lewis rats (12 weeks old, 200-250 g body weight) were used for the rehabilitation study. Rodents were maintained on a 12-hour light/dark cycle with food and water provided ad libitum at a temperature of 22 $\pm$ 1 C and relative humidity of 55 $\pm$ 5 %.
Wild animals	No wild animals were used in the study
Reporting on sex	Females
Field-collected samples	No field collected samples were used in the study.
Ethics oversight	All procedures and surgeries were approved by the Veterinary Office of the Canton of Geneva (Switzerland; license GE/112/20).

Note that full information on the approval of the study protocol must also be provided in the manuscript.

## Clinical data

Policy information about [clinical studies](#)

All manuscripts should comply with the ICMJE [guidelines for publication of clinical research](#) and a completed [CONSORT checklist](#) must be included with all submissions.

Clinical trial registration	NCT04965727 SNCTP 000004348
Study protocol	<a href="https://clinicaltrials.gov/study/NCT04965727">https://clinicaltrials.gov/study/NCT04965727</a>
Data collection	Investigational site is at CHUV; data was collected between September 2021 and January 2023 in two participants.
Outcomes	<p>Primary Endpoints: The primary endpoint is the occurrence of all Serious Adverse Events (SAE) and Adverse Events (AE) that are deemed related or possibly related to study procedure or to the study investigational device: nature and description of SAE and AE. This includes the time period from implantation up to the end of the study. We followed up on changes in vital signs and bloodwork throughout the study to document adverse events related to the therapy.</p> <p>Secondary Endpoints: Lower extremity motor scores; Walking performance; Neurobiomechanical recordings.</p>

## Plants

Seed stocks	<i>Report on the source of all seed stocks or other plant material used. If applicable, state the seed stock centre and catalogue number. If plant specimens were collected from the field, describe the collection location, date and sampling procedures.</i>
Novel plant genotypes	<i>Describe the methods by which all novel plant genotypes were produced. This includes those generated by transgenic approaches, gene editing, chemical/radiation-based mutagenesis and hybridization. For transgenic lines, describe the transformation method, the number of independent lines analyzed and the generation upon which experiments were performed. For gene-edited lines, describe the editor used, the endogenous sequence targeted for editing, the targeting guide RNA sequence (if applicable) and how the editor was applied.</i>
Authentication	<i>Describe any authentication procedures for each seed stock used or novel genotype generated. Describe any experiments used to assess the effect of a mutation and, where applicable, how potential secondary effects (e.g. second site T-DNA insertions, mosaicism, off-target gene editing) were examined.</i>

## Magnetic resonance imaging

### Experimental design

Design type	Participants were lying in the MRI scanner and asked to perform monopedal and bipedal foot flexion/extension movements in a visually cued block-design paradigm.
Design specifications	Each block consisted of 8 either monopedal or bipedal movements cued externally every 2 seconds by a visual symbol depicting the corresponding body part. The 21 blocks (7 monopedal, 14 bipedal, i.e., 168 movements in total) were interspersed with an equal number of rest periods (fixation cross for 16 seconds). Before each block, participants saw a brief instruction about the upcoming task to perform, followed by a countdown of 3 seconds. The order of movements was balanced and pseudo-randomised.
Behavioral performance measures	Participants' real-time behavioral performance during the fMRI data acquisition was collected using a MR-compatible pneumatic device.

### Acquisition

Imaging type(s)	diffusion, structural and functional
Field strength	3T
Sequence & imaging parameters	MRI data were acquired on a Siemens Prisma 3T scanner using a 64-channel head coil. Functional images were acquired using a 3D multi-shot EPI sequence 70 at 2 mm isotropic voxel size (number of volumes: 239; 60 axial slices parallel to AC/PC line; matrix size: 92 x 92; slice TR = 52 ms; volume TR = 3.328 s; TE = 30 ms; flip angle $\alpha=15^\circ$ ; slice oversampling: 6.7%). Anatomical data were acquired at 1.5 mm voxel size (matrix size: 160 x 150 x 120; FoV 256 x 240 x 176 mm) using a 3D FLASH sequence, providing estimates of the longitudinal relaxation rate, the effective proton density, magnetisation transfer and transverse relaxation rate.
Area of acquisition	Whole brain
Diffusion MRI	<input checked="" type="checkbox"/> Used <input type="checkbox"/> Not used
Parameters	the qMRI protocol included three multi-echo 3D fast low angle shot (FLASH) acquisitions with magnetization transfer-weighted (MTw:

Parameters TR = 24.5 ms,  $\alpha = 6^\circ$ ), proton density-weighted (PDw: TR = 24.5 ms,  $\alpha = 6^\circ$ ), and T1-weighted (TR = 24.5 ms,  $\alpha = 21^\circ$ ) contrasts at 1 mm isotropic resolution<sup>71,73</sup>. To correct for the effects of RF transmit field inhomogeneities<sup>74</sup> B1 mapping data was acquired using the 3D EPI spin-echo and stimulated echo method as previously described (4 mm<sup>3</sup> resolution, TE = 39.06 ms, TR = 500 ms)<sup>74,75</sup>. B0-field mapping data was acquired to correct image distortions in the EPI data (2D double-echo FLASH sequence with slice thickness = 2 mm, TR = 1020 ms, TE1/TE2 = 10/12.46 ms,  $\alpha = 90^\circ$ , BW = 260 Hz/pixel). The total acquisition time was 27 min.

## Preprocessing

Preprocessing software	All steps of data processing and analysis were performed in the framework of SPM12 (Wellcome Trust Centre for Neuroimaging, <a href="http://www.fil.ion.ucl.ac.uk/spm">www.fil.ion.ucl.ac.uk/spm</a> ) running under MATLAB 7.13 (The MathWorks, Inc., Natick, Massachusetts, United States).
Normalization	Functional data was realigned to the session mean, corrected for receive coil inhomogeneities and EPI distortion <sup>72</sup> , and co-registered to the high-resolution structural data.
Normalization template	na
Noise and artifact removal	This was followed by spatial smoothing using a 3D Gaussian kernel of 3 mm full-width-at-half-maximum.
Volume censoring	na

## Statistical modeling & inference

Model type and settings	These models were then used as the outcome measure in a mixed effect linear model wherein a random effect was included for participants and fixed effects for sex and age.
Effect(s) tested	The adjusted estimate and p-value for this final second-level model is reported.
Specify type of analysis:	<input checked="" type="checkbox"/> Whole brain <input type="checkbox"/> ROI-based <input type="checkbox"/> Both
Statistic type for inference	na
(See <a href="#">Eklund et al. 2016</a> )	
Correction	Corrected for receive coil inhomogeneities and EPI distortion

## Models & analysis

n/a	Involvement in the study
<input checked="" type="checkbox"/>	<input type="checkbox"/> Functional and/or effective connectivity
<input checked="" type="checkbox"/>	<input type="checkbox"/> Graph analysis
<input checked="" type="checkbox"/>	<input type="checkbox"/> Multivariate modeling or predictive analysis